Photonic Crystals for High Temperature Applications

by

Yi Xiang Yeng

M. Eng. / B. A. (Hons), University of Cambridge, United Kingdom (2008)

Submitted to the Department of Electrical Engineering and Computer Science
in partial fulfillment of the requirements for the degree of

Doctor of Philosophy in Electrical Engineering and Computer Science

at the

MASSACHUSETTS INSTITUTE OF TECHNOLOGY

Sept 2014

Author .....
Department of Electrical Engineering and Computer Science
Aug 29, 2014

Certified by .....
Marin Soljačić
Professor of Physics and MacArthur Fellow
Thesis Supervisor

Accepted by .....
Leslie A. Kolodziejski
Chairman, Department Committee on Graduate Students

Photonic Crystals for High Temperature Applications

by

Yi Xiang Yeng

Submitted to the Department of Electrical Engineering and Computer Science
on Aug 29, 2014, in partial fulfillment of the
requirements for the degree of
Doctor of Philosophy in Electrical Engineering and Computer Science

Abstract

This thesis focuses on the design, optimization, fabrication, and experimental realization of metallic photonic crystals (MPhCs) for high temperature applications, for instance thermophotovoltaic (TPV) energy conversion and selective solar absorption. We begin with the exploration of refractory two-dimensional (2D) MPhC slabs as selective thermal emitters that approach the emittance of a blackbody below a cutoff wavelength, and zero emittance above the cutoff. The theory behind the enhancement of thermal emission is explored, leading to design handles that enable optimization for different applications. The fabrication process and extensive characterization of optimized 2D MPhCs are also presented. Next, we utilize non-linear global optimization tools to further optimize the 2D MPhCs for various TPV energy conversion systems. Performance estimates of realistic TPV systems incorporating experimentally demonstrated spectral control components are also presented. The numerical model is also used to pinpoint deficiencies in current TPV systems to uncover areas of future research to further improve system efficiencies. In particular, we show that air-filled 2D MPhCs suffer from decreased selective emission at larger polar angles, which can be circumvented by filling and coating the 2D MPhCs with a suitable refractory dielectric material. Finally, we explore PhC enhanced silicon (Si) photovoltaic cell based TPV systems numerically. Experiments towards record breaking efficiencies for Si cell based TPV systems are also presented and shown to agree well with numerical estimates, thus paving the way towards widespread adoption of what may be a promising highly efficient, portable, and reliable energy conversion system.

Thesis Advisor	Marin Soljačić Professor of Physics
Thesis Committee	Ivan Čelanović Principal Research Scientist
	Erich P. Ippen Professor of Electrical Engineering
	Leslie A. Kolodziejski Professor of Electrical Engineering

Acknowledgements

The journey towards a Ph.D. at MIT has been wonderful and often overwhelming. I am deeply indebted to many people I met at MIT for making the time working on my doctoral studies an unforgettable experience. First and foremost, I would like to express my most sincere gratitude to my thesis advisor, Prof. Marin Soljačić for his tutelage, support, and being an inspiration throughout the course of my Ph.D. with his awe-inspiring ideas. I am also thankful to Marin for his invaluable advice and guidance on the personal and career level. I thoroughly enjoyed the numerous discussions we shared, as well as the regular group outings that Marin organises.

In addition, I am deeply grateful to Dr. Ivan Čelanović, who has been a close research advisor throughout my doctoral studies. In fact, the Ph.D. wouldn't be possible without my earlier undergraduate research experience with Ivan alongside Dr. Natalija Jovanović while as an exchange undergraduate at MIT. They were both inspirational in my decision to further my studies at MIT. Ivan's constant guidance, encouragement, and contagious enthusiasm made it possible for me to persevere through challenging times. I am also indebted to his support in providing career opportunities and advice.

I am grateful to Prof. John Joannopoulos for his precious advice and insightful discussions, and Prof. Steven Johnson for his assistance in numerical simulations and brilliant lectures on photonic crystals, which proved to be the most useful course in my research. In addition, I would like to thank Prof. Erich Ippen and Prof. Leslie Kolodziejski for serving on my thesis committee, and providing me with valuable guidance and helpful suggestions. I would also like to thank Prof. Terry Orlando for serving on my RQE committee, and Prof. James Fujimoto for advising my academic progress.

I wish to express my warmest thanks to members in Marin's and Ivan's group for all the exciting conversations we had. I am especially grateful to Dr. Jay Senkevich and Walker Chan for all their indispensable advice on making the seemingly insurmountable TPV energy conversion experiments possible, and Dr. Peter Bermel and Dr. Michael Ghebrebrhan for guidance on numerical

simulations. Special thanks to Dr. Veronika Rinnerbauer and Veronika Stelmakh for their hard work in providing me with nanofabricated samples for my TPV experiments. I am also fortunate to have worked with several bright undergraduates that assisted me tremendously in my experimental endeavours: Elaina Chai, Imbert Wang, and Lauren Kuntz.

My early years at MIT was spent at the Nanostructures Lab (NSL), and I would like to thank everyone at NSL for making it a wonderful experience. Special thanks to Prof. Karl Berggren for accepting me into the lab, Mohammad Araghchini for his mentorship, and James Daley for his assistance with technical issues. I would also like to thank Dr. Tim Savas, Lin Lee Cheong, and Corey Fucetola for sharing their experience in nanofabrication. Some of the characterisation work was done at Centre of Material Science and Engineering, and I would like to acknowledge Tim McClure and Elisabeth Shaw for assisting me.

I would also like to acknowledge friends in Cambridge who have generously shared their experiences and advices to make a pleasant difference in my MIT experience: Song Liang Chua, Ta-Ming Shih, Wu-Hsi Li, Tsung-Han Tsai, Joann Wu, Shyue Ping Ong, Wui Siew Tan, Henry Koh, Shireen Goh, Weijian Chua, Nan Wang, and Xiangling Yap. I am also grateful to have met many sports enthusiast at MIT and Boston Metro Badminton Club, and MIT Golf Club, which provided me with opportunities to recharge and stay fit throughout the course of my studies.

Finally, I dedicate this thesis to my family, Fook Joon Yeng, Lee Pen Oh, Yi Ning Yeng, Yi Tang Yeng and Yi-Hsien Lin. This thesis would not have been possible without their understanding and support.

Contents

List of Figures

List of Tables

Nomenclature

Acronyms

1D	One-dimensional
2D	Two-dimensional
3D	Three-dimensional
AFM	Atomic force microscopy
ALD	Atomic layer deposition
ARC	Anti-reflection coating or anti-reflection coated
CSP	Concentrated solar power
DBR	Distributed Bragg reflector
DRIE	Deep reactive ion etching
EQE	External quantum efficiency
FDTD	Finite-difference time-domain
FOM	Figure of merit
FTIR	Fourier transform infrared spectroscopy

IQE	Internal quantum efficiency
IR	Infrared
MPhC	Metallic photonic crystal
PhC	Photonic crystal
PV	Photovoltaic
Q-factor	Quality factor
RCWA	Rigorous coupled wave analysis
RIE	Reactive ion etching
RTD	Resistance temperature detectors
SPP	Surface plasmon-polariton
SS	Stainless steel
TE	Transverse electric
TM	Transverse magnetic
TPV	Thermophotovoltaic
UHV	Ultra high vacuum
UNSW	University of New South Wales
ZT	Thermoelectric figure of merit

Greek Symbols

α	Absorptance or absorptivity
α_{F}	Absorptance or absorptivity of bandpass filter over all wavelengths

α_{s}	Solar absorptance
δ	Maximum size of photonic crystal sidewall deviation
$\Delta\varepsilon$	Uncertainty or change in emissivity or emittance
ΔT	Uncertainty or change in temperature
ϵ_{m}	Dielectric function of metal
ε	Emissivity or emittance
$\varepsilon(\lambda, T)$	Emissivity or emittance as a function of wavelength and temperature
$\varepsilon(\lambda, \theta)$	Emissivity or emittance as a function of wavelength and polar angle
$\varepsilon(\lambda, \theta, \phi)$	Emissivity or emittance as a function of wavelength, polar angle, and azimuthal angle
$\varepsilon(\lambda, \theta, \phi, T)$	Emissivity or emittance as a function of wavelength, polar angle, azimuthal angle, and temperature
ε_{H}	Hemispherical emittance
$\varepsilon_{\mathrm{HT}}$	Emissivity or emittance at high temperatures
$\varepsilon_{\mathrm{lw}}$	Emissivity or emittance for wavelengths larger than the cutoff wavelength
$\varepsilon_{\perp}$	Emissivity or emittance at normal incidence angle
$\varepsilon_{\mathrm{room}}$	Emissivity or emittance at room temperature
$\varepsilon_{\mathrm{sw}}$	Emissivity or emittance for wavelengths smaller than the cutoff wavelength
ε_{t}	Thermal emittance
$\eta_{\mathrm{cav\text{-}spec}}$	TPV cavity-spectral efficiency
η_{cell}	TPV cell efficiency

η_{emit}	Emission efficiency
η_{spec}	Spectral efficiency
η_{TPV}	TPV radiant heat-to-electricity efficiency
$\eta_{\text{TPV, max}}$	Maximum TPV radiant heat-to-electricity efficiency when operating at optimum emitter temperature
κ	Thermal conductivity
λ	Wavelength
λ_{c}	Cutoff wavelength
λ_{F}	Bandwidth of high reflectivity or reflectance
λ_{g}	Bandgap
ϕ	Azimuthal angle
θ	Polar angle
θ_{c}	Cutoff angle
θ_{d}	Angle at the onset of diffraction
θ_{i}	Angle of incidence
θ_p	Angle of p-th order diffraction
ω	Angular frequency
Ω_{s}	Solid angle subtended by the sun

Roman Symbols

A	Area

a	Period
a_0	Period of the first stack of DBR filter
a_l	Period of the l-th stack of DBR filter
B	Exponential chirp factor of DBR filter
b	Relative range of exponentially chirped DBR filter
C	Solar concentration factor (number of suns)
c	Speed of light
d	Depth
$\mathrm{d}A$	Infinitesimal differential area
$\mathrm{d}F$	Differential view factor
$\mathrm{d}Q_{\mathrm{dA_1}\to\mathrm{dA_2}}$	Differential radiant power incident on infinitesimal area $\mathrm{d}A_2$ from an emitter of infinitesimal area $\mathrm{d}A_1$
E_g	Energy gap or bandgap
F	View factor
$\boldsymbol{G}$	Reciprocal lattice vector
h	Planck's constant
$\hbar$	Reduced Planck's constant
I	Current
$i_\mathrm{BB}(\lambda, T)$	Spectral radiance of a blackbody as a function of temperature
I_o	Dark current

I_{sc}	Short circuit current
J_{elec}	Output electrical power density
$J_{\mathrm{elec,\ max}}$	Output electrical power density at maximum power point
$J_{\mathrm{elec,\ max}}^{\mathrm{BB}}$	Output electrical power density at maximum power point when using blackbody emitter
$J_{\mathrm{elec,\ max}}^{\mathrm{PhC}}$	Output electrical power density at maximum power point when using PhC emitter
k	Boltzmann's constant
$\boldsymbol{k}_{\parallel}$	Component of wavevector in the xy-plane
$\boldsymbol{k}_{\mathrm{SPP}}$	Wavevector of surface plasmon-polaritons
$L_{\mathrm{BB}}(\lambda, T)$	Spectral radiance of blackbody as a function of temperature
$L_{\mathrm{s}}(\lambda, T)$	Spectral radiance of sample as a function of temperature
m	Ideality factor
n	Index of refraction
n_1	Refractive index of first material of DBR filter
n_2	Refractive index of second material of DBR filter
P_{cell}	Convertible radiant power incident on photovoltaic cell
P_{cond}	Parasitic conductive heat loss
P_{elec}	Output electrical power
$P_{\mathrm{elec,\ max}}$	Output electrical power at maximum power point
P_{em}	Emitted radiant power

P_{in}	Input power
P_{re}	Reabsorbed radiant power
q	Elementary electronic charge
Q_{abs}	Absorptive quality factor
Q_{rad}	Radiative quality factor
R	Reflectance or reflectivity
r	Radius
$R_{\text{H}}(\lambda)$	Spectral hemispherical reflectance
R_{s}	Series resistance
R_{sh}	Shunt resistance
$R_{\theta=45^\circ}$	Reflectance or reflectivity at incidence angle of 45 degrees
s	Distance between two infinitesimal areas or two parallel plates
$S_{\text{s}}(\lambda)$	Terrestrial solar spectral radiance (AM1.5D)
T	Temperature
t	Thickness
T_{c}	Temperature of photovoltaic cell
Tr	Transmittance
V	Voltage
x	Figure of merit weighting factor

Chapter 1

Introduction

Since time immemorial, humankind has been persistently exploring usage of raw materials freely available on Earth to assist them in a multitude of tasks. Progressive understanding of their properties has often led to major technology breakthroughs, which enabled civilization to progress, for instance from the Stone Age to the Iron Age. However, a limit was soon reached as to what can be done with materials in their raw form, thus spurring development into processing existing materials. Eventually, humankind was able to purify raw materials, as well as engineer composites and alloys that possess properties that are more desirable compared to their raw forms.

At the turn of the 20th century, materials development has been dominated by the mystery of newly discovered electrical properties driven by the development of quantum mechanics, and particularly semiconductor physics. Scientists soon realized how to effortlessly control the flow of electrons in semiconductors, leading to the transistor revolution, without which the world today would be unimaginable. A similar path is seen in the understanding and exploitation of optical properties of materials in the past few decades, leading to the invention of the laser and a world connected by an intricate network of optical fibres. At this point, it would seem that humankind has exhausted everything that could be exploited with the well understood optical properties of raw and composite materials. To overcome this limit, a new class of materials would have to be engineered. Indeed, two seminal publications in 1987 by Eli Yablonovitch [1] and Sajeev John [2]

led to the explosion of research and development in a new class of engineered materials known as photonic crystals (PhCs).

PhCs are artificially engineered materials whereby a periodicity in the refractive index exists. In appropriately designed PhCs, bandgaps for photons (i.e. photonic bandgaps) exists [1–4]. This is analogous to the existence of bandgaps for electrons in semiconductors due to the periodic potentials in a crystal lattice. Thus, the concept of PhCs offer tantalizing prospects of manipulating the generation and propagation of photons at will. Coupled with the recent advancements in nanofabrication techniques, many applications have been made possible, ranging from room and cryogenic temperature optoelectronic devices for development of all-optical integrated circuits [5], to highly sensitive sensors [6], low-threshold lasers [7], and highly efficient light-emitting diodes [8]. While many applications of PhCs focus on room and cryogenic operating temperatures, development for high temperature applications have been lacking.

1.1 Thesis Motivation and Goals

The nascent field of high temperature nanophotonics could potentially enable many important applications, for instance highly efficient infrared sources that are selective in wavelength and angle, and solid-state energy conversion applications, such as thermophotovoltaic (TPV) energy generation, and selective solar absorption. However, special challenges arise when trying to design nanophotonic materials with precisely tailored optical properties that can operate at high temperatures ($>$ 1100 K). These include: proper material selection and purity to prevent melting, evaporation, or chemical reactions; minimization of any material interfaces to prevent thermomechanical problems such as delamination; robust performance in the presence of surface diffusion; and long range geometric precision over large areas with minimization of very small feature sizes to maintain structural stability. In this thesis, we will explore an approach for high temperature nanophotonics that surmounts all of these difficulties. Moreover, the underlying physics will be uncovered, leading to design handles that enable optimization for various applications. As a proof of concept, we aim to fabricate optimized designs, and perform extensive optical characterization. In addition, to quantify the benefits of such an approach, we will put to test an optimized design

in a realistic TPV system level numerical model. Finally, we aim to construct a TPV experimental setup to demonstrate the enhancement in performance.

1.2 Organization of the Thesis

In Chapter 2, we will uncover the physics behind the enhancement of emission for two-dimensional (2D) metallic photonic crystals (MPhCs), upon which enables us to utilize simple design rules to obtain an optimized structure. The fabrication and characterization of 2D MPhCs will then be discussed, before concluding with an extensive numerical study on the effect of fabrication disorders. In Chapter 3, we will evaluate the potential performance enhancements of implementing optimized 2D MPhCs in target TPV applications using a highly accurate system level numerical model. Comparisons will then be made with other TPV systems with or without different experimentally realized spectral control components. In addition, we will uncover key parasitic losses afflicting TPV systems that are realizable to-date. In Chapter 4, we will explore dielectric filling of the cavities of the 2D MPhC to improve on omnidirectional emittance, which is vital for certain applications, for instance as an emitter in TPV systems. In Chapter 5, we will investigate the viability of conventional silicon (Si) solar cell based TPV systems that are enhanced with optimized PhC selective emitters and cold-side filters. This chapter will also describe the experimental apparatus used to accurately measure the key performance metrics of TPV systems. Results of TPV efficiency measurements will also be discussed. Finally, we will summarize our findings and provide suggestions for future research directions in Chapter 6.

1.3 Thesis Contributions

Major contributions of this thesis are as follows:

- Demonstrated how thermal emission of 2D MPhCs can easily be optimized for a particular system, resulting in near-ultimate short-wavelength emittance for this architecture. Bandgap edge of PhC can be tailored theoretically to any wavelength of interest, limited only by intrinsic material properties and fabrication limits, by virtue of controlling the cavity's resonant

frequency. Using this, PhC designs for bandgaps important in typical TPV systems were demonstrated. The optimization method also enables designs with maximum emission at larger wavelengths previously unattainable with this material platform.

- Fabricated representative designs using standard nanofabrication techniques amenable to wafer scale batch processing. Modifications were made to allow for deeper, larger, and more uniform cylindrical holes, as well as ensuring a contamination free surface. The samples were also optically characterized both at room temperatures via indirect reflectance measurements, and at high temperatures via direct thermal emission measurement, both of which agree extremely well with numerical predictions.

- Extensively investigated the effects of fabrication disorder vital for future improvements via numerical methods. The disorders studied include tapering of sidewalls, sidewall roughness, breakage of sidewalls, and surface contamination.

- Developed numerical model that accurately predicts radiant heat-to-electricity efficiency and power density of TPV systems. The numerical model incorporates physical properties of the hot-side emitter, cold-side filter, and photovoltaic (PV) cell. Using this, the improvement seen when implementing optimized 2D MPhCs was quantified. In addition, factors of inefficiencies present in the best TPV systems that can be assembled to-date were identified, leading to recommendations for future research efforts.

- Demonstrated optimized designs of dielectric-filled anti-reflection coated (ARC) 2D MPhCs with vastly superior omnidirectional broadband selective emission compared to the unfilled 2D MPhCs.

- Demonstrated theoretically a maximum radiant heat-to-electricity efficiency of 6.4% and electrical power density of $0.4\,\mathrm{W\,m^{-2}}$ at temperature of 1660 K when implementing an optimized 2D tantalum (Ta) PhC emitter in combination with an optimized dielectric 1D PhC based cold-side filter in conventional Si solar cell based TPV systems. An experimental setup was also built and the measurements were shown to agree extremely well with the numerical model developed.

Chapter 2

Two-dimensional Metallic Photonic Crystals for Selective Emission

This chapter presents a detailed exploration of the optical properties of the 2D metallic cylindrical cavity square lattice PhC slab. Through understanding of the physics behind the enhancement of emission, we uncover simple design rules that enable optimization of selective emission for specific applications. We further show that fabricated 2D MPhCs possess optical properties that agree extremely well with numerical models, both at room and high temperatures. Finally, we present extensive numerical investigation into the effects of fabrication disorders.

2.1 Introduction

Ever since photonic bandgaps were predicted to exist in PhCs [1–3], significant interest has garnered in recent years to exploit this property. In particular, MPhCs have been shown to possess a large bandgap [9–12], and consequently superior modification of the intrinsic thermal emission spectra is readily achievable. This is extremely promising for many unique applications, especially high efficiency energy conversion systems encompassing hydrocarbon and radioisotope fueled TPV energy conversion [13, 14], as well as solar selective absorbers and emitters for the emerging field

of solar thermal, including solar TPV [15–18] and solar thermochemical production of fuels [19]. The selective emitters can also be used as highly efficient infrared (IR) radiation sources for IR spectroscopy and sensing applications including highly selective gas and chemical sensing [20, 21].

To date, PhCs have been designed to achieve both highly selective narrowband thermal emission exhibiting wavelength, directional, and polarization selectivity [22–24], as well as broadband thermal emission spectra close to blackbody within the design range but suppressed emission otherwise [12, 17, 25–28]. In this investigation, we focus on the design, optimization, fabrication, and characterization of the high performance broadband selective emitter with critical emphasis on obtaining optimized optical response providing the necessary bandwidth that translates into higher power density imperative for large scale solid-state energy conversion, high temperature performance, and long range fabrication precision over large areas. In this respect, notable experimental efforts include 2D square cavities fabricated on tungsten (W) using e-beam lithography and fast atom beam etching [27], and the woodpile stacked 3D W PhC fabricated using a layer-by-layer modified Si process [12, 26, 29].

However, in order to effectively apply nanophotonic materials in emerging high temperature large scale energy conversion systems, it is imperative to simultaneously achieve high temperature stability, sharp contrast between regions of enhanced and suppressed emission, and precise fabrication of periodic nanostructures over large areas while maintaining macroscopic correlation lengths and ensuring a contamination free surface. The proposed solution in this chapter overcomes these challenges, thus paving the way to what is an emerging new field of high temperature nanophotonics for energy conversion applications.

This chapter starts by explaining the physics behind the enhancement of emission, which leads us to design handles critical for optimization purposes. In addition, the angular dependence of the PhC emitter will be uncovered. Next, representative designs fabricated using standard nanofabrication techniques amenable to wafer scale batch processing are presented. Results of optical characterization at room temperature and high temperature are then shown. Instead of using physical methods for surface temperature measurement, which is extremely challenging at such high temperatures [30], resulting in erroneous estimations, we will demonstrate a method of esti-

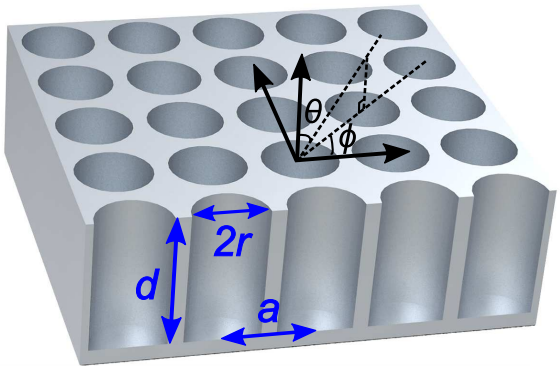

Figure 2-1: Two-dimensional (2D) metallic photonic crystal (MPhC) slab. The holes have period a, radius r, and depth d. The polar and azimuthal angles are designated by θ and ϕ respectively.

mation of the surface temperature accurate to within $\approx 3\%$ relative uncertainty. Finally, the effects of fabrication disorders are discussed. Note that a condensed version of this chapter is reported in Ref. 31.

2.2 Theory and Design

The majority of reported selective emitter/absorber designs have focused extensively on multilayer and multimaterial structures [32], as well as metal-dielectric composite coatings (cermets) [33]. However, these designs cannot operate at high temperatures ($> 1000\,\mathrm{K}$) due to thermomechanical stresses between layers and interfaces, and chemical reactions between the constituent elements that are initiated at elevated temperatures. Even 3D layer-by-layer structures, such as W woodpile PhC contain multiple interfaces [12, 26, 29], thus making them fragile. To overcome the aforementioned shortcomings, we have selected a material platform consisting of robust, single element, broadband tunable spectrally selective IR emitters comprised of a 2D square array of cylindrical holes with period a, radius r, and depth d etched through a large area metallic surface as shown in Fig. 2-1. This relatively simple design allows one to simultaneously achieve near-blackbody emittance ε at short wavelengths as well as ε almost as low as a polished metal at long wavelengths, with a sharp cutoff separating the two regimes. This is especially critical for high efficiency energy conversion.

For this investigation, we have chosen W as the material of choice, firstly due to its superior ability in withstanding high temperatures (high melting point of $3695\,\mathrm{K}$, low vapor pressure of

1 Pa at 3477 K), which makes it particularly suitable for very high temperature applications with proper vacuum packaging. Specifically, we select 99.999% pure single crystal W to ensure superior optical performance and minimal surface diffusion at high temperatures. In addition, W has an intrinsically low ε at wavelengths $\lambda > 2.5\,\mu m$ as shown in Fig. 2-2(a). Suppression of these photons is vital for higher TPV system efficiencies since these photons are generally below the bandgap of current state of the art low bandgap TPV cells. More importantly, the increasing ε at $\lambda < 2.5\,\mu m$ due to interband transitions also enables us to easily enhance emission within $1.5\,\mu m < \lambda < 2.5\,\mu m$, which is vital for efficient TPV energy conversion. This intrinsic wavelength selectivity is also necessary for application as an efficient solar selective absorber characterised by strong solar absorption and low thermal emission.

Previous demonstration of the 2D W PhC in our group achieved enhancement in emission for $\lambda < 1.5\,\mu m$ as reported in Ref. 28. Achieving high emission for cutoff wavelengths $\lambda_c > 1.7\,\mu m$, which is imperative to extend the range of possible applications, proved elusive as the intrinsic ε of W is low at $\lambda > 1.7\,\mu m$. In order to make further inroads, let us first uncover the physics behind the enhancement in emission.

In general, the enhancement in emission is achieved by coupling into resonant cavity electromagnetic modes. In such systems, λ_c is approximately given by the fundamental mode of the cylindrical metallic cavity as described by previous work in our group published in Ref. 28. For radiation with frequencies larger than the fundamental cavity resonance frequency, enhanced absorption occurs due to the increased interaction time of the radiation with the absorptive metal. On the other hand, radiation with frequencies lower than the fundamental cavity resonance frequency is forbidden from entering the cavities, thus maintaining the desired wavelength selectivity. In this regime, the effective medium theory holds; the increased surface area fraction of air-to-metal decreases the index contrast, resulting in a slightly lower reflectance R, and consequently increased absorptance α.

The resonance frequency of the fundamental electromagnetic cavity mode, and hence λ_c, is mainly affected by r, with d playing only a secondary role for the aspect ratios considered [28, 34]. This phenomena is clearly seen in Fig. 2-2, the results of which were obtained using finite difference

time-domain (FDTD) simulations [35] implemented via MEEP, a freely available software package developed at MIT [36]. In this method, a plane wave is launched from the normal direction and propagated through space. On each grid point of a flux plane defined at the front and back of the computational cell, the electric and magnetic fields are Fourier-transformed via integration with respect to preset frequencies at each time-step. At the end of the simulation, the Poynting vector is calculated for each frequency and integrated across each plane, which yields the total transmitted and reflected power at each frequency. The dispersion of W is captured via the Lorentz–Drude model, fit both to room temperature and elevated temperatures [37]. Apart from the approximations of material dispersions and grid discretization, these calculation methods are exact. ε of each structure can be calculated from α computed above via Kirchhoff's law of thermal radiation, which states that α and ε must be equal at every λ for a body in thermal equilibrium [38].

As can be seen in Fig. 2-2(a), reliance on r alone is insufficient in maximizing the ε peaks below λ_c. In fact, as λ_c is further increased, the peak ε of the fundamental mode decreases for a fixed d. This is due to the intrinsic α of flat W that decreases as λ increases as shown in Fig. 2-2(a). In order to further enhance the selective emitter's performance, we further explore the role of d by fixing r. As can be seen in Fig. 2-2(b), the peak ε of the fundamental resonant mode is strongly affected by d. In addition, as d increases, the number of resonances within $1\,\mu\text{m} < \lambda < 2\,\mu\text{m}$ increases, which indicates the importance of d in increasing ε below λ_c.

It can easily be understood that the increase of d increases the interaction time with the absorptive metal, thus elevating ε. However, there is a strong indication that an optimum d exists in ensuring peak ε of 1 at the resonance λ of the fundamental mode as shown in Fig. 2-2(b). To understand the reason behind the existence of an optimum d, we relied on coupled-mode theory [39]. Following this approach, it was found that complete absorption of incident radiation occurs when the radiative (Q_{rad}) and absorptive quality factors (Q_{abs}) of the PhC cavity resonances are matched, i.e. satisfying the Q-matching condition [34]. If free space radiation is undercoupled to the PhC cavity resonances ($Q_{\text{rad}} > Q_{\text{abs}}$), insufficient radiation enters the cavity, resulting in suboptimal absorption. On the other hand, if free space radiation is overcoupled to the PhC cavity resonances ($Q_{\text{abs}} > Q_{\text{rad}}$), the radiation escapes before it is completely absorbed. Hence, in order to obtain

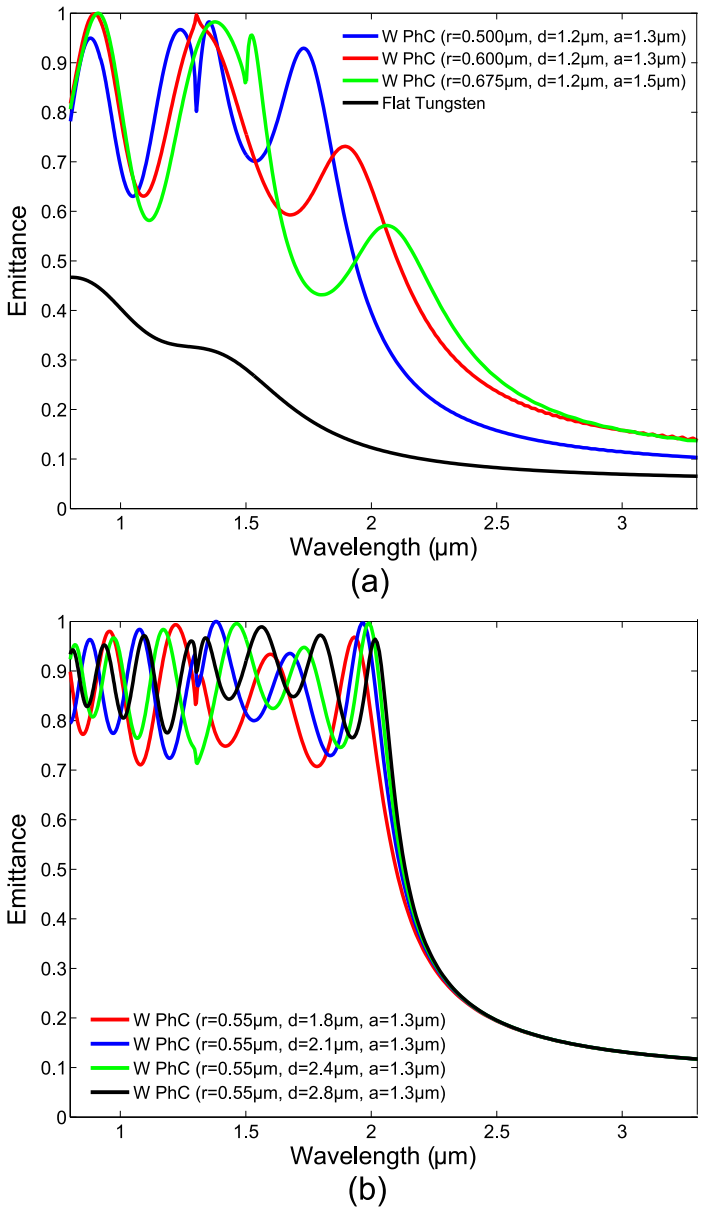

Figure 2-2: Effect of (a) the radius r and (b) the depth d on normal incidence emittance ε of 2D tungsten (W) PhCs. As can be seen, the resonance frequency of the fundamental cavity mode, which determines the cutoff wavelength λ_c, is mainly affected by r, with d playing only a secondary role for the aspect ratios considered. Nevertheless, selection of the appropriate d is imperative to achieve maximum ε at $\lambda < \lambda_c$. In addition, as d increases, the number of resonances within 1 μm $< \lambda <$ 2 μm increases, which indicates the importance of d in increasing ε below λ_c.

maximum peak ε that approaches the theoretical blackbody in the vicinity of the designated λ_c, the Q-matching condition for the fundamental mode has to be satisfied.

Following the analysis in Ref. 34, it was found that for a particular choice of r, there is only one value of d that satisfies the Q-matching condition for the fundamental mode, i.e. an optimal pair of r and d exists for a particular λ_c. Note that a only strongly affects ε at $\lambda \leq a$, whereupon diffracted plane waves (see Section 2.2.1) start to appear, causing ε to degrade. This can be understood through the coupled-mode picture, whereby the resonances couple to a number of planewaves fixed by a. Therefore, the cavity's Q_{rad} decreases as there are more channels to couple to, resulting in the loss of Q-matching and consequently suboptimal emission. It is thus important to choose the smallest possible a for a fixed r (limited only by sidewall thickness that must be thicker than the skin-depth of the metal to preserve the wavelength selectivity of the emitter) in order to achieve the intended broadband high ε. However, adequate sidewall tolerances ($\approx 100\,\mathrm{nm}$) must be included to ensure robustness to fabrication disorders, hence a would have to be slightly larger than optimal. In addition, very small sidewall thicknesses could potentially lead to breakage (due to diffusion, melting, or mechanical stress), which would destroy the connectivity of the structure, leading to a compromised optical response, particularly a dramatic increase in ε at long wavelengths.

To illustrate the unprecedented control that resonant Q-matching brings to shaping the thermal emission, we show in Fig. 2-3 three different 2D W PhC designs that exhibit peak ε approaching the blackbody at $1.70\,\mu\mathrm{m}$, $2.00\,\mu\mathrm{m}$, and $2.30\,\mu\mathrm{m}$, obtained solely by matching Q_{rad} and Q_{abs} of the fundamental cylindrical cavity resonance. These designs demonstrate the ease of simultaneously matching the electronic bandgaps and photonic bandgaps in TPV systems utilizing gallium antimonide (GaSb) [40], indium gallium arsenide (InGaAs) [41, 42], and indium gallium arsenide antimonide (InGaAsSb) TPV cells [43, 44].

2.2.1 Angular Dependence of Emittance

Previous research in the group, and in fact many other research efforts on selective emitters [12, 17, 23, 25, 26, 28, 32, 45], did not explore the dependence of ε with respect to angle of exitance. Yet, it is imperative to fully understand the angular dependence of ε in order to fully evaluate the impact

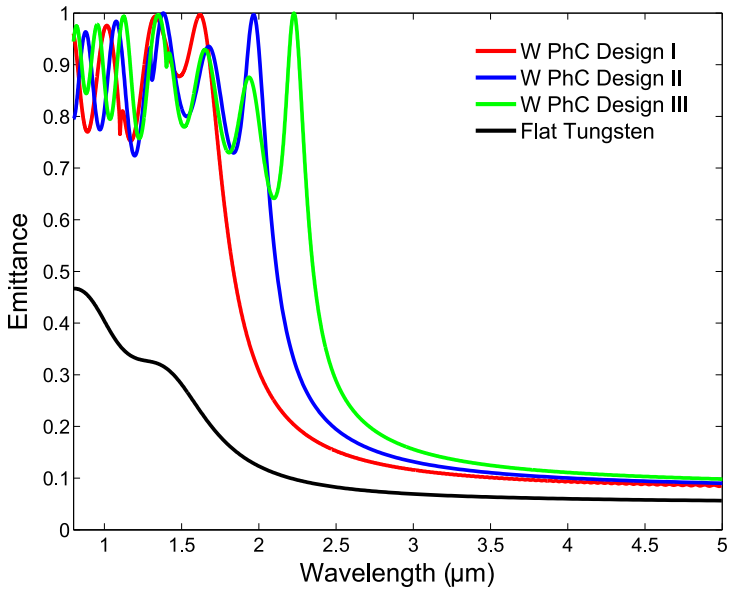

Figure 2-3: Simulated normal ε for 2D W PhC Design I ($r = 0.45\,\mu\text{m}$, $a = 1.10\,\mu\text{m}$, $d = 1.50\,\mu\text{m}$), 2D W PhC Design II ($r = 0.55\,\mu\text{m}$, $a = 1.30\,\mu\text{m}$, $d = 2.10\,\mu\text{m}$), 2D W PhC Design III ($r = 0.625\,\mu\text{m}$, $a = 1.40\,\mu\text{m}$, $d = 2.80\,\mu\text{m}$) with the first peak in the vicinity of $1.70\,\mu\text{m}$, $2.00\,\mu\text{m}$, and $2.30\,\mu\text{m}$ respectively.

of 2D MPhCs in target applications. Hence, in this subsection, we explore the angular dependence of the 2D MPhC using FDTD methods. The simulations can easily be performed by varying the parallel k-vector $\boldsymbol{k}_{\parallel}$ (the component of the wavevector in the xy-plane) for each λ to obtain the desired polar and azimuthal angle, which is respectively designated with θ and ϕ as illustrated in Fig. 2-1.

The results of the numerical simulations for 2D W PhC Design II are shown in Fig. 2-4. Since the variation of ε is small with respect to polarization and ϕ for a fixed θ, the results are averaged over both polarizations and ϕ. Evidently, frequency selectivity is strong; the location of the resonant peaks and hence λ_c is virtually unchanged with respect to θ. This reflects the fact that the resonant peaks are due to coupling of free space radiation with hole resonances that satisfy Q-matching conditions. However, ε starts to drop significantly above a certain θ. For instance, the high ε peak due to the fundamental cavity resonance starts dropping when $\theta \gtrsim 35°$. To understand this phenomenon, let us first review the fundamentals of a diffraction grating, which is governed by the

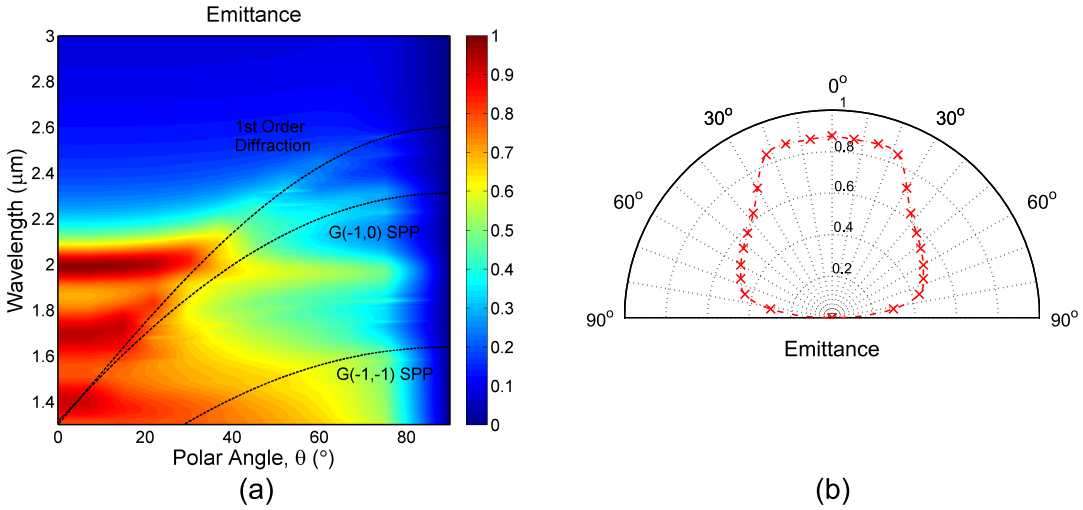

Figure 2-4: (a) ε as a function of θ averaged over polarization and ϕ for 2D W PhC Design II with $\lambda_c \approx 2\,\mu m$. The dotted lines represent the onset of 1st order diffraction and resonant modes associated with surface plasmon polaritons (SPPs). Due to the reduction in Q_{rad} for $\theta > \theta_d$, i.e. the polar angle at the onset of diffraction for a particular λ, Q-matching of the resonances is destroyed, leading to a dramatic reduction in ε. (b) Average ε below λ_c as a function of polar angle for 2D W PhC Design II. As can be seen, the emitter maintains maximum emission for $\theta < 30°$, and is suppressed by 50% at 75°.

following grating equation:

$$a(\sin\theta_i + \sin\theta_p) = p\lambda, \quad p = \pm1, \pm2, \pm3, ... \tag{2.1}$$

where θ_i is the radiation's angle of incidence and θ_p is the angle where the p-th order diffraction lies. The onset of diffraction occurs when $p = 1$ and $\theta_p = 90°$. Thus, at normal incidence ($\theta_i = 0°$), diffraction order(s) is (are) present for $\lambda \leq a$. For radiation with a specific λ incident on the PhC, diffraction sets in when θ_i is larger than the polar angle given below:

$$\theta_d = \sin^{-1}\left(\frac{\lambda}{a} - 1\right) \tag{2.2}$$

For 2D W PhC Design II, radiation with $\lambda = 2\,\mu m$ will get diffracted when $\theta_i > \theta_d = 32.6°$. Above the diffraction threshold, α decreases because there are more channels to couple into, resulting in a smaller Q_{rad}, thus destroying Q-matching. Therefore, at larger incident polar angles, the in-band

absorption region decreases and has a lower average α as can be seen in Fig. 2-4. Regardless, Q-matching is satisfied up to the diffraction threshold, thus the emitter maintains maximum emission for $\theta_{\mathrm{i}} < \theta_{\mathrm{d}}$. Depending on the application, this angular selectivity may be beneficial. For instance, solar absorbers in solar thermal applications can substantially benefit from both frequency and angular selectivity [46–48], whereby solar α is high at normal incidence, and thermal ε is reduced due to lower integrated hemispherical ε.

ε of 2D MPhCs at larger θ_{i} is also influenced by surface plasmon-polaritons (SPPs). SPPs are longitudinal modes that propagate along the surface of metals and are confined within the air-metal interface [49]. The SPP dispersion relation is given by:

$$|\boldsymbol{k}_{\mathrm{SPP}}| = \frac{\omega}{c}\left(\frac{\epsilon_{\mathrm{m}}}{1+\epsilon_{\mathrm{m}}}\right)^{1/2} \tag{2.3}$$

where ω is the angular frequency, c is the speed of light, and ϵ_{m} is the real part of the metal dielectric function. Since $|\boldsymbol{k}_{\parallel}|$ of free space radiation is always smaller than $|\boldsymbol{k}_{\mathrm{SPP}}|$, free space radiation cannot directly excite SPP modes on a smooth surface. The situation changes however when periodicity is present as in the case of the 2D MPhC; in this case SPPs can be generated through Umklapp scattering as the periodicity is able to provide the additional $\boldsymbol{k}_{\parallel}$ momentum via surface reciprocal lattice vectors $\boldsymbol{G}$:

$$\boldsymbol{k}_{\parallel} + \boldsymbol{G} = \boldsymbol{k}_{\mathrm{SPP}} \tag{2.4}$$

Using Eqs. (2.3) and (2.4), the approximate ω of SPPs in 2D square lattice PhCs at specific θ and ϕ can be determined as follows:

$$\frac{\epsilon_m}{1+\epsilon_m} = \left(\sin\theta\cos\phi \pm \frac{iG_x}{\omega/c}\right)^2 + \left(\sin\theta\sin\phi \pm \frac{jG_y}{\omega/c}\right)^2 \tag{2.5}$$

where $\boldsymbol{G} = \boldsymbol{x}G_x + \boldsymbol{y}G_y$, and i and j are integers. The different SPP modes can thus be differentiated using the notation $\mathrm{G}(i,j)$.

Using Eq. (2.5), the lowest and 2nd order SPP modes $\mathrm{G}(-1,0)$ and $\mathrm{G}(-1,-1)$ for 2D W PhC Design II are solved and plotted in Fig. 2-4(a). Since the enhancement in ε for 2D W PhC Design

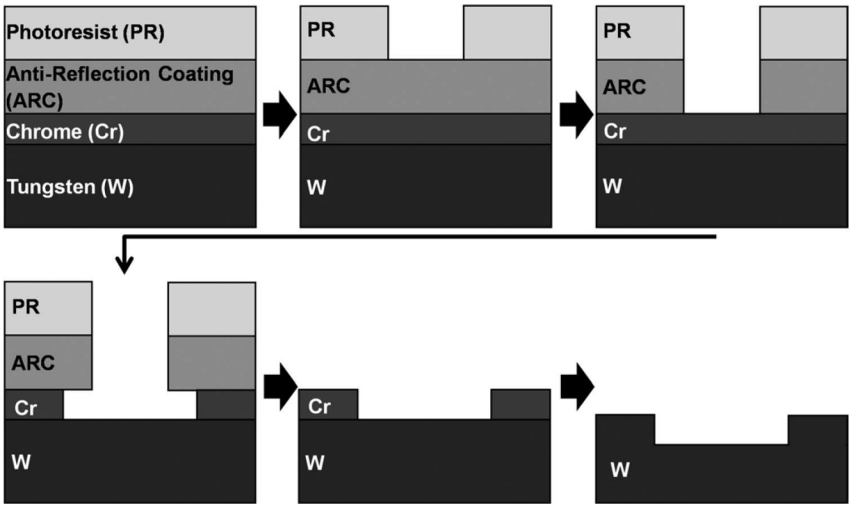

Figure 2-5: 2D W PhC fabrication process: After depositing a layer of chrome (Cr) on the W substrate, a thin layer of anti-reflection coating (ARC) and photoresist is spin coated. After lithographic exposure, the desired pattern is transferred from one layer to the next layer via various etching processes until periodic cylindrical holes are obtained on the W substrate.

II is dominated by the Q-matched electromagnetic cavity modes, SPP modes are only weakly observed. It is also observed in Fig. 2-4 that a slight enhancement in ε occurs for $\lambda > \lambda_c$ along the 1st order diffraction line whereby radiation is traveling along the surface of the PhC slab. Again, the enhancement is weak due to unmatched Q's.

2.3 Fabrication

The first 2D W PhC prototypes fabricated in our group were based on interferometric lithography using a two-layer resist process with a thin layer of chrome (Cr) as the hard mask for etching into a single side polished single crystal W samples 10 mm in diameter using carbon tetrafluoride (CF_4) based reactive ion etching (RIE) [28, 50, 51]. The procedure is summarized as follows (see Fig. 2-5 for a graphical summary):

1. A thin layer of Cr is e-beam deposited on top of the single crystal W substrate, which is then subsequently spin coated with 300 nm of AZ Photoresist's BARLi ARC and 250 nm of OHKA America's THMR-iNPS4 photoresist.

2. The photoresist is exposed using a Lloyd's mirror interference lithography system with expanded beam from a 50 mW 325 nm helium-cadmium (HeCd) Laser. The exposure is performed twice, with the second exposure perpendicular to the first to create a square array of cylindrical cavities. The interference angle is chosen such that the desired periodicity is obtained. After photoresist development, the diameter of the cylindrical cavities is much smaller than in the desired final structure.

3. Holes produced in the resist layer are transferred into the ARC via helium–oxygen (He–O_2) based RIE respectively using the Plasma Therm 790.

4. With the Cr mask now exposed, the sample is immersed into Cr-7 (Cyantek) liquid etchant diluted with 40% distilled water to slow down the etch rate, thus ensuring a more repeatable process. The duration of the wet etch is calibrated to obtain the desired diameter on the Cr hard mask. Subsequently, the ARC coating layer is removed.

5. The Cr hard mask allows pattern transfer to the W substrate using a CF_4–O_2 based RIE. Etching of W is optimized with the following parameters: flow rate 6.7 sccm of CF_4 and 1 sccm of O_2 at 10 mTorr pressure with plasma conditions at 250 V and 90 W. The etch rate is about 10 nm of W per minute and the etch selectivity ratio to the Cr hard mask is approximately 10:1 under these conditions.

6. Cr hard mask is removed with Cr-7 liquid etchant.

Using this procedure, samples with d up to 600 nm were successfully fabricated, with enhancement in emission limited to $\lambda < 1.5$ µm as reported in Ref. 28. To achieve $\lambda_c > 1.5$ µm as illustrated in Fig. 2-3, d has to be > 1.5 µm. Hence, for this investigation, the thickness of Cr mask was increased to > 150 nm. However, due to equipment limitations, we were only able to deposit a maximum Cr layer thickness of 250 nm, thus we were limited to $d \lesssim 2.5$ µm.

The necessity of a larger d and subsequently the requirement of a thicker Cr mask (5x thicker), and larger r (1.5x larger) compared to the work reported in Ref. 28, however, led to a multitude of problems, the first being the difficulty in controlling the random variations in sidewall roughness

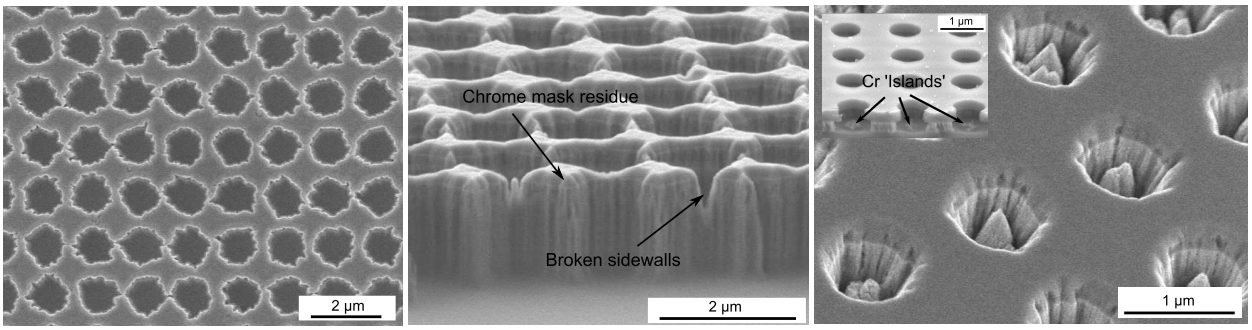

Figure 2-6: Possible fabrication disorders due to new design requirements: (a) Top view of 2D W PhC sample with random variations in sidewall uniformity. (b) Side view of 2D W PhC sample. Broken sidewalls and Cr mask residue are clearly seen, both of which result in highly undesirable elevated long wavelength emission. (c) Formation of 'islands' within cylindrical cavities due to Cr residue, as shown in inset. As Cr mask thickness is increased, it becomes progressively difficult to ensure repeatability of Cr wet etch process.

as observed in Fig. 2-6(a) due to the necessary longer etch times with Cr-7. Secondly, due to the requirements that $2r$ be smaller than a by a few skin depths for optimum emission below λ_c, it is easy to break the sidewalls as illustrated in Fig. 2-6(a) & (b). This results in elevated long wavelength emission as the effective cavity size is increased (see Section 2.5 for further details on the effects of fabrication disorders). Fortunately, it was discovered that sidewall roughness of the Cr mask can be minimized by ensuring clean deposition conditions as shown in Fig. 2-7. Elevating the process temperature to 250°C could also help ensure deposition of a higher quality Cr mask.

The thicker Cr mask requirement also occasionally resulted in incomplete and uneven etching of the Cr mask, leading to formation of 'islands' in the final 2D W PhC sample as illustrated in Fig. 2-6(c), which reduces the effective cavity depth, leading to suboptimal emission below λ_c. Lastly, subjecting the Cr mask to prolonged RIE ion bombardment to obtain larger d seems to lead to Cr mask hardening / alloy formation with W, resulting in difficulty in complete removal with the Cr-7 wet etchant (see Fig. 2-6(b)) and consequently elevated long wavelength emission. Thus in the final RIE etching process of W, it is important to be conservative to ensure sufficient pure Cr remained at the bottom of the mask to ensure a more thorough removal.

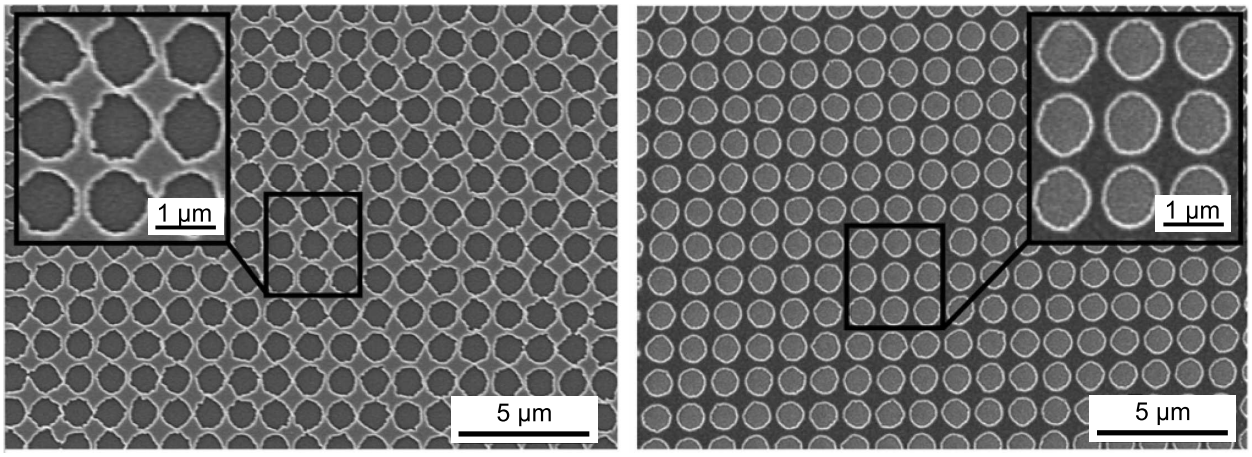

Figure 2-7: (a) Cr mask with relatively rougher sidewalls (b) Cr mask with smooth sidewalls. This can be achieved by ensuring clean deposition conditions, i.e. after a scheduled maintenance on the e-beam deposition chamber. Elevating the chamber temperature during deposition may also help.

After multiple attempts with the modified fabrication process, two samples were fabricated from single crystal W: the first has $\lambda_c \approx 1.70\,\mu m$ (2D W PhC Sample I) and the second has $\lambda_c \approx 2.00\,\mu m$ (2D W PhC Sample II). Images of the latter are shown in Fig. 2-8. As can be seen, long range uniformity is achieved across a large area. In order to determine the depth of the cavities accurately, tapping mode atomic force microscopy (Veeco Nanoscope IV Multimode AFM with Nanoscience Instruments High Aspect Ratio Silicon AFM tips) was used. For 2D W PhC Sample I and 2D W PhC Sample II, the depth was found to be approximately 1.30 µm and 1.60 µm respectively. Note that due to the limitations of the RIE machine we were using, we were unable to etch deeper than $\approx 1.60\,\mu m$. This however could easily be circumvented with access to a deep reactive ion etching (DRIE) tool.

2.4 Optical Characterization

2.4.1 Room Temperature Emittance

The room temperature normal ε of the fabricated samples, approximated via Kirchhoff's Law from near-normal R measurements obtained using the OL 750 spectroradiometer, are compared with

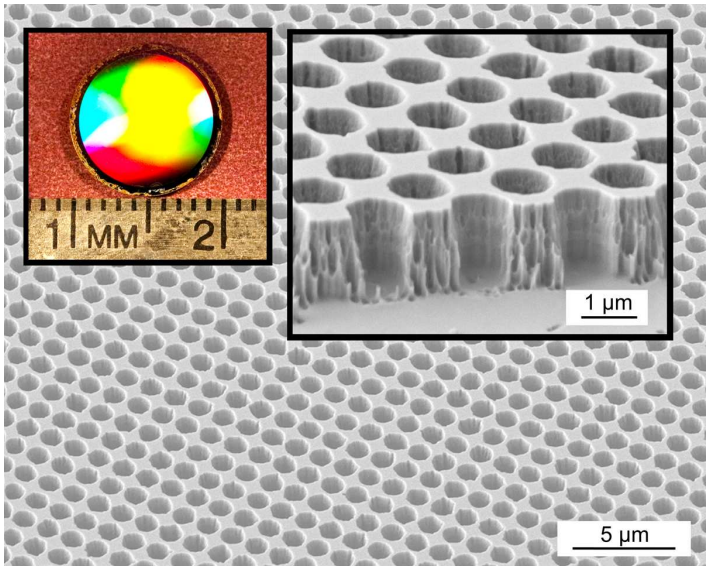

Figure 2-8: Scanning electron micrograph of fabricated 2D W PhC Sample II ($r = 0.55\,\mu m$, $a = 1.40\,\mu m$, $d = 1.60\,\mu m$) over a large area, showing excellent uniformity. Interference lithography and standard reactive ion etching (RIE) techniques were used to fabricate the samples. Left inset: Digital photo of the full 1 cm diameter sample. Right inset: Magnified cross sectional view of 2D W PhC Sample II.

FDTD simulations in Fig. 2-9. As can be seen, excellent agreement is seen between the measurements and the simulations; the resonant peaks match in wavelength as well as magnitude. The slight broadening and dampening of the resonances are expected due to small non-uniformities, including slightly uneven profile of the cavities and sidewall disorder due to the isotropic stochastic nature of the chemical wet etching technique used. Nevertheless, the performance is almost unaffected and this shows the robustness of the design to fabrication disorders (effect of fabrication disorders will be further discussed in Sec 2.5). In fact, this brings the emitter closer to blackbody performance below λ_c, which translates into higher power density for energy applications. Since we were unable to obtain $d > 1.6\,\mu m$, the magnitude of the peak intended at $2.0\,\mu m$ is lower than desired.

2.4.2 High Temperature Emittance

While room temperature R measurements allow indirect confirmation of ε, it is important to obtain direct thermal emission data to demonstrate the viability of the approach at high temperatures.

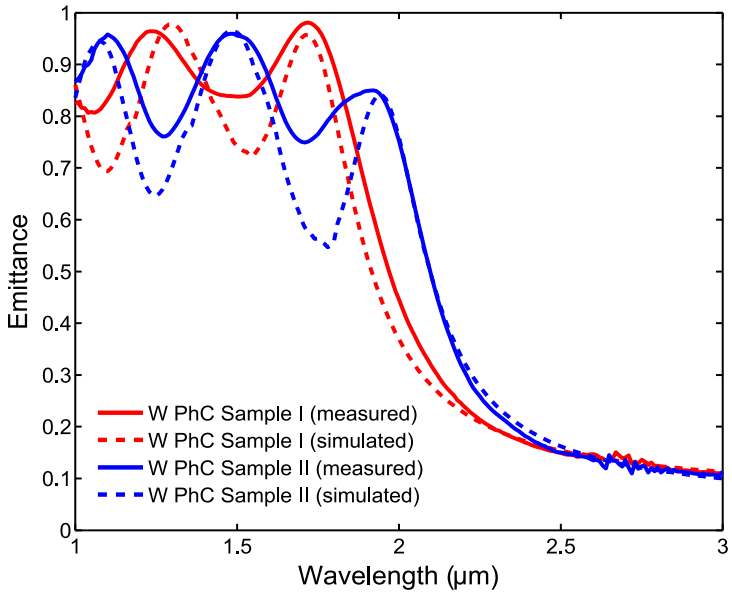

Figure 2-9: Measured (solid lines) and simulated (dotted lines) room temperature near-normal ε of the fabricated 2D W PhC Sample I ($r = 0.48\,\mu m$, $a = 1.22\,\mu m$, $d = 1.30\,\mu m$) and 2D W PhC Sample II ($r = 0.55\,\mu m$, $a = 1.40\,\mu m$, $d = 1.60\,\mu m$). ε is approximated from measurements of near-normal specular reflectance R via Kirchhoff's Law.

In this investigation, we have utilized the measurement setup and technique described in Ref. 52. This method requires emission measurements of a calibrated blackbody source (Omega BB-4A) at two temperatures, which then allows the instrument response function and background radiation at each wavelength to be calculated. Using this, the absolute normal spectral radiance of the samples can be extracted [53]. We then only need to know the surface temperature to compare the experimental measurements to simulations.

Fig. 2-10 illustrates the experimental setup used to obtain high temperature ε of the 2D W PhCs. The 2D W PhC sample was mounted on top of a HeatWave Labs 1-inch diameter ultra high vacuum (UHV) electrical heater (rated to 1200°C). Both the heater and the 2D W PhC sample were enclosed in a vacuum chamber that was evacuated to a base pressure of 10^{-6} Torr. An IR transparent calcium fluoride (CaF_2) window and Viton O-ring combination was used to seal the vacuum chamber whilst allowing IR radiation to exit. While delivering power to the heater, forming gas (5% hydrogen (H_2) – 95% nitrogen (N) gas mixture) was flowed to achieve a process pressure

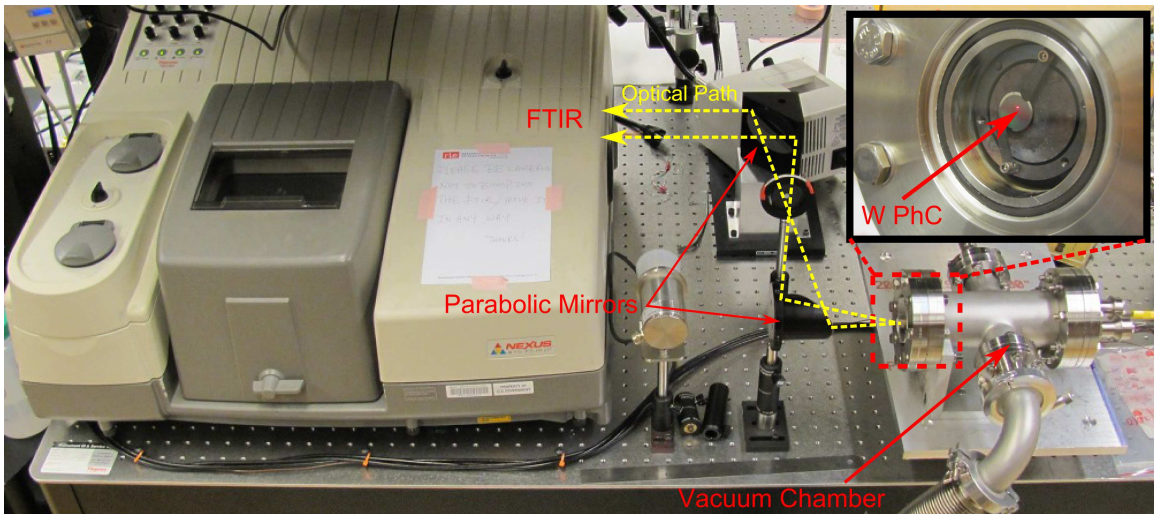

Figure 2-10: Experimental setup to obtain ε of 2D W PhCs at high temperatures (up to 1200 K). Inset shows 2D W PhC attached to heater with molybdenum (Mo) clips in a vacuum chamber. A calcium fluoride (CaF_2) window and Viton O-ring combination was used to seal the vacuum chamber, whilst allowing IR radiation to exit.

of around 30 mTorr to further prevent oxidation of samples. Radiation exiting from the CaF_2 window was then collimated into the emission port of a Nexus 870 Fourier Transform Infrared Spectroscope (FTIR) using two parabolic mirrors with a collection angle of $\theta \lesssim 5°$. By using an aperture in between the mirrors, we ensured that the signal obtained originates solely from the 2D W PhC sample surface. The FTIR's deuterated triglycine sulfate (DTGS) detector was used for the emission measurements.

In this experiment, accurate measurement of the emitter's surface temperature is important. However, due to the high temperatures (> 1000 K), large temperature gradients, and small samples involved, it is extremely challenging to obtain accurate measurements using physical sensing methods, e.g. using a thermocouple. In fact, erroneous estimations have been frequently obtained [30]. Fortunately, due to the temperature insensitivity of ε of the 2D MPhCs in the vicinity of the resonance peaks, as shown in Fig. 2-11, we can rely on room temperature emittance $\varepsilon_{\text{room}}$ measurements to accurately estimate the surface temperatures of our samples during the high temperature measurements. For instance, the first resonance peak has $\varepsilon_{\text{room}} \approx 0.98$, while at higher temperatures, the change in emittance $\Delta\varepsilon$ of this peak is $\lesssim 0.05$. This is highly unexpected as the dielectric constant

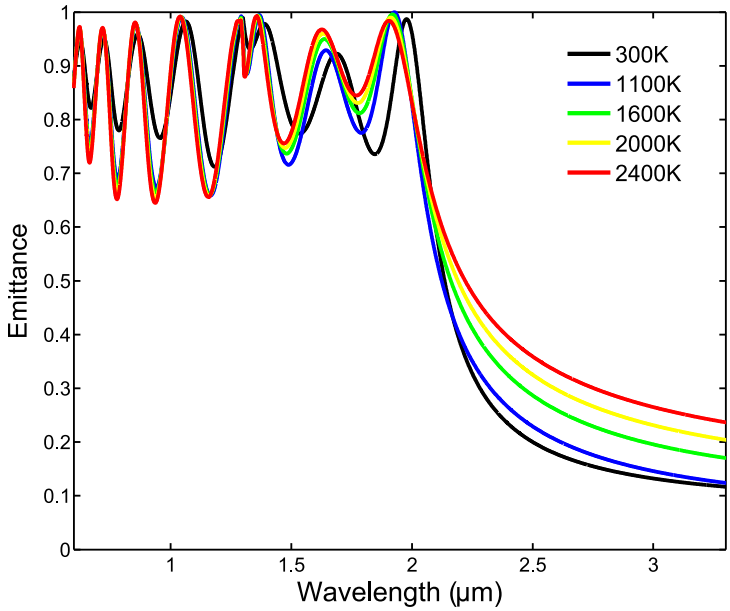

Figure 2-11: Comparison of simulated normal ε of 2D W PhC Design II at different temperatures. Simulations are performed using Lorentz-Drude parameters fitted to experimentally measured ε of flat W at various temperatures [37].

of W varies significantly with respect to temperature. In fact, ε of flat W at room temperature and at high temperatures can differ by more than 80% [37]. However, due to the relatively deep holes of Q-matched cylindrical cavities, the change in Q_{abs} is small with respect to temperature. This is because deep hole modes interact more weakly with the metal's surface. Hence, Q_{abs} and Q_{rad} are still fairly well matched. Consequently, ε in the vicinity of the resonances stays approximately constant with temperature. This allows us to approximate the emittance at high temperatures ε_{HT} with the following:

$$\varepsilon_{\text{HT}} = \varepsilon_{\text{room}} \pm \Delta\varepsilon \tag{2.6}$$

where $\Delta\varepsilon$ is the associated uncertainty of ε at high temperatures given $\varepsilon_{\text{room}}$ is used as the estimate. To determine the uncertainty in the temperature ΔT given $\Delta\varepsilon$, we start with the definition for $\varepsilon(\lambda, T)$, the emittance of the sample:

$$\varepsilon(\lambda, T) = \frac{L_{\text{s}}(\lambda, T)}{L_{\text{BB}}(\lambda, T)} \tag{2.7}$$

where T is the absolute temperature, and $L_{\mathrm{s}}(\lambda, T)$ and $L_{\mathrm{BB}}(\lambda, T)$ are respectively the spectral radiance of the sample and a blackbody. Hence, $L_{\mathrm{s}}(\lambda, T)$ is given by:

$$L_{\mathrm{s}} = \varepsilon(\lambda, T) \frac{2hc^2}{\lambda^5 \left(e^{\frac{hc}{\lambda k T}} - 1 \right)} \tag{2.8}$$

where h is Planck's constant, and k is Boltzmann's constant. T is then given by:

$$T = \frac{hc}{\lambda k \ln \left(\frac{2\varepsilon hc^2}{\lambda^5 L_{\mathrm{s}}} + 1 \right)} \tag{2.9}$$

Given a measurement $L_{\mathrm{s}}(\lambda, T)$, and the estimate of $\varepsilon \approx \varepsilon_{\mathrm{room}}$ around the regions of resonances, we can obtain the uncertainty in T using the following:

$$\Delta T = \sqrt{\left(\frac{\partial T}{\partial \varepsilon} \right)^2 (\Delta \varepsilon)^2 + \left(\frac{\partial T}{\partial L_{\mathrm{s}}} \right)^2 (\Delta L_{\mathrm{s}})^2} \tag{2.10}$$

Extensive calibration of our thermal emission measurement setup with a calibrated blackbody source at various T's showed that our spectral radiance measurements are accurate to $\Delta L_{\mathrm{s}}/L_{\mathrm{s}} < 1\%$. Since this is small in comparison to $\Delta\varepsilon/\varepsilon$, the relative uncertainty of T can be approximated by:

$$\frac{\Delta T}{T} \simeq \frac{\Delta \varepsilon}{\ln \left(\frac{2\varepsilon hc^2}{\lambda^5 L_{\mathrm{s}}} + 1 \right) \left(\varepsilon + \frac{\lambda^5 L_{\mathrm{s}}}{2hc^2} \right)} \tag{2.11}$$

The approximation scheme described can be applied, for instance around the resonant wavelength of 2 μm for 2D W PhC Sample II, where $\varepsilon_{\mathrm{room}} \approx 0.85$ as shown in Fig. 2-9. Even though the expected $\Delta\varepsilon$ as deduced from Fig. 2-11 is closer to 0.05 for perfectly Q-matched structures, a larger $\Delta\varepsilon$ of 0.15 is chosen here to reflect improvement in Q-matching expected for less than ideal structures. Even then, these parameters yield an estimate of the surface T of 2D W PhC Sample II to within a respectable $\approx 3\%$ relative uncertainty as can be determined using Eq. (2.11). With these T estimations, we are then able to compare our experimental results to simulations. The results agree extremely well as shown in Fig. 2-12. Note that for the estimation, we have neglected the small but experimentally observable increase in the fundamental mode's resonant frequency of

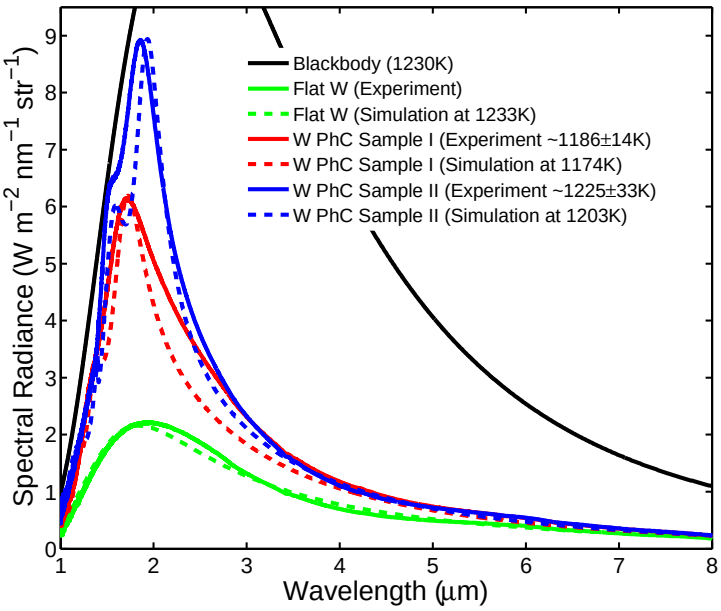

Figure 2-12: Comparison of measured and simulated normal emitted spectral radiance of fabricated samples. The thermal emission measured from the samples agree well with simulations and demonstrates the suppression of emission for $\lambda > \lambda_c$ and near blackbody performance for $\lambda < \lambda_c$.

$\approx 3\%$ at high T's, since the analysis focuses on the constancy of the ε magnitude. The increase is primarily due to the reduction of the skin depth at higher T's, leading to approximately 3% increase in the resonant frequency as can be seen in Fig. 2-11. Geometry changes due to thermal expansion can safely be neglected, as W has a very low thermal expansion coefficient of $6\,\mu\mathrm{m\,m^{-1}\,K^{-1}}$ [54], which results in geometry changes of less than 1%.

The samples were also subjected to repeated thermal cycling, i.e. heated to $T \approx 1200\,\mathrm{K}$ for an hour, before allowing to cool to room temperature. After several thermal cycles, R measurements show no measurable difference in the optical properties. Scanning electron micrographs also show the 2D W PhC samples keeping its original microstructure, including the $\approx 300\,\mathrm{nm}$ sidewall thickness, i.e. exhibiting no evidence of surface diffusion, thus demonstrating its stability at high T's under vacuum. Though our experiments indicate no degradation over 10 hours, further work is suggested to address stability issues over longer time scales (years).

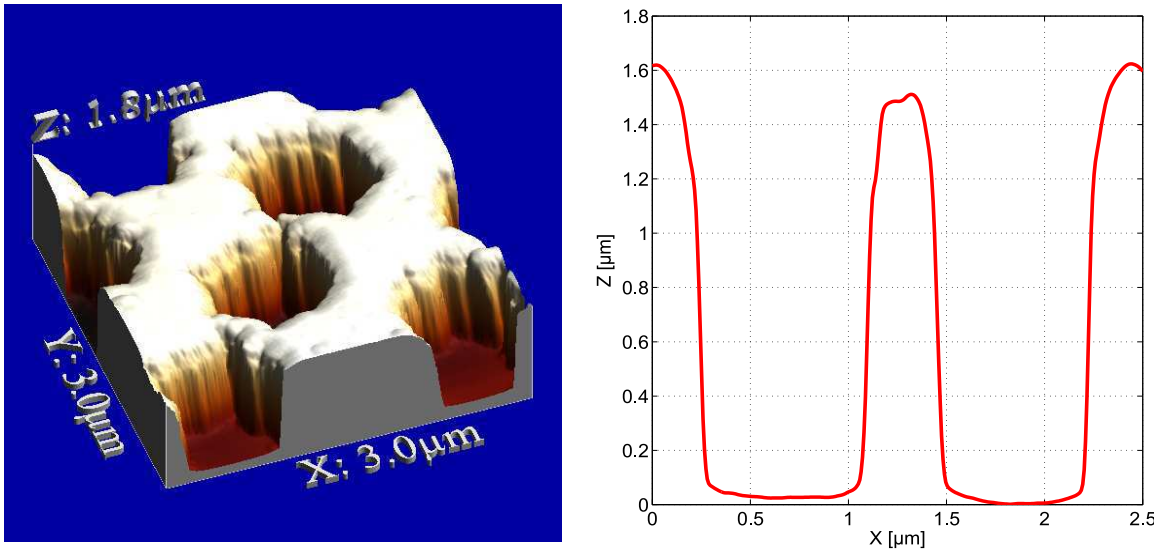

Figure 2-13: AFM results of fabricated 2D W PhC. (a) 3D Rendered Profile (b) 2D Profile

2.5 Effect of Fabrication Disorders

Here, the effects of various fabrication disorders that may occur on fabricated 2D MPhCs are explored using numerical simulations. They include tapering of the holes, sidewall roughness, and surface contamination. Note that the simulations to study fabrication disorders were performed using measured optical properties of tantalum (Ta) [37].

2.5.1 Tapering of Holes

AFM was used to investigate the profile of the cylindrical cavities of the fabricated samples. As can be seen in Fig. 2-13, tapering of the cylindrical cavities is evident; r at the base of the cavities is smaller by about 200 nm compared to the opening at the top. Consider the model shown in the inset of Fig. 2-14, where the diameter is reduced by 50 nm increments four times leading to a total reduction of 200 nm at the base of the cavity. The five regions with different r's are split to the ratio of 1:4:5:9:1 of d. As can be seen in Fig. 2-14, tapering of the holes results in a reduced effective r as compared to the perfect structure. As a main consequence, λ_c shifts towards smaller wavelengths.

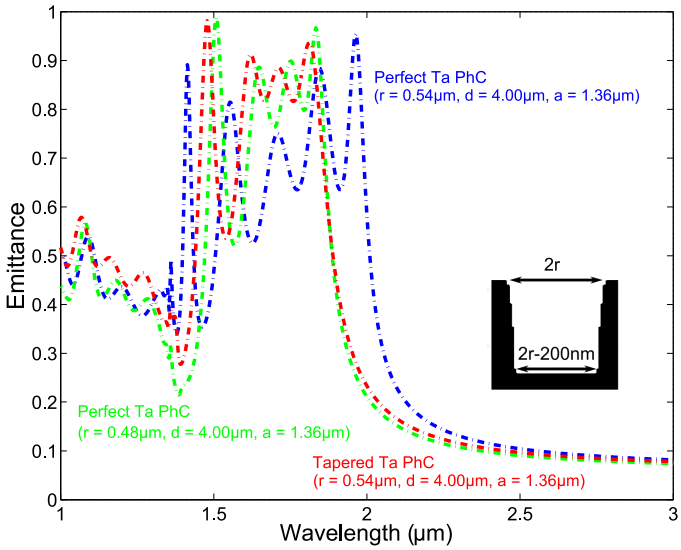

Figure 2-14: ε of the tapered structure (see inset) can be modeled by a perfect structure with a smaller effective r.

The contrast in ε is almost unaffected; for the perfect structure with the effective r, ε contrast of 5:1 is achieved over 10% wavelength separation, while for the tapered structure, the same contrast is achieved over 11% wavelength separation. Long wavelength ε is unaffected as expected.

2.5.2 Sidewall Roughness

Due to the stochastic nature of the chemical wet etch used to pattern the Cr hard mask, the sidewalls of the finished 2D MPhCs suffer from roughness. The best fabricated PhC, as shown in Fig. 2-8, has maximum sidewall deviation of $\approx 0.09a = 125\,\text{nm}$, and average sidewall deviation $\approx 0.045a = 65\,\text{nm}$.

The effects of sidewall roughness can easily be studied using FDTD simulations by incorporating both inclusion and removal of the corresponding metallic material at random points along the perimeter of each air hole, designed such that the average change in air hole area is zero. The maximum size and average size of the deviation is denoted by δ and $\delta/2$ respectively. Even though the simulation is designed such that the average change in air hole area is zero, λ_c increases as shown in Fig. 2-15. This suggests an increase in the effective r of the structure, which is expected due to increased penetration of the electromagnetic fields into the air regions. This is confirmed in

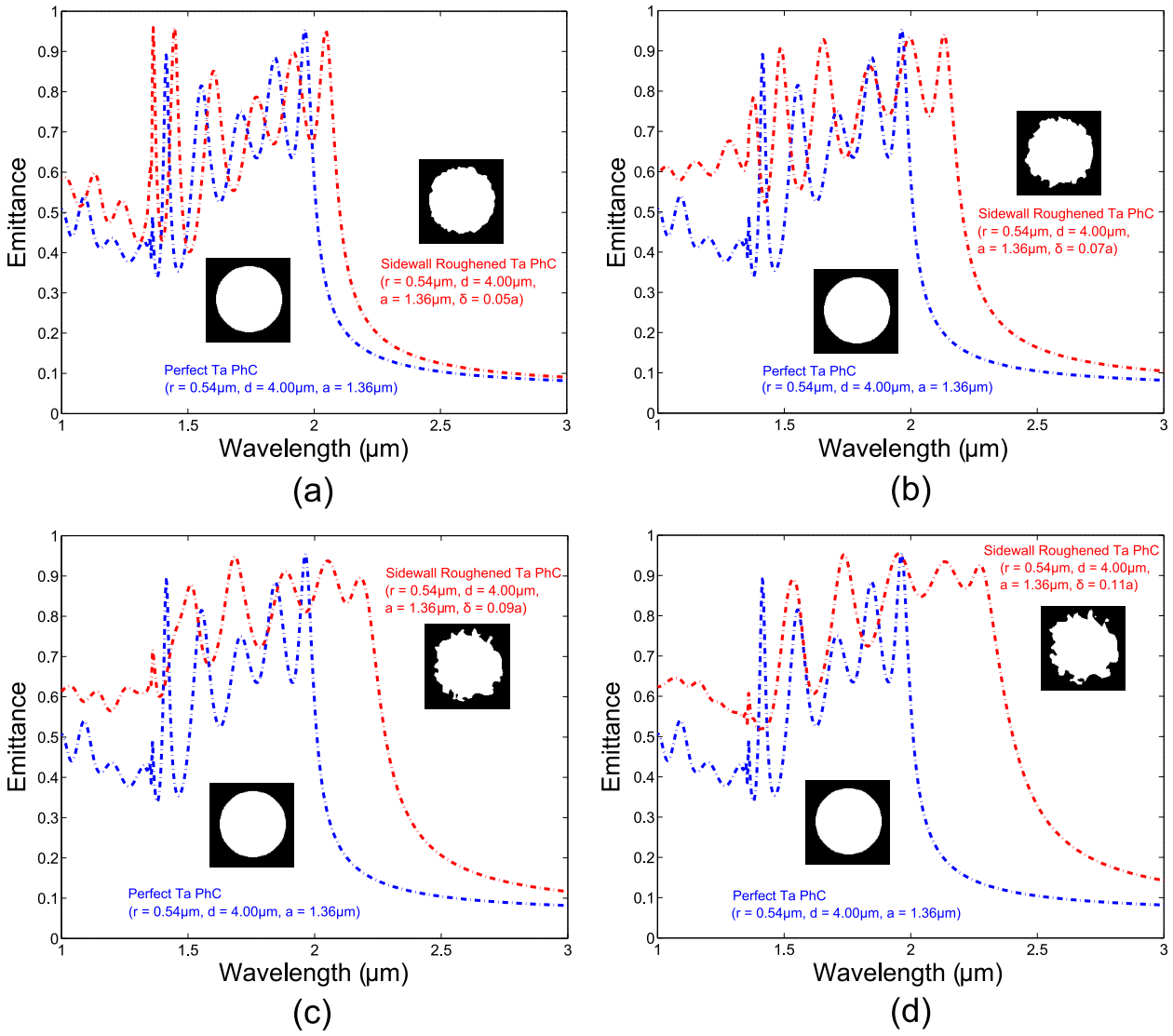

Figure 2-15: Effect of sidewall roughness (quantified as maximum sidewall deviation δ) on the performance of the emitter. (a) $\delta = 0.05a$ (b) $\delta = 0.07a$ (c) $\delta = 0.09a$ (d) $\delta = 0.11a$

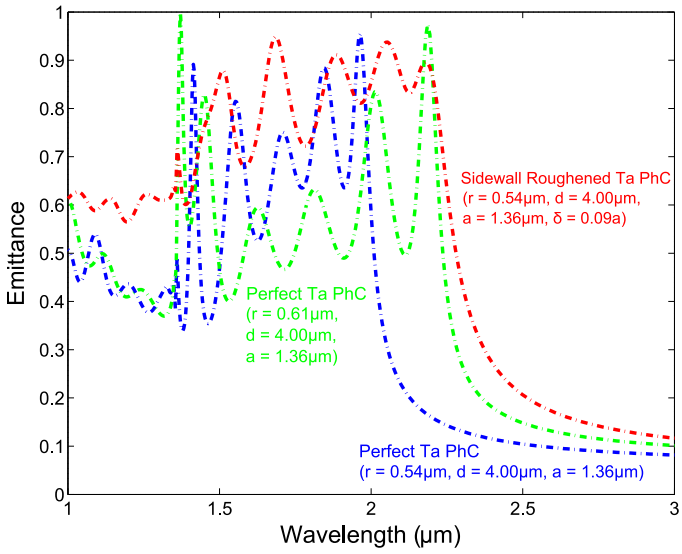

Figure 2-16: λ_c of the sidewall roughened structure can be approximated by a perfect structure with a larger effective r. However, average ε below λ_c is higher by $\approx 30\%$ for sidewall roughened structures.

Fig. 2-16, where comparison of ε between a perfect structure with a larger effective r and a sidewall roughened structure with $\delta = 0.09a$ shows resonance wavelengths that are approximately aligned. However, the increased metallic surface area of the sidewall roughened structure allows enhanced interaction with electromagnetic fields at $\lambda < \lambda_c$, resulting in an increase of the average ε by $\approx 30\%$. This is in fact a desirable effect for applications requiring maximum ε at $\lambda < \lambda_c$. The only drawback is the slightly reduced Q-factor of the resonances, resulting in reduced ε contrast at the cutoff; the sidewall roughened structure has an ε contrast of 5:1 over 16% wavelength separation while the effective r perfect structure achieved the same contrast over 8% wavelength separation. Nevertheless, they have approximately the same long wavelength ε (within 0.005 at around $\lambda = 4\,\mu\text{m}$).

Hole Radius Variation

Simulations of sidewall roughened structures with larger supercells can provide us with insight into the effect of random variation between the holes in fabricated structures. The results are shown in Fig. 2-17 for 1×1, 2×2, 3×3, and 4×4 supercells. Results from the 1×1 cell do indeed

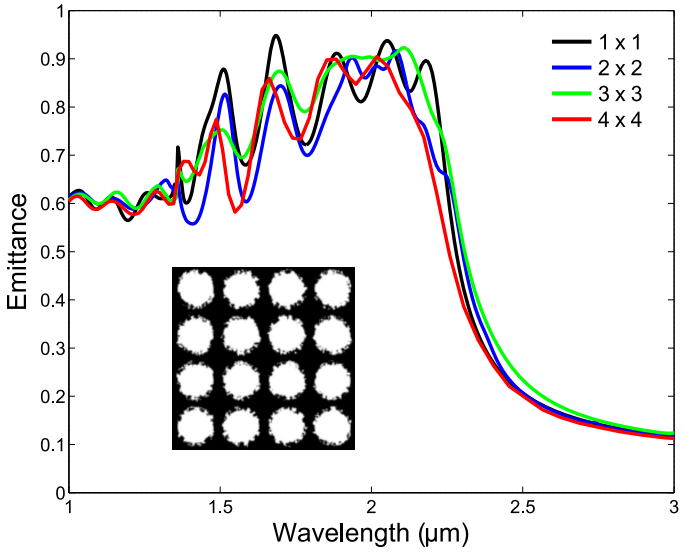

Figure 2-17: Simulations with larger supercells allows us to approach the fabricated structure. Results from the 1×1 cell nevertheless provide a good approximation to results obtained using larger supercells, especially for the higher order modes. The first few modes however may merge due to broadening caused by variation in the effective r between holes. Results shown are for 2D Ta PhC with $r = 0.54\,\mu\text{m}$, $d = 4.00\,\mu\text{m}$, $a = 1.36\,\mu\text{m}$, $\delta = 0.09a$. (Inset: 4×4 supercell)

provide a good approximation, especially for the higher order modes. However, due to the variation in the effective r between the holes, the first few modes may merge as a result of superposition of the individual resonances at slightly different frequencies. For the dimensions considered (2D Ta PhC with $r = 0.54\,\mu\text{m}$, $d = 4.00\,\mu\text{m}$, $a = 1.36\,\mu\text{m}$), a 25 nm variation in r results in approximately 100 nm shift in the resonance wavelength. Hence, ε of fabricated structures is expected to exhibit broadening.

Breakage of Sidewalls

When sidewall deformation gets too large ($\delta > 0.15a$ when $r = 0.4a$), the sidewalls may break during the etching process, causing the cylindrical cavities to become connected to each other. New resonant modes not pertaining to metallic cylindrical cavities start to appear, and electromagnetic waves of larger wavelengths are now able to enter the cavities due to the increased λ_c. Consequently, the emitter loses its wavelength selectivity as long wavelength ε elevates. Results for $\delta = 0.18a$ when $r \approx 0.4a$ are shown in Fig. 2-18. Therefore, during fabrication, it is recommended to start

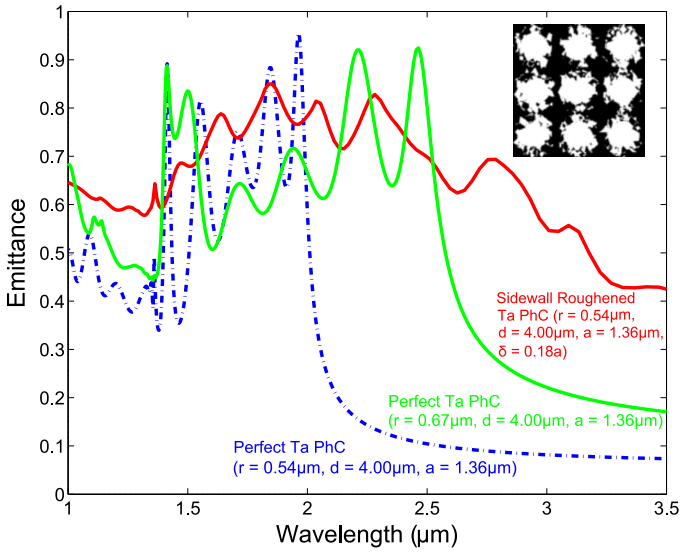

Figure 2-18: As the sidewalls become broken, the cylindrical cavities may become connected to each other, thus allowing interaction with electromagnetic waves of larger wavelengths. Consequently, long wavelength ε increases by more than 100% compared to the perfect structure with very thin sidewalls (in green).

with a slightly larger a than necessary to ensure that the sidewalls remain intact.

2.5.3 Contamination

Initial fabrication efforts resulted in 2D W PhC samples that have unusually high long wavelength ε as shown in Fig. 2-19. Closer investigation of the surface using X-ray Photoelectron Spectroscopy (Kratos AXIS Ultra Imaging) showed significant ($>$ 9 atoms per W atom) presence of Cr, fluorine (F), and carbon (C). The presence of C and F is most likely due to the final CF_4 based RIE performed to etch cylindrical cavities into W, while presence of Cr signifies its incomplete removal using the Cr-7 wet etchant in the final fabrication procedure.

In order to confirm the hypothesis that the contamination caused the sample to be more absorptive at $\lambda > \lambda_c$, a few experiments were performed to compare ε of a new W sample to samples that have been subjected to various fabrication processes. We start with Dirty W I, which is a clean W sample with 20 nm of Cr deposited on top of it. As shown in Fig. 2-20, Cr is approximately 3 times more absorptive than W at long wavelengths, hence the presence of Cr on the surface is

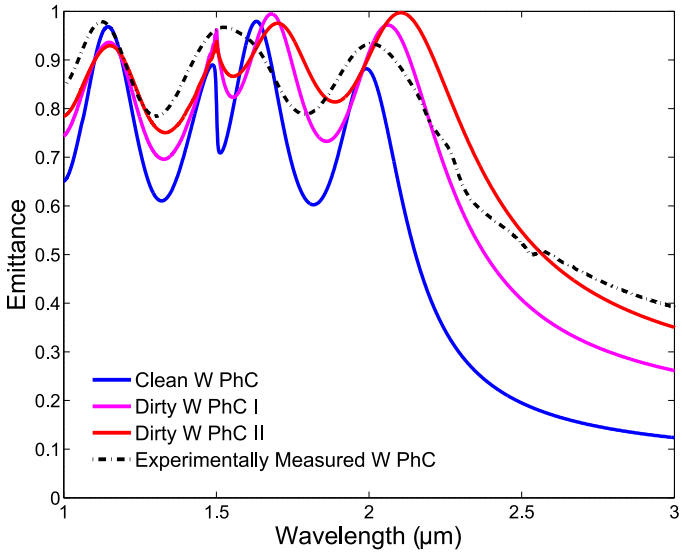

Figure 2-19: ε of 2D W PhC ($r = 0.58\,\mu\text{m}$, $d = 1.60\,\mu\text{m}$, $a = 1.50\,\mu\text{m}$) at various contamination levels. Solid lines are results obtained from numerical simulations while the dotted line is a measurement taken from a representative fabricated sample. Dirty 2D W PhC I and Dirty 2D W PhC II are simulations assuming a surface that is respectively 5% and 10% more absorptive than clean W.

detrimental to the emitter's wavelength selectivity. Next, Dirty W I was subjected to 10×5 minutes CF_4 based RIE and subsequent immersion into the Cr-7 liquid etchant for 3 minutes, resulting in a sample (Dirty W IV) that is more emissive by ≈ 0.06 compared to the new sample (New W). For the sample not exposed to the CF_4 based RIE (Dirty W II), ε is only higher by ≈ 0.01. This signifies that upon exposure to RIE, the Cr hard mask becomes harder to remove. Additionally, exposure to RIE without a mask can also elevate ε (Dirty W III).

In conclusion, contamination on the top surface of metal PhCs can result in elevated ε in the region $\lambda > \lambda_c$, therefore destroying the selectivity of the emitter. In contrast, contamination in the cylindrical cavities only affect ε below λ_c; the PhCs exhibit resonances that are broader and have lower Q-factors. Interestingly, the average ε below λ_c increases by $\approx 15\%$, bringing it closer to the ideal emitter performance. However, low ε at $\lambda > \lambda_c$ is more critical. Thus, to avoid issues with contamination, it is highly recommended that a thicker Cr mask than necessary is deposited to adequately protect the top surface from the final CF_4 based RIE. This also ensures that an adequately thick layer of high purity Cr remains at the bottom, which ensures an easier removal

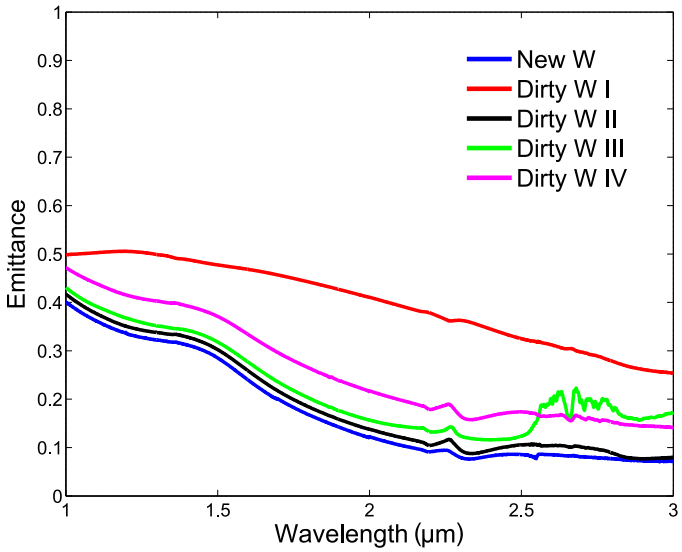

Figure 2-20: Measured ε of W samples subjected to various fabrication processes; Dirty W I has 50 nm Cr deposited on the top surface of a clean sample, Dirty W II is Dirty W I subjected to immersion in Cr-7 liquid etchant for 3 minutes, Dirty W III is a clean sample subjected to 10×5 minutes of the same CF_4 based RIE used in etching holes into W, and Dirty W IV is Dirty W I subjected to 10×5 minutes of the same CF_4 based RIE and subsequent immersion into Cr-7 liquid etchant for 3 minutes.

with the Cr-7 liquid etchant in the final step.

2.6 Conclusions

In this chapter, we have demonstrated highly selective thermal emission using 2D MPhCs that consist of a square array of cylindrical cavities etched into an optically smooth metallic substrate. The 2D MPhC exhibits low emittance at long wavelengths and near-blackbody emittance at short wavelengths, with a sharp cutoff in between, as predicted by numerical modeling and optimization. The enhancement of emission is provided by coupling of free space radiation into cavity modes.

Thermal emission of the 2D MPhC design can easily be optimized for a particular application via Q-matching, whereby the absorptive and radiative rates of the PhC's cavity resonances are matched, resulting in near-ultimate short wavelength emittance. In addition, the bandgap edge of the PhC can be tailored to theoretically any wavelength of interest by virtue of controlling the cavity's resonant frequency (limited only by intrinsic material properties and fabrication limits).

Furthermore, the approach is directly applicable to any highly reflective metallic material, for instance platinum, silver, molybdenum, tantalum, etc. since the magnitude of the first emittance peak is controlled solely by Q-matching.

Using this, 2D W PhC designs capable of an emission contrast of about 3:1 over 10% wavelength separation have been demonstrated numerically and experimentally, a marked improvement to previously reported work with an approximate emission contrast of 2:1 [12, 25–29]. Furthermore, with theoretical guidance via Q-matching, designs with maximum emission at larger wavelengths previously unattainable have been achieved. As an example, we have shown theory and computationally guided designs optimized for use in TPV systems employing cells with different electronic bandgaps. They are also robust with respect to experimental levels of disorder and impurities. Strong angular selectivity has also been observed, with short wavelength emission suppressed by 50% at the polar angle of 75° compared to normal incidence.

We have also demonstrated high operation temperatures of at least 1200 K with our 2D W PhC selective thermal emitters that have been produced over large areas with macroscopic long range order using conventional nanofabrication techniques already demonstrated at scale. The spectral properties of MPhCs, including the cutoff wavelength and magnitude of the high emittance region, have remained stable at high temperatures, demonstrating the mechanical and optical robustness of our design with respect to temperature.

The 2D MPhCs provide the platform necessary to realise high temperature nanophotonics for energy applications, ranging from efficient solar absorbers for solar thermal applications [15–17, 19], which are characterized by good solar absorption (low reflectance for wavelengths smaller than a cutoff wavelength usually in the vicinity of 1.5 µm to 2.5 µm depending on operating temperature and solar concentration) and low thermal emittance (high reflectance for wavelengths larger than the cutoff wavelength, and angularly selective absorption), to highly efficient selective emitters that are important for realizing both high efficiency and high power density TPV energy conversion systems [13, 14, 18]. In addition, they can be applied as a high efficiency near- to mid-IR radiation source for IR spectroscopy, night vision, as well as miniaturized on-chip for sensing applications including highly selective gas and chemical sensing [20, 21].

Chapter 3

Performance Analysis of Experimentally Viable Photonic Crystal Enhanced Thermophotovoltaic Systems

Following experimental demonstration of the 2D MPhCs described in Chapter 2, it is instructive to evaluate its performance in targeted high temperature applications. In this chapter, we quantify the performance improvement seen when implementing optimized 2D MPhCs as selective emitters in TPV energy conversion systems, whereby efficient spectral control is imperative in achieving high efficiency. In addition, the performance of the 2D MPhC selective emitter is compared to the greybody emitter coupled with the well characterized cold-side tandem filter. Finally, we evaluate the parasitic losses in experimentally realistic TPV systems using state-of-the-art components that are available today in order to identify areas for improvement.

3.1 Introduction

Recent advancements in the field of low bandgap PV cells [40,41,43,44] has led to renewed interest in developing high efficiency and high power density TPV energy conversion systems, whereby direct conversion of thermal radiation to electricity is achieved via the PV effect [55–57]. Compared to solar PV conversion, the heat source is significantly closer to the PV cell, resulting in photon flux and power density that are orders of magnitude higher. However, due to the much lower temperatures achievable in practical TPV systems ($< 2000\,\mathrm{K}$), the majority of emitted photons lie in the near- to mid-IR spectrum, hence the importance of high quality low bandgap PV cells in developing high efficiency TPV systems. TPV systems offer many advantages, including the promise of highly versatile and compact high power density energy conversion systems that have no moving parts, leading to quiet and robust operation. Virtually any high grade heat source can be utilized, including waste heat [57], fossil fuels [13, 58], radioisotopes [14, 42, 59, 60], and solar energy [15, 16, 61–63].

Even though low bandgap PV cells allow more efficient use of the emitted radiation, the broadband nature of thermal emission at the relatively low temperatures considered results in significant emission of below bandgap photons. For instance, only 28% of the radiant exitance of a blackbody at 1500 K with peak radiation at a wavelength of 1.93 µm lies below 2 µm, which is approximately the bandgap of InGaAs PV cells [41]. The remaining non-convertible photons emitted result in parasitic heat losses, which would also lead to highly undesirable elevated PV cell operating temperatures. Hence, spectral control is critical in achieving higher TPV system efficiencies.

Spectral control can be achieved firstly via the use of selective emitters to preferentially emit convertible photons. To date, various selective emitters have been investigated; from rare-earth oxides [61, 64–66], to 1D [32, 67], 2D [23, 25, 27, 28, 45, 68], and 3D PhCs [12, 26, 29, 69]. Another spectral control approach relies on recuperating non-convertible photons using front surface reflectors [70–73] and back surface reflectors [74–76] on the PV cell. A TPV system including both aspects of spectral control is shown in Fig. 3-1(b).

Following recent efforts on the design, fabrication, characterization, and optimization of spectral

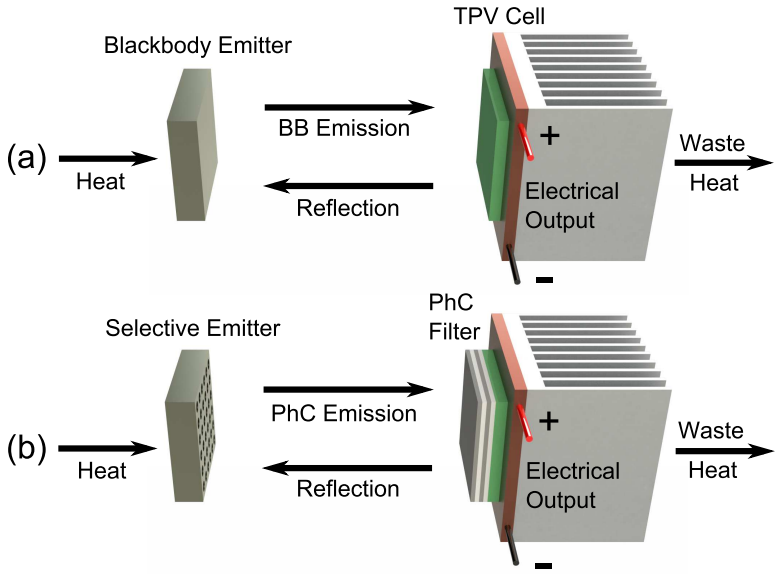

Figure 3-1: (a) Conventional TPV energy conversion system without spectral control. (b) TPV system with 2D PhC selective emitter and cold-side filter. Spectral control enables performance enhancement of up to 400% over the conventional TPV system.

control devices for TPV applications, many studies have attempted to estimate the enhancement in TPV system performance [13,18,77,78]. In this investigation, we focus on obtaining estimates of TPV system performance using spectral control components that have recently been demonstrated *experimentally*, while taking into account high temperature and angular dispersion properties to ensure realistic estimates. In particular, we focus on 2D tantalum (Ta) PhCs as the selective emitter; Ta is chosen for this investigation as it is machinable, which is not the case for W described in Chapter 2. Machinability is important to ensure ease of system integration. Regardless, just like 2D W PhCs, 2D Ta PhCs offer the same sharp emittance cutoff that is easily shifted and optimized [28,31,34], are scalable to large areas [79], and have been proven to be thermally stable at high temperatures in high vacuum conditions [80]. The performance of this emitter is evaluated with or without a cold-side tandem filter [70,73], which to date is widely regarded as one of the more promising experimentally realized reflective spectral control device [14,71,81].

In the following section, we will discuss the numerical model used to obtain detailed performance predictions of TPV systems. Inputs to the model include key physical properties of each component

that constitute the TPV system; optical properties are captured by the absorptance, reflectance, and transmittance of the emitter, cold-side filter, and PV cell; electrical power generating properties are captured by the quantum efficiency, dark current, parasitic resistances, and ideality factor of the PV cell. Methods to obtain optimized 2D Ta PhC selective emitter and cold-side tandem filter designs will also be discussed. In section 3.3, TPV modeling results of various emitter and cold-side filter combinations will be presented. In addition, we will analyze the performance of 3 different current state-of-the-art low bandgap TPV cells using key physical properties that have been experimentally measured from fabricated cells; GaSb (bandgap $E_{\mathrm{g}} \simeq 0.72$ eV) [40,82], InGaAs ($E_{\mathrm{g}} \simeq 0.62$ eV) [41,42], and InGaAsSb ($E_{\mathrm{g}} \simeq 0.55$ eV) [43,44,82]. The results using experimentally realizable components will be benchmarked against idealized components to identify areas that require improvement. We then conclude by summarizing our findings in section 3.4. Note that a condensed version of this chapter is reported in Ref. 83.

3.2 Numerical Model

3.2.1 Thermophotovoltaic System

To obtain the short circuit current I_{sc} generated, the net irradiance incident on the PV cell is calculated following a ray tracing approach. We begin with the definition of the spectral radiance of a blackbody:

$$i_{\mathrm{BB}}(\lambda, T) = \frac{2hc^2}{\lambda^5[\exp(\frac{hc}{\lambda kT}) - 1]} \tag{3.1}$$

The total radiant power emitted P_{em} at temperature T by an emitter of area A_1 with temperature and angular dependent spectral emittance $\varepsilon(\lambda, \theta_1, \phi_1, T)$ is then given by:

$$P_{\mathrm{em}} = \int_0^{\infty} \mathrm{d}\lambda \int_0^{\frac{\pi}{2}} \mathrm{d}\theta_1 \int_0^{2\pi} \mathrm{d}\phi_1 \int_{A_1} \mathrm{d}A_1 \left[i_{\mathrm{BB}}(\lambda, T)\, \varepsilon(\lambda, \theta_1, \phi_1, T)\, \cos\theta_1 \sin\theta_1 \right] \tag{3.2}$$

where θ_1 is the polar angle and ϕ_1 is the azimuthal angle. The fraction of P_{em} reaching the PV cell can be evaluated by first considering the differential radiant power incident on the PV cell of

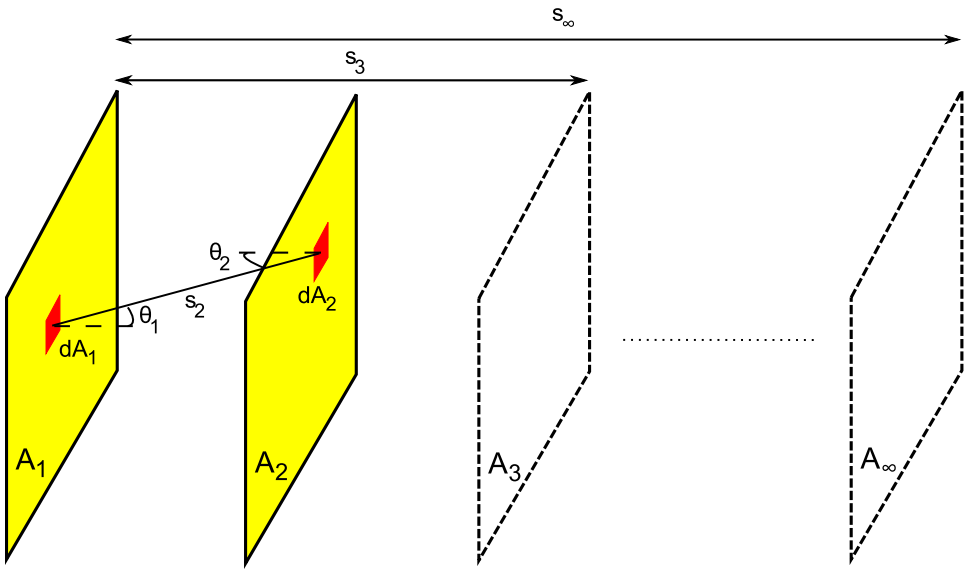

Figure 3-2: Radiative heat transfer model involving emitter of area A_1 and PV cell of area A_2. θ_1 and θ_2 are respectively the angle between the straight line connecting the two infinitesimal areas $\mathrm{d}A_1$ and $\mathrm{d}A_2$ and their respective normal vectors, and s_2 is the distance between $\mathrm{d}A_1$ and $\mathrm{d}A_2$. To take into account the multiple reflections taking place between the emitter and the PV cell, alternating virtual surfaces of the emitter and PV cell are constructed at a distance s_l from the initial emitter.

infinitesimal area $\mathrm{d}A_2$ from an emitter of infinitesimal area $\mathrm{d}A_1$:

$$\mathrm{d}Q_{\mathrm{dA_1}\rightarrow\mathrm{dA_2}} = i_{\mathrm{BB}}(\lambda, T)\,\varepsilon(\lambda, \theta_1, \phi_1, T)\,\mathrm{d}A_1\,\mathrm{d}F_2 \tag{3.3}$$

$\mathrm{d}F_2$ is the differential view factor, which is defined as the fraction of radiant power emitted by $\mathrm{d}A_1$ incident on $\mathrm{d}A_2$:

$$\mathrm{d}F_2 = \frac{\cos\theta_1\,\cos\theta_2}{s_2^2}\,\mathrm{d}A_2 \tag{3.4}$$

where θ_2 is the angle between the straight line connecting the two infinitesimal areas and the normal vector for $\mathrm{d}A_2$, and s_2 is the distance between $\mathrm{d}A_1$ and $\mathrm{d}A_2$ as illustrated in Fig. 3-2.

In a TPV system, it is important to take into account the multiple reflections taking place between the emitter and the PV cell. It is thus convenient to define the differential view factor $\mathrm{d}F_l$ for $\mathrm{d}A_l$, a differential virtual surface area constructed at a distance s_l from the initial emitter $\mathrm{d}A_1$

(see Fig. 3-2) to properly take into account the lth order reflection [84]:

$$\mathrm{d}F_l = \frac{\cos\theta_1 \, \cos\theta_l}{s_l^2} \, \mathrm{d}A_l \tag{3.5}$$

Even values of l represent reflections to the PV cell, while odd values represent reflections back to the emitter. Thus, the radiant power reabsorbed P_{re} by the emitter can be evaluated by integrating Eq. (3.3) and summing over odd values of l:

$$P_{\mathrm{re}} = \sum_{p=1}^{\infty} \int \mathrm{d}\lambda \int \mathrm{d}F_{2p+1} \int \mathrm{d}A_1 \left[i_{\mathrm{BB}}(\lambda, T) \, R_2^p \, R_1^{p-1} \, (1 - R_1) \, \varepsilon(\lambda, \theta_{2p+1}, \phi_{2p+1}, T) \right] \tag{3.6}$$

where R_1 and R_2 are the angular dependent reflectance of the emitter and the PV cell respectively. The terms $R_2^p \, R_1^{p-1}$ and $1 - R_1$ respectively captures the multiple reflections and final absorption events. For a parallel plate TPV system configuration considered in this investigation, Eq. (3.6) can be further simplified to the following:

$$P_{\mathrm{re}} = \sum_{p=1}^{\infty} \int \mathrm{d}\lambda \int \mathrm{d}A_{2p+1} \int \mathrm{d}A_1 \left[\frac{i_{\mathrm{BB}}(\lambda, T) \, R_2^p \, R_1^{p-1} \, (1 - R_1) \, \varepsilon(\lambda, \theta_{2p+1}, \phi_{2p+1}, T) \, \cos^2\theta_{2p+1}}{s_{2p+1}^2} \right] \tag{3.7}$$

Similarly, the convertible radiant power incident on the PV cell P_{cell}, and I_{sc} can be obtained by summing over even values of l:

$$P_{\mathrm{cell}} = \sum_{p=1}^{\infty} \int_0^{\lambda_{\mathrm{g}}} \mathrm{d}\lambda \int \mathrm{d}A_{2p} \int \mathrm{d}A_1 \left[\frac{i_{\mathrm{BB}}(\lambda, T) \, (R_1 R_2)^{p-1} \, (1 - R_2) \, \varepsilon(\lambda, \theta_{2p}, \phi_{2p}, T) \, \cos^2\theta_{2p}}{s_{2p}^2} \right] \tag{3.8}$$

$$I_{\mathrm{sc}} = 2qc \sum_{p=1}^{\infty} \int \frac{\mathrm{IQE}(\lambda) \, \mathrm{d}\lambda}{\lambda^4 [\exp(\frac{hc}{\lambda kT}) - 1]} \int \mathrm{d}A_{2p} \int \mathrm{d}A_1 \left[\frac{(R_1 R_2)^{p-1} \, (1 - R_2) \, \varepsilon(\lambda, \theta_{2p}, \phi_{2p}, T) \, \cos^2\theta_{2p}}{s_{2p}^2} \right] \tag{3.9}$$

where $\mathrm{IQE}(\lambda)$ and λ_{g} are respectively the internal quantum efficiency and bandgap of the PV cell, and q is the elementary electronic charge. Eq. (3.9) is then used to evaluate the total output current

I as a function of applied voltage V at the output terminals of the PV cell according to:

$$I = I_{\mathrm{sc}} - I_{\mathrm{o}} \exp\left[\frac{q(V + IR_{\mathrm{s}})}{mkT_{\mathrm{c}}}\right] - \frac{V + IR_{\mathrm{s}}}{R_{\mathrm{sh}}} \tag{3.10}$$

where m, I_{o}, R_{s}, R_{sh}, and T_{c} are respectively the ideality factor, dark current, series resistance, shunt resistance, and temperature of the PV cell [85]. The output electrical maximum power point $P_{\mathrm{elec,\ max}}$ is then obtained by maximizing $P_{\mathrm{elec}} = IV$ by setting $\mathrm{d}(IV)/\mathrm{d}V = 0$. The radiant heat-to-electricity TPV efficiency η_{TPV} is then given as follows:

$$\eta_{\mathrm{TPV}} = \frac{P_{\mathrm{elec,\ max}}}{P_{\mathrm{em}} - P_{\mathrm{re}}} \tag{3.11}$$

η_{TPV} can further be broken down into the overall spectral efficiency when TPV cavity effects are taken into account $\eta_{\mathrm{cav\text{-}spec}}$, and the PV cell efficiency η_{cell}:

$$\eta_{\mathrm{cav\text{-}spec}} = \frac{P_{\mathrm{cell}}}{P_{\mathrm{em}} - P_{\mathrm{re}}} \tag{3.12}$$

$$\eta_{\mathrm{cell}} = \frac{P_{\mathrm{elec,\ max}}}{P_{\mathrm{cell}}} \tag{3.13}$$

Note that the evaluation of Eqs. (3.7)–(3.9) can be computationally intensive, especially in obtaining estimates for optimization purposes. Thus, it is interesting to consider the simplification of capturing the angular dependence via the spectral hemispherical emittance $\varepsilon_{\mathrm{H}}(\lambda, T)$:

$$\varepsilon_{\mathrm{H}}(\lambda, T) = \frac{1}{\pi} \int_0^{\frac{\pi}{2}} \mathrm{d}\theta_1 \int_0^{2\pi} \mathrm{d}\phi_1 \left[\varepsilon(\lambda, \theta_1, \phi_1, T) \cos\theta_1 \sin\theta_1\right] \tag{3.14}$$

Using this, the problem simplifies into radiation exchange between two general surfaces of total area A_1 and A_2, thereby not requiring the intensive numerical integration over all differential areas. Indeed, we have verified that both the full ray tracing method and the spectral hemispherical approximation produce results that agree very well (see Appendix 3.A). This is expected given the very high view factors ($F > 0.85$) involved in practical parallel plate TPV systems that are considered in this investigation, whereby most emission up to $\theta \lesssim 85^\circ$ is incident on the PV cell.

3.2.2 Two-dimensional Tantalum Photonic Crystals as Selective Emitters

The 2D MPhC described in Chapter 2 is well suited for enabling high efficiency TPV systems, as it can be easily designed to simultaneously achieve near-blackbody ε at $\lambda < \lambda_g$, as well as ε almost as low as a polished metal at long wavelengths, with a sharp cutoff separating the two regimes. Of the various refractory metals available, Ta is selected for this investigation as it is highly machinable and weldable. This is extremely vital in ensuring practical integration into a TPV system. In addition, the 2D Ta PhC emitter has been demonstrated to be thermally stable at high temperatures in high vacuum environments [80], and the fabrication process is scalable to large areas [79], both of which are essential for practical large scale adoption.

As discussed in Section 2.2, Q-matching of the fundamental cavity resonance mode allows quick identification of near optimal designs for TPV systems. However, it is not the global optimum as it is difficult to simultaneously achieve Q-matching for higher order modes, which is important in broadening the bandwidth for maximum ε at $\lambda < \lambda_g$ and thereby maximum η_{TPV} and $P_{elec,\,max}$. In addition, the optimization problem is highly non-convex marked by a large number of local optima. Hence, non-linear global optimization methods were used to uncover the optimum r, d, and a of the 2D Ta PhC that would best suit a particular TPV cell as local search algorithms may potentially get trapped in a localized peak [18]. The global optimum was found via the multi-level single-linkage (MLSL) method, which executes a quasi-random low-discrepancy sequence (LDS) of local searches [86] using constrained optimization by linear approximation (COBYLA) [87]. Other global search algorithms, such as the controlled random search (CRS) algorithm [88], also yielded similar results. The global optimization routines were implemented via NLOpt, a free software packaged developed at MIT that allows comparison between various global optimization algorithms [89]. Note that in all optimization routines, the design provided by Q-matching of the fundamental mode was used as the initial estimate. In addition, the following constraints were implemented: $a - 2r \geq 100\,\text{nm}$ to ensure integrity of sidewalls; $d \leq 8.50\,\mu\text{m}$ based on fabrication limits using an SF_6 based DRIE Bosch process [79].

$\varepsilon(\lambda, \theta_1, \phi_1, T)$ of the 2D Ta PhC can easily be determined via FDTD numerical methods [35]

coupled with the Lorentz–Drude model fitted to elevated temperature emittance [80] to capture the optical dispersion of Ta. However, high memory requirements and slow computational speed of FDTD methods limit its application in determining the globally optimum design for a particular TPV system. Thus, to obtain quicker estimates, we utilized the mode matching formalism described in Ref. 90, of which we have confirmed to match very well with FDTD methods. In essence, the reflectance was calculated by matching the radiation fields at the boundary of free space and the cylindrical cavities via expansion of the cavity modes for shorter wavelengths, and utilizing a surface area weighted impedance for longer wavelengths.

The calculated $\varepsilon(\lambda, \theta_1, \phi_1, T)$ can then be used to obtain η_{TPV} and the maximum power density $J_{\text{elec, max}} = P_{\text{elec, max}}/A_1$ as described in Section 3.2.1. For optimization purposes, we used the following figure of merit:

$$\text{FOM} = x\eta_{\text{TPV}} + (1-x)\frac{J^{\text{PhC}}_{\text{elec, max}}}{J^{\text{BB}}_{\text{elec, max}}} \tag{3.15}$$

where $J^{\text{PhC}}_{\text{elec, max}}/J^{\text{BB}}_{\text{elec, max}}$ captures the TPV system power density performance of the 2D Ta PhC emitter compared to a blackbody, and $x \in$ [0,1] is the weighting given to η_{TPV} in the optimization routine, which could be modified depending on design goals. In this investigation, we are mainly concerned in obtaining the highest η_{TPV} possible, thus $x = 0.9$ was used. Using this, 3 different designs optimized for GaSb [40, 82], InGaAs [41, 42], and InGaAsSb [43, 44, 82] cells were obtained. As can be seen in Fig. 3-3, the normal incidence spectral emittance $\varepsilon_\perp$ of the optimized 2D Ta PhCs is high at $\lambda < \lambda_{\text{g}}$ of the respective TPV cells, and low at $\lambda > \lambda_{\text{g}}$. Note that in the optimization routine, we have assumed an approximate operating $T = 1500\,\text{K}$ and a fixed view factor $F = 0.99$, which is realistically achievable using a $100\,\text{mm} \times 100\,\text{mm}$ flat plate geometry with separation $s = 500\,\mu\text{m}$. Regardless, the exact operating T and F of the final optimal TPV system are relatively unimportant as long as they are reasonably close. This is due to the fact that the optimization routine indirectly searches for the design with the best selective $\varepsilon_\perp$. In fact, the optimum design also has the best selective ε_{H}, firstly due to the fact that the cavity resonance wavelength remains the same regardless of θ_1 and ϕ_1. Secondly, the best selective $\varepsilon_\perp$ and ε_{H} can only be achieved by limiting diffraction as discussed in Section 2.2.1, thus leading the algorithms to converge to the smallest possible a.

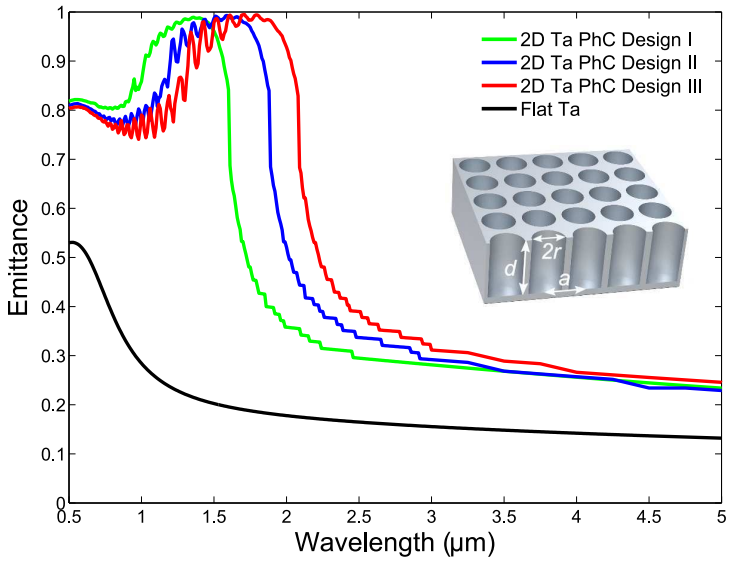

Figure 3-3: Simulated high temperature ($T = 1478\,\mathrm{K}$) normal spectral emittance $\varepsilon_\perp$ of flat Ta and 2D Ta PhCs optimized for GaSb (Design I: $r = 0.43\,\mu\mathrm{m}$, $d = 8.50\,\mu\mathrm{m}$, $a = 0.95\,\mu\mathrm{m}$), InGaAs (Design II: $r = 0.51\,\mu\mathrm{m}$, $d = 8.50\,\mu\mathrm{m}$, $a = 1.11\,\mu\mathrm{m}$), and InGaAsSb (Design III: $r = 0.57\,\mu\mathrm{m}$, $d = 8.50\,\mu\mathrm{m}$, $a = 1.23\,\mu\mathrm{m}$). As can be seen, λ_c is easily shifted by modifying the dimensions of the PhC.

3.2.3 Plasma-dielectric Stacks as Cold-side Bandpass Filters

Recent TPV system experiments demonstrating record η_TPV of 19% employed a greybody-like graphite emitter with a cold-side tandem filter [14]. It is thus instructive to compare the TPV system performance using 2D Ta PhCs as the emitter, with or without the tandem filter. The tandem filter consists of bi-material multilayer dielectric stack terminated with a plasma filter [70, 73]. The dielectric stack is essentially an enhanced version of the quarter-wave stack, whereby high transmission is seen for photons within the convertible range yet simultaneously providing high reflection in the mid-infrared range ($\lambda \sim 2$–$6\ \mu\mathrm{m}$). In order to extend the bandwidth of high reflection beyond $\lambda = 6\,\mu\mathrm{m}$, an additional plasma filter consisting of a highly doped semiconductor is deposited at the end of the multilayer dielectric stack. λ_c of the tandem filter can be shifted by modifying the thicknesses of the dielectric stack layers, and further optimized for particular TPV cells using the optimization technique described in Ref. 70. The measured normal incidence transmittance of two particular designs optimized for 0.5 eV and 0.6 eV cutoffs are shown in Fig. 3-

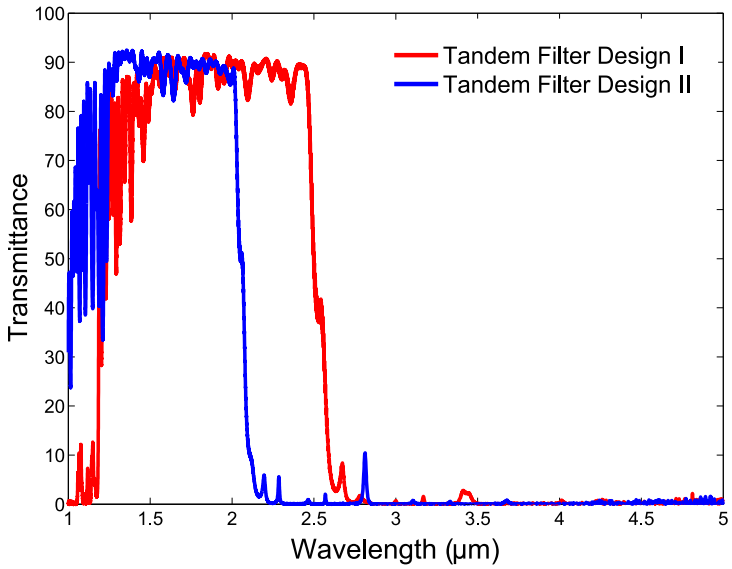

Figure 3-4: Measured normal incidence transmittance of tandem filters optimized for 0.5 eV and 0.6 eV TPV cells. The tandem filters consist of dielectric stacks of antimony selenide (Sb_2Se_3) and yttrium fluoride (YF_3), terminated with a 1 µm thick heavily doped indium phosphide arsenide (InPAs) layer as the plasma filter. The tandem filters were obtained from Rugate Technologies, Inc.

4. The filters were fabricated by Rugate Technologies, Inc. using antimony selenide (Sb_2Se_3) and yttrium fluoride (YF_3) as the multilayer dielectric stack, and a heavily doped indium phosphide arsenide (InPAs) layer as the plasma filter.

3.3 Results and Discussion

We now consider TPV systems utilizing both the optimized 2D Ta PhC selective emitter and the cold-side tandem filter discussed in Section 3.2.2 and Section 3.2.3 respectively. In order to benchmark the performance of the 2D Ta PhC selective emitter, a greybody emitter ($\varepsilon = 0.9$) and an idealized cutoff emitter ($\varepsilon_H = 0.9$ for $\lambda < \lambda_c$ and $\varepsilon_H = 0.1$ for $\lambda > \lambda_c$) are included in the analysis. The idealized cutoff emitter is used as the approximate upper limit achievable with metallic PhCs.

In the following subsections, we will explore the effect of T and F on TPV systems utilizing the aforementioned spectral control devices. Following that, we will look into the effect of below bandgap emission of selective emitters on η_{TPV} in order to gain insight into the improvements

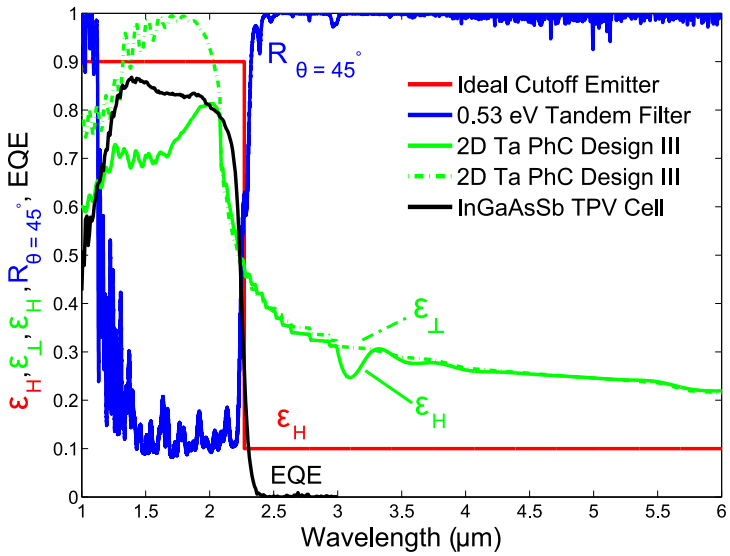

Figure 3-5: Relevant optical properties for optimized components in an InGaAsSb TPV system. The normal incidence emittance $\varepsilon_{\perp}$ and hemispherical emittance ε_{H} of the optimized 2D Ta PhC emitter, and $\theta = 45°$ reflectance $R_{\theta=45°}$ of the 0.53 eV tandem filter are shown to match the external quantum efficiency (EQE) of an InGaAsSb cell. An ideal cutoff emitter is included in the analysis to elucidate the effect of non-ideal spectral emittance of the optimized 2D Ta PhC.

necessary for selective emitters to be viable. Since the trends are general for all TPV cells in consideration, we will only present results for the particular InGaAsSb TPV cell described in Ref. 82. Finally, we will elucidate the effects of TPV cell non-idealities, and present estimates of optimized TPV system efficiencies using GaSb [40, 82], InGaAs [41, 42], and InGaAsSb [43, 44, 82] TPV cells, as well as compare the results to notable TPV experimental results reported to date.

3.3.1 Optimized InGaAsSb Thermophotovoltaic System

Figure 3-5 presents the measured external quantum efficiency (EQE) of the fabricated InGaAsSb cells [82], together with $\varepsilon_{\perp}$ and ε_{H} of the optimized 2D Ta PhC. As can be seen, λ_{c} of the optimized 2D Ta PhC matches well with the EQE of the InGaAsSb TPV cell. Although the performance is excellent at normal incidence, ε_{H} is significantly lower in the region of high EQE, which would negatively impact both η_{TPV} and $J_{\mathrm{elec,\,max}}$ since typical TPV systems are operated at high F. As discussed in Section 2.2.1 the intrinsic angular selectivity of the 2D Ta PhC arises from the constancy of the resonant peaks and the decreasing diffraction threshold as a function of incident polar angle.

At wavelengths below the diffraction threshold, absorptance decreases because there are more channels to reflect back to and Q_{rad} decreases, thus destroying Q-matching. Therefore, at larger incident angles, the in-band absorption region decreases and has a lower average absorptance (see Fig. 3-5). Nevertheless, ε_{H} still approaches the long wavelength limit determined by the volume fraction of air to Ta, thus maintaining some degree of spectral selectivity.

The tandem filter also suffers from angular dispersion detrimental to TPV systems. However, variations in the magnitude of transmittance at $\lambda < \lambda_{\mathrm{c}}$ and reflectance at $\lambda > \lambda_{\mathrm{c}}$ are less severe compared to the optimized 2D Ta PhCs. As θ increases, λ_{c} shifts to smaller λ's; selectivity only starts degrading above $\theta = 60^{\circ}$ [70]. Hence, the spectral hemispherical reflectance of the tandem filter is closely approximated by $\theta = 45^{\circ}$ reflectance, $R_{\theta=45^{\circ}}$. Since spectral hemispherical reflectance measurements of optimized filters are not available, shifted versions of measured normal incidence transmittance of filters shown in Fig. 3-4 are used as an estimate for $R_{\theta=45^{\circ}}$ in order to obtain estimates of η_{TPV} for systems employing the tandem filter. This is reasonable due to the following: λ_{c} of the filter is easily shifted within the wavelength range of interest in TPV by altering the layers' thicknesses; $R_{\theta=45^{\circ}}$ closely approximates normal incidence reflectance; and the filter exhibits absorptance close to zero for λ = 1–9 µm [70]. The estimated $R_{\theta=45^{\circ}}$ for a 0.53 eV tandem filter optimized for InGaAsSb TPV cells is shown in Fig. 3-5. Note that the absorptance of the tandem filter extracted from Ref. 70 not shown in Figure 3-5 is also taken into account in the model.

For TPV systems without the optimized tandem filter, the reflectance of the bare InGaAsSb cell becomes critical. Hence, reflectance of the InGaAsSb cells is included whenever possible, i.e. extracted from data published in literature [82]. Nevertheless, due to the limited wavelength range where reflectance data is available, we assume zero reflectance at wavelengths where data is unavailable to ensure conservative η_{TPV} estimates. We also assume a constant reflectance for the TPV cells over all angles as published literature data for experimentally fabricated cells are limited to near normal incidence. Regardless, these approximations do not prevent us from exposing critical spectral control requirements necessary in engineering efficient TPV systems, which is the main objective of this investigation.

3.3.2 Effect of Temperature and View Factor

Using the numerical model presented in Section 3.2, η_{TPV} can be estimated for InGaAsSb TPV systems comprising the ideal cutoff selective emitter, optimized 2D Ta PhC selective emitter, or greybody emitter ($\varepsilon = 0.9$), with or without the optimized tandem filter. First, we consider a system with a fixed $F = 0.99$. As shown in Fig. 3-6(a), there exists an optimum operating T for each of the combinations considered; if T is too low, the emission peak is located at $\lambda > \lambda_{\text{g}}$ of the TPV cell as indicated by sub-optimal $\eta_{\text{cav-spec}}$ and η_{cell} shown in Figs. 3-6(b) & (c); if T is too high, the TPV cell's R_{s} losses dominate as indicated by the reduction in η_{cell} shown in Fig. 3-6(c).

At the optimum T, highest η_{TPV} can be achieved by including the optimized 0.53 eV tandem filter; coupling the filter with the greybody and the optimized 2D Ta PhC emitter results in a maximum radiant heat-to-electricity efficiency $\eta_{\text{TPV, max}}$ of 23.5% and 23.7% respectively, which is extremely close to the performance of the ideal cutoff emitter of $\eta_{\text{TPV, max}} = 24.3\%$. The optimum operating T's are 1260 K, 1230 K, and 1210 K for the optimized 2D Ta PhC, greybody, and ideal cutoff emitter respectively, when coupled with the tandem filter. The corresponding $J_{\text{elec, max}}$'s are 0.62 W cm^{-2}, 0.66 W cm^{-2}, and 0.59 W cm^{-2} respectively. These results indicate that in a high F system, the use of a selective emitter is not critical if an optimized tandem filter is present. This is mainly due to the tandem filter's steep cutoff and high reflectance at $\lambda > \lambda_{\text{c}}$. Nevertheless, if implementation of the filter is not possible, the optimized 2D Ta PhC emitter offers $> 70\%$ improvement in $\eta_{\text{TPV, max}}$ over the greybody emitter.

To further study the effect of F, we consider each of the combinations at their optimum T. As shown in Fig. 3-7 the greybody performs as well as the optimized 2D Ta PhC when coupled with the optimized tandem filter at $F > 0.97$ (100 mm $\times$ 100 mm flat plate geometry with $s <$ 1.7 mm). If $F < 0.97$, significant improvement is seen with the optimized 2D Ta PhC over the greybody as the efficiency of photon recycling using the tandem filter deteriorates. Note, however, that in practical systems, it is important to realize that F is limited by the reduction in active cell area due to front side metallization (busbars) requirements of TPV cells, and less than ideal packing ratios when TPV cells are stitched together to form larger modules. The limiting effect of

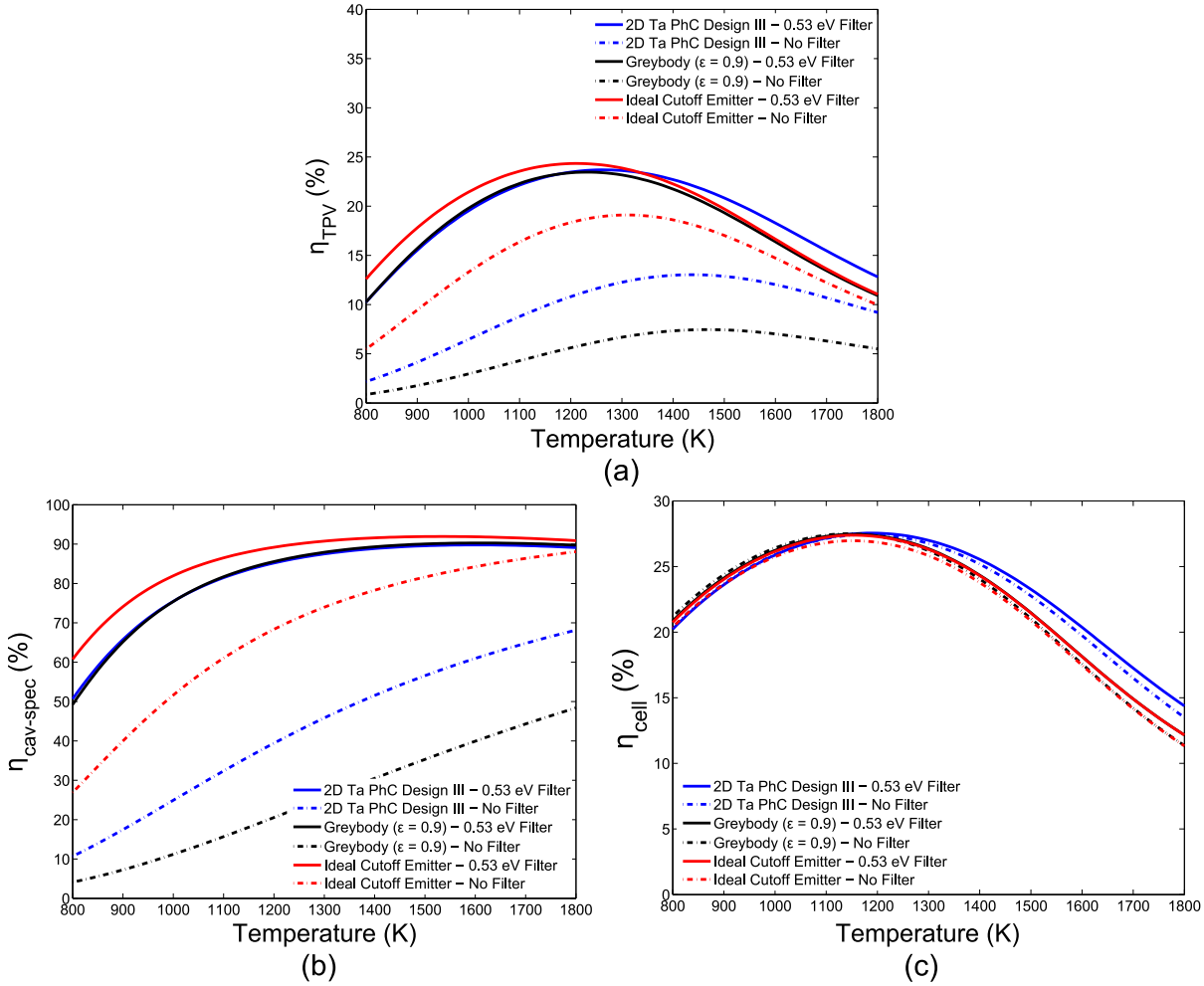

Figure 3-6: (a) Radiant heat-to-electricity efficiency η_{TPV} for various emitters with or without an optimized tandem filter in combination with an InGaAsSb TPV cell at fixed view factor $F = 0.99$ ($100\,\mathrm{mm} \times 100\,\mathrm{mm}$ flat plate geometry with separation $s = 500\,\mu\mathrm{m}$). An optimum T exist for each combination. Due to considerable emission below the bandgap of the InGaAsSb TPV cell for the emitters considered, significant improvement is seen with the use of the tandem filter. (b) Overall spectral efficiency when TPV cavity effects are included, $\eta_{\mathrm{cav\text{-}spec}}$. When $F = 0.99$, use of a selective emitter is not critical if an optimized tandem filter is present. (c) TPV cell efficiency, η_{cell}. For $T > 1200\,\mathrm{K}$, degradation of η_{cell} is observed due to larger series resistance R_{s} losses from high carrier injection.

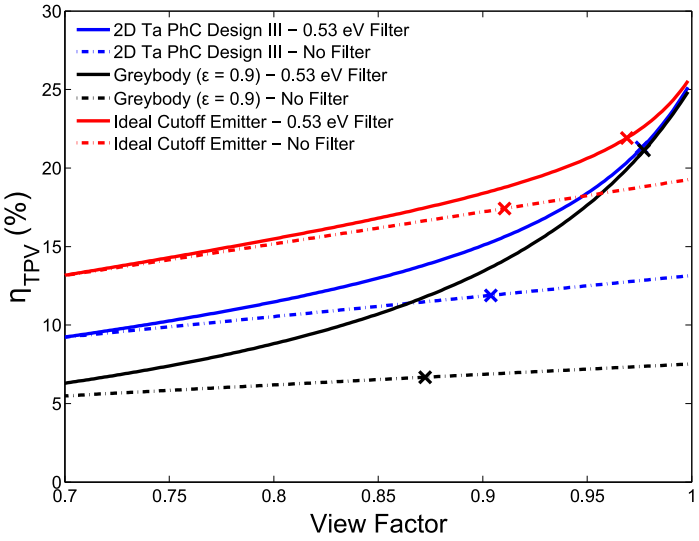

Figure 3-7: η_{TPV} at optimum T. The crosses are simulation results for $F = 0.99$ when the TPV cell active region is assumed to be 90% of total cell area.

this non-ideality can easily be determined in the model by assuming a certain active TPV cell area ratio, while non-active regions are assumed to be 100% dissipative. As reported in Ref. 41 and 42, active TPV cell area ratios of $\sim$ 90% are readily achievable. Using this information, we are able to estimate η_{TPV} for all the emitter-filter combinations considered at $F = 0.99$, results of which are marked by the crosses in Fig. 3-7 to clearly show the reduction in the effective F. Evidently, use of the cold-side tandem filter helps mitigate the effect of $< 100\%$ active cell area ratios.

3.3.3 Effect of Non-ideal Selective Emitter

As can be seen in Fig. 3-6, a selective emitter is critical for TPV systems without the optimized tandem filter. It is also observed that the optimized 2D Ta PhC emitter does not come close to achieving the performance of the ideal cutoff emitter. This is primarily due to long wavelength ε that is larger by a factor of two compared to the ideal cutoff emitter, which is inevitable even with a low ε polished metal given that intrinsic free electron damping losses significantly increase with the rise of temperature [37]. The question now lies as to how much improvement can be seen if long wavelength ε can be suppressed to hypothetical levels in future selective emitter development. To study this, let us compare the performance of a greybody emitter to an ideal cutoff selective

emitter with ε_{H} at $\lambda < \lambda_{\mathrm{g}}$ of $\varepsilon_{\mathrm{sw}} = 0.9$, and a varying ε_{H} at $\lambda > \lambda_{\mathrm{g}}$ of $\varepsilon_{\mathrm{lw}}$. Estimates of η_{TPV} for both emitters at $T = 1250\,\mathrm{K}$ (which is approximately the optimum for InGaAsSb TPV) with or without the 0.53 eV optimized tandem filter are presented in Figs. 3-8(a) and (b) for $F = 0.99$ and $F = 0.95$ ($100\,\mathrm{mm} \times 100\,\mathrm{mm}$ flat plate geometry with $s = 3\,\mathrm{mm}$) respectively. Evidently, use of a selective emitter results in markedly increased η_{TPV} over a greybody if the optimized tandem filter is absent. Notice that a larger relative improvement in η_{TPV} is seen compared to the relative reduction in $\varepsilon_{\mathrm{lw}}$. However, for a TPV system using only the ideal cutoff emitter for spectral control, $\varepsilon_{\mathrm{lw}}$ must be smaller than 0.03 to outperform the greybody – optimized tandem filter combination. Such a low $\varepsilon_{\mathrm{lw}}$ is unfortunately a necessity due to the large amount of spectral irradiance when integrated from $\lambda_{\mathrm{g}} < \lambda < 10\,\mu\mathrm{m}$. Materials with $\varepsilon_{\mathrm{lw}} < 0.03$ do not exist as yet, thus effective spectral control is more readily attainable using the cold-side optimized tandem filter compared to the hot-side selective emitter in high F TPV systems. If $F < 0.95$, both aspects of spectral control become important; a relative improvement $> 5\%$ over the greybody emitter is realized for $\varepsilon_{\mathrm{lw}} < 0.09$ when used in combination with the optimized tandem filter.

3.3.4 Effect of Non-ideal Cold-side Bandpass Filter

In this section, we consider the non-idealities that could be present in cold-side bandpass filters. First, let us consider an ideal cutoff filter with the following characteristics:

$$\begin{aligned} Tr &= 0.95 - \alpha_{\mathrm{F}} \quad : \lambda < \lambda_{\mathrm{c}} \\ R &= 1.00 - \alpha_{\mathrm{F}} \quad : \lambda > \lambda_{\mathrm{c}} \end{aligned}$$

where Tr is transmittance of the filter, and α_{F} is the absorptance of the filter over all λ's. These parameters are chosen as the approximate upper limit of bandpass filters [70, 72]. Using these, we can calculate η_{TPV} for InGaAsSb TPV systems at $T = 1250\,\mathrm{K}$ and $F = 0.99$ when coupled with the following previously discussed emitters: optimized 2D Ta PhC, greybody, and ideal cutoff emitter. In addition, α_{F} is varied from 0 to 0.05. The results are presented in Fig. 3-9(a). An $\sim 18\%$ relative reduction in η_{TPV} is seen for both the optimized 2D Ta PhC and greybody emitters, compared to a lower $\sim 12\%$ relative reduction for the ideal cutoff emitter when $\alpha_{\mathrm{F}} = 0.05$. This is expected

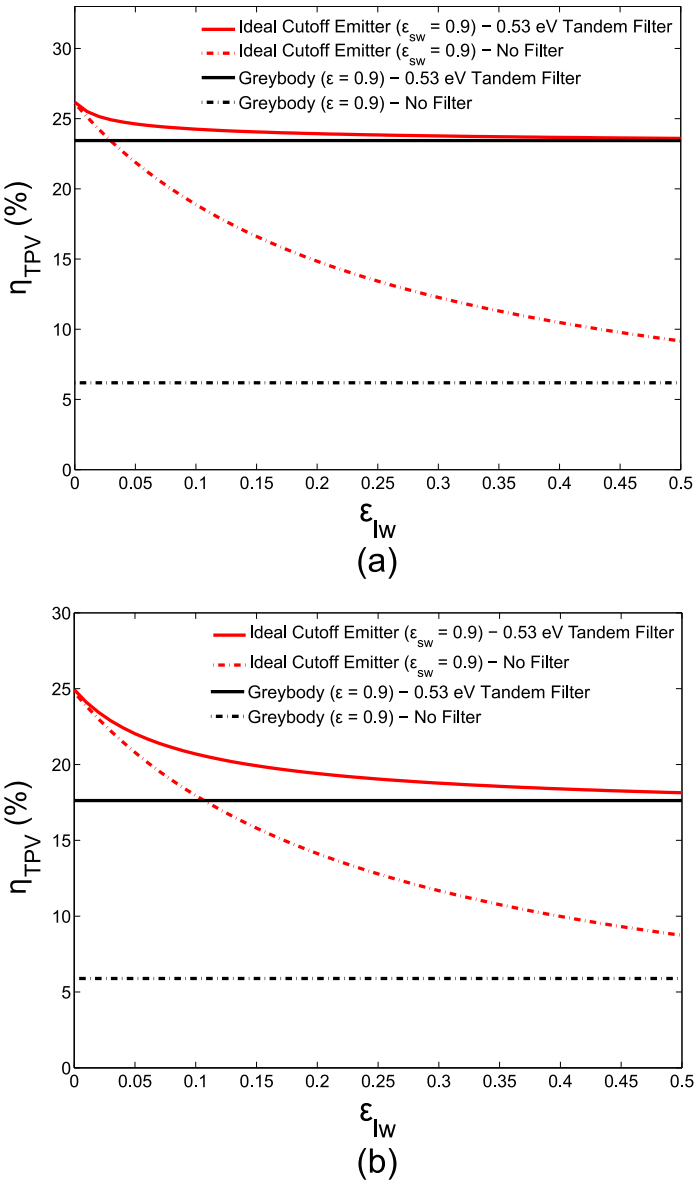

Figure 3-8: η_{TPV} for an InGaAsSb TPV system including an ideal cutoff emitter with ε_{H} at $\lambda < \lambda_{\mathrm{g}}$ of $\varepsilon_{\mathrm{sw}} = 0.9$, and a varying ε_{H} at $\lambda > \lambda_{\mathrm{g}}$ of $\varepsilon_{\mathrm{lw}}$ with or without a 0.53 eV optimized tandem filter at a fixed T of 1250 K. (a) $F = 0.99$. To outperform the greybody - optimized tandem filter combination, the solitary ideal cutoff emitter must possess $\varepsilon_{\mathrm{lw}} < 0.03$, to a point where addition of the tandem filter is detrimental given the larger reduction in power density for a small improvement in η_{TPV}. (b) $F = 0.95$ (100 mm × 100 mm flat plate geometry with $s = 3$ mm). To outperform the greybody - optimized tandem filter combination, the solitary ideal cutoff emitter must possess $\varepsilon_{\mathrm{lw}} < 0.10$. As F is reduced, both aspects of spectral control become important.

given that better selective emitters are necessary if filters are highly absorptive. The performance of the optimized tandem filter discussed in Section 3.2.3 are also put into context in Fig. 3-9(a) with marked crosses for the respective emitters, indicating an effective $\alpha_{\mathrm{F}} \sim 1\%$, which is consistent with results reported in Ref 70.

The other interesting aspect of bandpass filters is the bandwidth of high reflectance λ_{F}. Thus, let us consider an ideal cutoff filter with $\alpha_{\mathrm{F}} = 0$ and the following:

$$R = \begin{cases} 0.05 & : \lambda < \lambda_{\mathrm{c}} \\ 1.00 & : \lambda_{\mathrm{c}} < \lambda < \lambda_{\mathrm{c}} + \lambda_{\mathrm{F}} \\ 0.30 & : \lambda > \lambda_{\mathrm{c}} + \lambda_{\mathrm{F}} \end{cases}$$

Again, these values are estimates of upper limits of bandpass filters that could be realistically achieved based on reported results [70, 72]. As can be seen in Fig. 3-9(b), only $\sim 1\%$ absolute difference in η_{TPV} is seen for the greybody emitter compared to the optimized 2D Ta PhC selective emitter and the ideal cutoff emitter when $\lambda_{\mathrm{F}} = 10\,\mu\mathrm{m}$. For $\lambda_{\mathrm{F}} < 6\,\mu\mathrm{m}$, the optimized 2D Ta PhC selective emitter enables absolute improvement $> 3\%$ in η_{TPV} compared to the greybody emitter. Hence, when λ_{F} is small, it is more advantageous to employ the optimized 2D Ta PhC selective emitter. In Fig. 3-9(b), results using the optimized tandem filter discussed in Section 3.2.3 when coupled with the respective emitters are also indicated with marked crosses. An effective $\lambda_{\mathrm{F}} > 6\,\mu\mathrm{m}$ is seen, which is consistent with results reported in Ref 70. It is also important to note that even though the optimized tandem filter enables excellent TPV performance that is extremely close to the ideal cutoff filter, they are nevertheless extremely costly and difficult to fabricate, given the sheer number of layers (> 50 layers) and the specialty materials used (Sb_2Se_3, YF_3, and heavily doped InPAs). In Ref 72, it is reported that a much more practical 10 layer Si/SiO_2 filter stack can achieve $\lambda_{\mathrm{F}} \sim 2\,\mu\mathrm{m}$. When this filter is used instead, the 2D Ta PhC selective emitter enables up to $\sim 44\%$ relative improvement over the greybody emitter. In addition, the performance of the optimized 2D Ta PhC selective emitter based TPV system is improved by $\sim 50\%$ when the simple 10 layer Si/SiO_2 filter is present. Ultimately, the optimum combination would depend on cost and design goals.

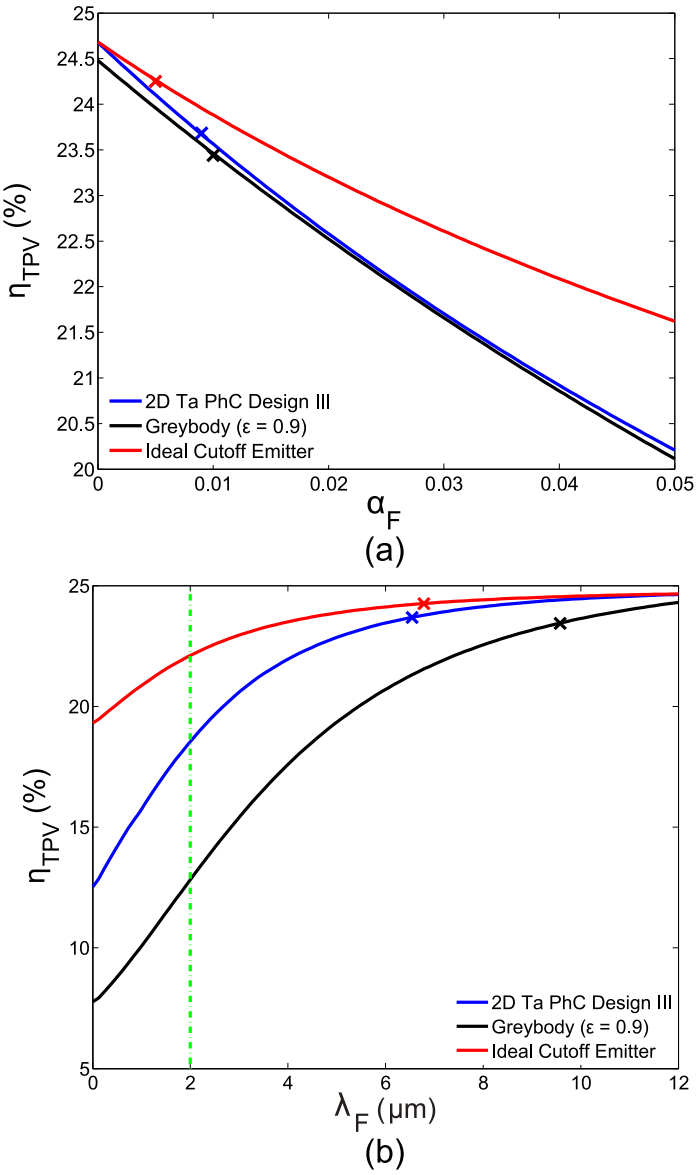

Figure 3-9: η_{TPV} for InGaAsSb TPV systems at $T = 1250\,\mathrm{K}$ and $F = 0.99$ using an ideal cutoff filter with: (a) $Tr = 0.95 - \alpha_{\mathrm{F}}$ at $\lambda < \lambda_{\mathrm{c}}$ and $R = 1.00 - \alpha_{\mathrm{F}}$ at $\lambda > \lambda_{\mathrm{c}}$, where α_{F} is the filter absorptance over all λ. (b) Varying high R bandwidth λ_{F} with $R = 0.05$ at $\lambda < \lambda_{\mathrm{c}}$, $R = 1.00$ at $\lambda_{\mathrm{c}} < \lambda < \lambda_{\mathrm{c}} + \lambda_{\mathrm{F}}$, and $R = 0.30$ at $\lambda > \lambda_{\mathrm{c}} + \lambda_{\mathrm{F}}$, assuming $\alpha_{\mathrm{F}} = 0$. The crosses are simulation results for the respective systems when the optimized tandem filter discussed in Section 3.2.3 is used instead. The green line is just a guide to the eye for the performance using a simple $\lambda_{\mathrm{F}} = 2.00\,\mu\mathrm{m}$ filter.

3.3.5 Effect of Non-ideal Thermophotovoltaic Cells

From 1975 to 2000, efficiencies of Si PV cells under AM1.5G solar irradiance have more than doubled from 13% to 25% [91]. In fact, the latest state of the art Si PV cells approach $\sim 85\%$ of their theoretical thermodynamic limit [92], a feat made even more impressive given that Si has an indirect bandgap. It is thus reasonable to envision a similar path followed by direct low bandgap TPV cells if similar research efforts are undertaken, upon which would lead to significantly higher η_{TPV}.

To quantify the possible increase in η_{TPV}, let us consider TPV cells limited only by thermalization losses and radiative recombination, i.e. the Shockley-Queisser limit [93]. This is easily implemented in the model described in Section 3.2.1 by setting $R_{\mathrm{s}} = 0$, $R_{\mathrm{sh}} = \infty$, and $m = 1$ in Eq. (3.10). In addition, I_{o} is set to the thermodynamic limit determined solely by radiative recombination [92]:

$$I_{\mathrm{o}} = \frac{A_2 q(n^2+1)E_{\mathrm{g}}^2 kT_{\mathrm{c}}}{4\pi^2\hbar^3c^2}\exp(-E_{\mathrm{g}}/kT_{\mathrm{c}}) \tag{3.16}$$

where n is the refractive index of the TPV semiconductor region, E_{g} is the energy gap of the TPV cell, and $\hbar = h/2\pi$. Lastly, the ideal TPV cell is assumed to possess an EQE(λ) of 1 at $\lambda < \lambda_{\mathrm{g}}$ and 0 at $\lambda > \lambda_{\mathrm{g}}$. Using this, predicted $\eta_{\mathrm{TPV,\,max}}$ and corresponding $J_{\mathrm{elec,\,max}}$ for all emitter-filter-TPV cell combinations are obtained and are presented in Table 3.1. Note that the 2D Ta PhC selective emitters, filters, and T's indicated in brackets are optimized for current state of the art low bandgap TPV cells (GaSb [82], InGaAs [41], and InGaAsSb [82]). In addition, the contribution of reabsorption of photons generated by radiative recombination in the TPV cells by the emitter is neglected, since it is much smaller than P_{em}, and that typical maximum power operation extracts $> 90\%$ of the photocurrent generated. If this contribution is included, we expect $< 5\%$ relative increase in η_{TPV} estimates for the ideal cell.

As can be seen in Table 3.1, current state-of-the-art fabricated TPV cells are $\sim 50\%$ as efficient as their thermodynamically ideal counterparts. For the InGaAsSb TPV system utilizing the optimized tandem filter and the optimized 2D Ta PhC selective emitter at the optimum operating $T = 1260\,\mathrm{K}$, $\sim 12\%$, $\sim 28\%$, and $\sim 13\%$ of the losses are attributable to non-ideal EQE, non-radiative

Table 3.1: Predicted $\eta_{\text{TPV, max}}$ and corresponding $J_{\text{elec, max}}$ for three different TPV cells utilizing experimentally realizable spectral control components at fixed $F = 0.99$. Optimum T indicated in brackets is determined for each TPV system combination using fabricated and characterized TPV cells (GaSb [82], InGaAs [41], and InGaAsSb [82]). Tandem filter is the plasma-dielectric filter discussed in Section 3.2.3 and Si/SiO2 filter is the simple 10 layer filter discussed in Section 3.3.4. Results indicate that current state of the art fabricated TPV cells are $\sim 50\%$ as efficient as their thermodynamically ideal counterparts. It is also interesting to note that spectral control via the optimized 2D Ta PhC and tandem filter enables TPV cells with larger bandgaps (GaSb) to perform as well as TPV cells with smaller bandgaps (InGaAsSb). However, the use of smaller bandgap TPV cells would result in lower optimum T's.

TPV System	Predicted $\eta_{\text{TPV, max}}$ (%), $J_{\text{elec, max}}$ (W/cm^2)					
	GaSb		InGaAs		InGaAsSb	
	Fabricated Cell [82]	Ideal Cell	Fabricated Cell [41]	Ideal Cell	Fabricated Cell [82]	Ideal Cell
Optimized 2D Ta PhC & Tandem Filter	22.8%, 0.58 W/cm^2 (1390 K)	45.9%, 1.25 W/cm^2 (1390 K)	25.0%, 0.68 W/cm^2 (1320 K)	45.5%, 1.23 W/cm^2 (1320 K)	23.7%, 0.62 W/cm^2 (1260 K)	45.0%, 1.17 W/cm^2 (1260 K)
Greybody ($\varepsilon = 0.9$) & Tandem Filter	22.3%, 0.59 W/cm^2 (1360 K)	45.6%, 1.29 W/cm^2 (1360 K)	24.8%, 0.71 W/cm^2 (1290 K)	45.4%, 1.30 W/cm^2 (1290 K)	23.5%, 0.66 W/cm^2 (1230 K)	45.4%, 1.27 W/cm^2 (1230 K)
Optimized 2D Ta PhC & Si/SiO_2 Filter	16.6%, 0.95 W/cm^2 (1510 K)	37.6%, 2.29 W/cm^2 (1510 K)	19.7%, 1.04 W/cm^2 (1420 K)	39.1%, 2.06 W/cm^2 (1420 K)	19.2%, 0.98 W/cm^2 (1370 K)	39.8%, 2.08 W/cm^2 (1370 K)
Greybody ($\varepsilon = 0.9$) & Si/SiO_2 Filter	10.6%, 1.20 W/cm^2 (1540 K)	27.6%, 3.23 W/cm^2 (1540 K)	13.7%, 1.41 W/cm^2 (1460 K)	30.0%, 3.11 W/cm^2 (1460 K)	14.0%, 1.35 W/cm^2 (1410 K)	32.5%, 3.23 W/cm^2 (1410 K)
Optimized 2D Ta PhC	9.2%, 1.11 W/cm^2 (1560 K)	23.3%, 2.98 W/cm^2 (1560 K)	12.8%, 1.30 W/cm^2 (1470 K)	25.9%, 2.71 W/cm^2 (1470 K)	13.0%, 1.26 W/cm^2 (1440 K)	29.1%, 2.98 W/cm^2 (1440 K)
Greybody ($\varepsilon = 0.9$)	4.5%, 1.28 W/cm^2 (1570 K)	12.6%, 3.87 W/cm^2 (1570 K)	7.0%, 1.62 W/cm^2 (1490 K)	15.1%, 3.75 W/cm^2 (1490 K)	7.5%, 1.63 W/cm^2 (1470 K)	18.7%, 4.42 W/cm^2 (1470 K)

recombination mechanisms, and R_s respectively. R_s is also the main cause of lower optimum operating T. As T approaches 1800 K, the proportion of losses attributable to R_s increases to $\sim$ 40%.

The most efficient TPV system that can be assembled today consists of the experimentally demonstrated InGaAs TPV cells in combination with an optimized 2D Ta PhC selective emitter and an optimized cold-side tandem filter. This system exhibits $\eta_{TPV} = 25\%$ and $J_{elec,\,max} = 0.68\,W\,cm^{-2}$ at realistic $T = 1320\,K$ and $F = 0.99$. η_{TPV} for this configuration is $\sim 55\%$ of the ideal TPV cell limit shown in Table 3.1. If TPV cells are to follow a similar research path witnessed by Si PV cells (reaching $\sim 85\%$ of their theoretical thermodynamic limit), η_{TPV} for this system could reach $\sim$ 40%. Note that the theoretical 0.62 eV single bandgap TPV thermodynamic efficiency limit (with ideal TPV cell and ideal spectral control, which is analogous to the Shockley-Queisser limit for Si PV), and the theoretical infinite bandgaps TPV thermodynamic efficiency limit (i.e. the Carnot efficiency limit) are respectively 55% and 77% at $T = 1320\,K$ and $T_c = 300\,K$.

3.3.6 Comparisons with Notable Thermophotovoltaic Experimental Efforts

To the best of our knowledge, the highest radiant heat-to-electricity efficiency reported to date is 23.6% with $J_{elec,\,max} = 0.79\,W\,cm^{-2}$ at $T = 1312\,K$ using InGaAs cells attached with a similar cold-side bandpass filter described in Section 3.2.3, and a greybody-like SiC emitter [81]. Note, however, that this measurement does not include optical cavity losses. If optical cavity losses are included, our numerical model predicts $\eta_{TPV} = 19.9\%$ and $J_{elec,\,max} = 0.80\,W\,cm^{-2}$, which is in good agreement with the reported results. A similar experiment, albeit with modifications to include optical cavity losses, and using a greybody-like graphite emitter instead, resulted with η_{TPV} = 19.1% and $J_{elec,\,max} = 0.66\,W\,cm^{-2}$ at $T = 1350\,K$ [14]. Our numerical model, which does not include cell array losses, predicts $\eta_{TPV} = 20.1\%$ and $J_{elec,\,max} = 0.73\,W\,cm^{-2}$. If the greybody-like graphite emitter is substituted with an optimized 2D Ta PhC, the TPV system can achieve η_{TPV} = 20.6% and $J_{elec,\,max} = 0.76\,W\,cm^{-2}$. Due to the marginal improvements, a greybody-like emitter would be a better choice in a high F system if an optimized tandem filter is present. This result also highlights the need for developing selective emitters that approach the ideal cutoff emitter,

possess ultra low ε_{lw}, and maintain selectivity over all angles, in order to maintain its relevance in advancing the performance of TPV systems.

For GaSb based TPV systems, the highest radiant heat-to-electricity efficiency reported to date is 21.5% (does not include optical cavity losses) with $J_{\text{elec, max}} = 1.50\,\text{W cm}^{-2}$ at $T = 1548\,\text{K}$ using an ARC W emitter with a dielectric filter that transmits useful photons of $\lambda < 1.8\,\mu\text{m}$ while reflecting over 95% the photons within $1.8\,\mu\text{m} < \lambda < 3.5\,\mu\text{m}$ [94]. If optical cavity losses are included in a $F = 0.99$ system, η_{TPV} is estimated to be 18.1%. This is consistent with the results presented in Table 3.1. These results also reveal another interesting aspect; spectral control is a great equalizer between different TPV cell technologies. Hence, the simpler, cheaper, and more robust GaSb cells might be the future way forward for practical TPV systems.

In Fig. 3-10, results of various TPV experimental efforts to-date [14, 56, 58, 62, 81, 94–100] are compiled and presented. We have attempted to make this as complete as possible to the best of our knowledge, while only including reports with sufficient credible data. It is unfortunate that the TPV research community has not agreed on a general metric that would allow convenient comparison between various research efforts, which is also understandable given the difficulty in accurate measurements and the different metrics of interest. Some report entire system efficiency [58, 62, 97, 99, 100]; some define η_{TPV} without including cavity effects [56, 81, 94–98]; only Crowley *et al.* individually measured η_{TPV}, η_{cell}, and $\eta_{\text{cav-spec}}$ [14]. Thus, in order to make a fair comparison, the plotted data in Fig. 3-10 is our best estimate of η_{TPV} based on reported parameters. In addition, theoretical efficiency limits, namely Carnot, ideal single junction ($E_{\text{g}} = 0.55$ eV), ideal dual junction ($E_{\text{g}} = 0.55$ eV and 0.75 eV), and ideal triple junction ($E_{\text{g}} = 0.55$ eV, 0.70 eV, and 0.90 eV) are also plotted for $T = 1500\,\text{K}$ to show the remaining potential for future improvement. Note that for the ideal dual and triple junction cells, E_{g}'s of the lowest bandgap cell are fixed to 0.55 eV, i.e. an InGaAsSb cell available today, while the remaining E_{g}'s are chosen to obtain the highest efficiency at $T = 1500\,\text{K}$. Current matching is neglected, and ideal spectral control is assumed for all ideal theoretical limits. We also plot η_{TPV} for a blackbody ($\varepsilon = 1$) at $T = 1500\,\text{K}$ with no spectral control using today's state-of-the-art InGaAsSb TPV cells. It is also interesting to include η_{TPV} estimates for optimized 2D Ta PhC in combination with filters that can be fabricated today at $F = 0.99$,

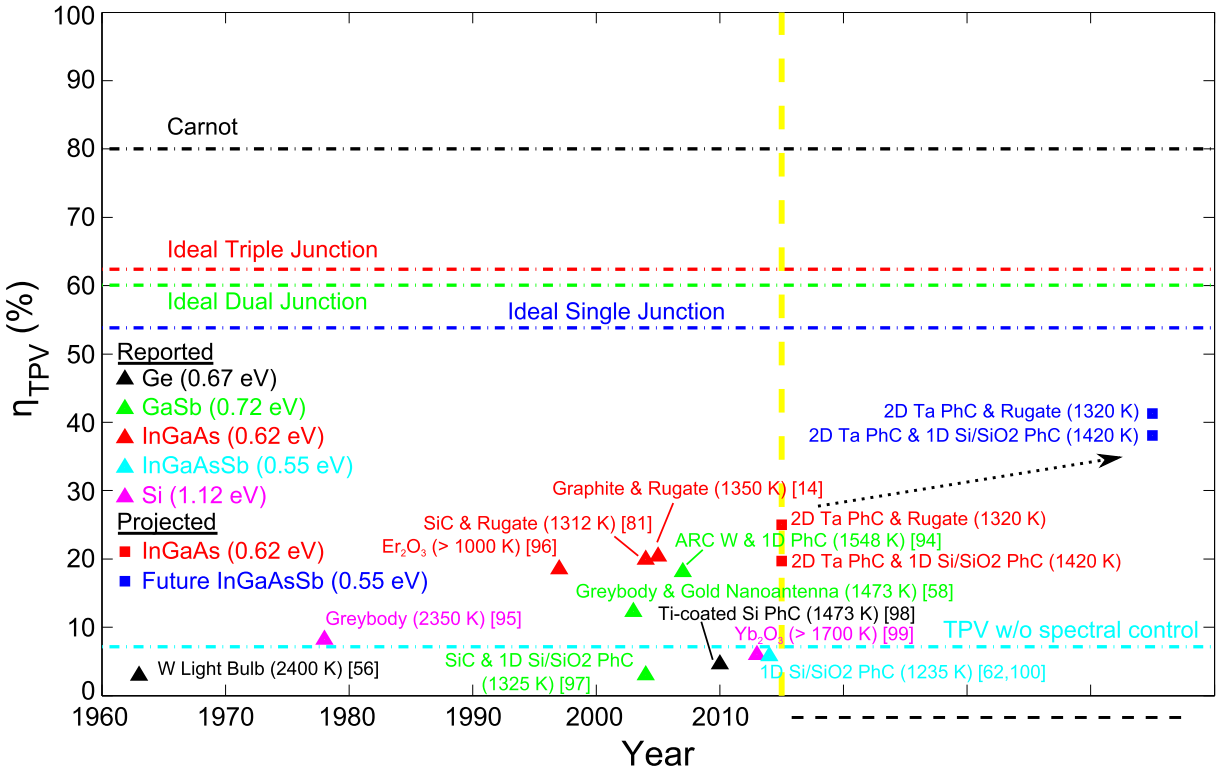

Figure 3-10: η_{TPV} of reported TPV experimental efforts to-date [14, 56, 58, 62, 81, 94–100] using various TPV cells, emitters, with or without a cold-side filter, each indicated using the following format: Emitter & Filter (T). Dotted-dashed lines are efficiency limits at $T = 1500\,\text{K}$, with the lowest bandgap cell fixed at $E_g = 0.55$ eV. For ideal dual and triple junction, the remaining E_g's are fixed at their optimum. Yellow dashed line indicates the year 2015.

i.e. the best TPV systems that can be built today, of which would outperform the best reported TPV experimental result by a few percent absolute. If single junction TPV cells could advance to $\sim 85\%$ of their ideal thermodynamic limit, which is not unreasonable given that Si cells have already achieved this target, we will obtain $\sim 78\%$ of the ideal spectral control single junction limit even with today's spectral control components. This is an extremely strong indication that today's spectral control components are very close to ideal, yet a lot more gains can be achieved if efforts are made towards advancing TPV cell technology.

3.4 Conclusions

Spectral control via selective emitters and/or cold-side filters is vital towards achieving higher TPV efficiencies. Amongst experimentally demonstrated selective emitters, 2D Ta PhC's hold great promise due to ease of design, large area fabrication, system integration, and ability to withstand extended operation at high temperatures. Most importantly, the selectivity enables $>$ 100% improvement over a greybody emitter ($\varepsilon = 0.9$).

The optimum spectral control approach depends on the achievable view factor, F, of which in a practical system, depends on the physical separation of the emitter and the PV cell, as well as PV cell front contact shadowing and stitching area losses from connecting multiple PV cells. For $F >$ 0.97 (100 mm $\times$ 100 mm flat plate geometry with separation $s < 1.7$ mm), the greybody emitter outperforms the 2D Ta PhC emitter when coupled with an optimized cold-side tandem filter. This is due to high photon recycling efficiency at large F. Thus, in order for selective emitters to remain relevant in future high-F TPV systems, it is crucial that further research efforts are undertaken to substantially reduce both long wavelength emittance and angular dispersion. Regardless, as $F <$ 0.97, use of both the selective emitter and the cold-side filter becomes necessary for maximum TPV efficiencies.

By combining an optimized 2D Ta PhC selective emitter with an optimized cold-side tandem filter, a TPV energy conversion system with radiant heat-to-electricity efficiency of 25% and power density of 0.68 W cm^{-2} can be achieved using experimentally demonstrated InGaAs TPV cells at realistic emitter temperature of 1320 K and $F = 0.99$ (achievable with 100 mm $\times$ 100 mm flat plate geometry with $s = 500$ µm). Interestingly, a performance approaching $\sim$ 80% of this can be achieved with the simpler and more practical Si/SiO_2 filter. The efficiency could be increased to $\sim$ 40% absolute (the theoretical 0.62 eV single bandgap TPV and infinite bandgaps TPV thermodynamic limit at emitter temperature of 1320 K and cell temperature of 300 K are 55% and 77% respectively) if TPV cells are to follow a similar research path witnessed by Si PV cells, thus paving the way towards widespread adoption of what may be a promising highly efficient, portable, and reliable energy conversion system.

3.A Appendix: Accuracy of Using Spectral Hemispherical Emittance to Approximate Full Ray Tracing Thermophotovoltaic System Model

At the end of Section 3.2.1, it is mentioned that the spectral hemispherical (diffused) approximation using Eq. (3.14) produce results that agree extremely well with the full ray tracing approach captured by Eqs. (3.7)–(3.9). Indeed, the agreement is excellent as shown in Fig. 3-11. These results are for a TPV system comprising an optimized 2D Ta PhC emitter coupled with a state-of-the-art Si PV cell [101] in a 100 mm × 100 mm flat plate geometry with $s = 500\,\mu\text{m}$. In the full ray tracing model, $\mathrm{d}A$ is set to 500 µm × 500 µm, and the summation of P_{re} in Eq. (3.7) and I_{sc} in Eq. (3.9) are respectively limited to the first 20 and 5 terms to ensure the simulation remains tractable. In addition, rays traveling beyond $\theta = 80^\circ$ are ignored. Even with these simplifications, the ray tracing method is approximately 100× slower than the diffused spectral hemispherical approximation. Hence, the diffused spectral hemispherical approximation is the method of choice when searching for the optimum design.

At higher T's, which is approximately 1600 K and above for the optimized 2D Ta PhC and Si PV combination, the diffused spectral hemispherical approximation starts to underestimate when compared to the full ray tracing model, i.e. slightly higher η_{TPV} and J_{elec} are predicted when using the full ray tracing model. This is due to larger η_{cell} and J_{elec} predicted by the full ray tracing model, which is most likely the artifact of $\mathrm{d}A$ not being small enough compared to s, thus putting a slightly larger weighting on normal incidence emittance. Regardless, both models predict the same trends.

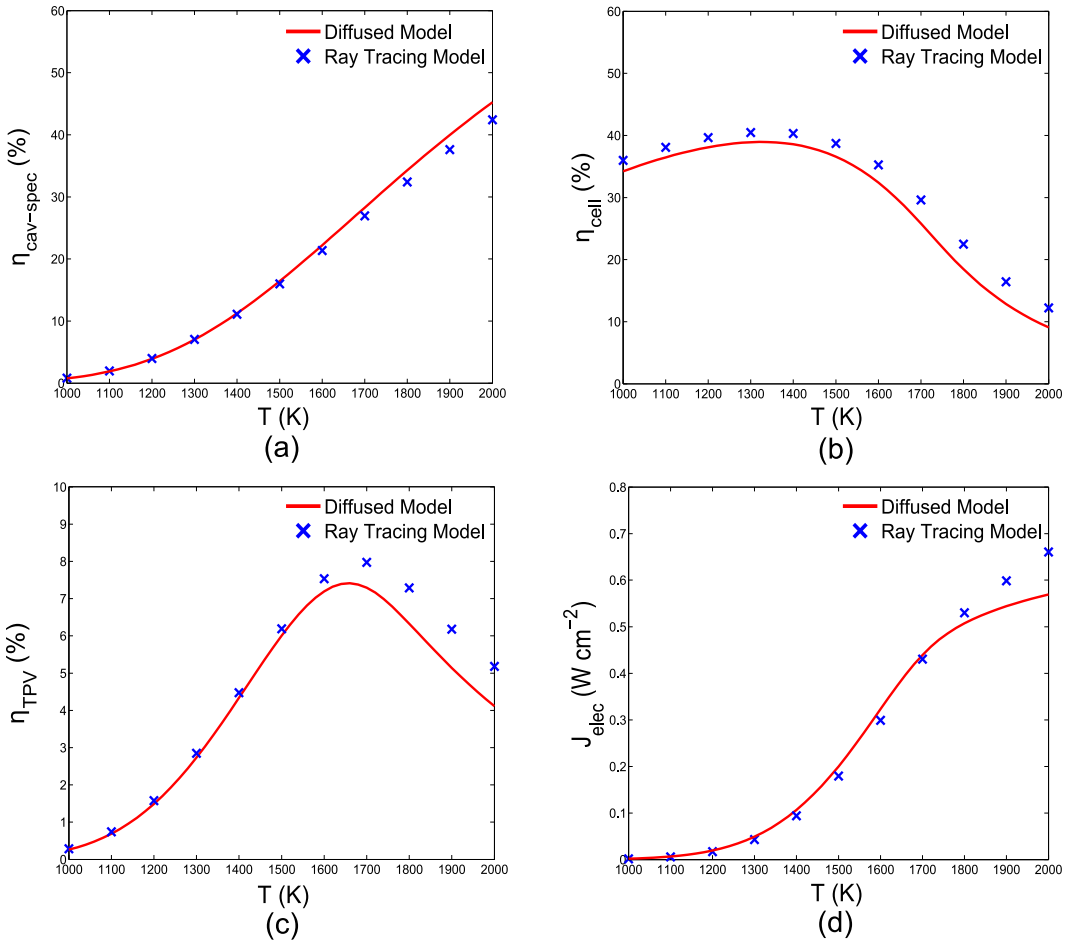

Figure 3-11: Comparison between spectral hemispherical (diffused) approximation and the full ray tracing TPV model for (a) $\eta_{\text{cav-spec}}$ (b) η_{cell} (c) η_{TPV} (d) J_{elec}. These results are for a TPV system comprising an optimized 2D Ta PhC emitter coupled with a state-of-the-art Si PV cell [101].

Chapter 4

Dielectric-filled Anti-reflection Coated Two-dimensional Metallic Photonic Crystals for Omnidirectional Wavelength Selective Emission

As discussed in Chapter 2, 2D MPhCs show great potential as selective emitters due to its high temperature stability and fabrication scalability. However, the traditional unfilled 2D MPhC only retains its selectivity and performance for polar angles $\theta \lesssim 35°$. Such limited angular emission profiles negatively impact the overall efficiency and power density when using the 2D MPhC as selective emitters in TPV applications as shown in Chapter 3. In this chapter, we report the design of dielectric-filled ARC 2D MPhCs capable of omnidirectional, polarization insensitive, wavelength selective emission, thus overcoming the aforementioned shortcomings of the traditional unfilled 2D MPhCs. First, we will uncover the theory behind the emission enhancement. Next, optimized dielectric-filled ARC 2D Ta PhC designs found using non-linear global optimization methods will be presented. Finally, we will evaluate the various selective emitters in TPV energy conversion systems.

4.1 Introduction

Thermal radiation of naturally occurring materials is usually broadband and has a magnitude far weaker compared to the ideal blackbody, rendering it inefficient for many applications, for instance as an infrared source in sensing applications [20, 21], as an emitter in TPV energy conversion [18, 77, 83], and as a solar absorber [15, 33, 46]. For many of these applications, it is desirable to accurately control thermal radiation such that thermal emission occurs only in certain wavelength ranges over an optimum angular spread. For instance, TPV benefits from the use of omnidirectional selective emitters [83], while angularly selective absorption results in a more efficient solar absorber [46–48, 63].

With the recent advancements in nanofabrication, various 1D [21, 22, 24, 67], 2D [17, 23, 25, 27, 28, 31, 45, 68, 102], and 3D [12, 26, 29, 69] periodic structures have been extensively investigated both theoretically and experimentally in order to achieve accurate control of thermal radiation. The first class of these relies on excitation of surface phonon-polaritons [22], surface plasmon-polaritons [21, 23, 103], and localized plasmon resonances [104]. These mechanisms usually result in very sharp and narrow thermal emission linewidths with respect to wavelength, and can be designed to emit over restricted [22, 103] or wide polar angles [102, 104]. Thermal emission can also be enhanced by coupling to magnetic polaritons to obtain narrowband emission over wide polar angles [105].

In certain applications, for instance as an emitter in TPV systems, it is however more advantageous to broaden the bandwidth of emission such that high ε is retained at $\lambda < \lambda_c$ while maintaining ultra low ε at $\lambda > \lambda_c$ over all polar angles and polarizations. In this respect, metamaterial designs based on metal-dielectric stacks [106] and 2D metallic pyramid arrays [17] show great promise. However, they are difficult to fabricate and have not been experimentally demonstrated at high temperatures under extended operation. Here, we present a simpler approach based on dielectric-filled 2D MPhCs to obtain omnidirectional polarization insensitive wavelength selective thermal emission.

4.2 Design and Optimization

The traditional unfilled 2D MPhCs rely on cavity resonances to achieve selective emission, whereby λ_c is determined by the fundamental cavity resonance frequency as discussed previously in Chapter 2. This relatively simple design allows one to simultaneously achieve near-blackbody $\varepsilon_\perp$ at $\lambda < \lambda_c$ as well as $\varepsilon_\perp$ almost as low as a polished metal at $\lambda > \lambda_c$, with a sharp cutoff separating the two regimes.

As in Chapter 3, we used NLOpt, a non-linear optimization package developed at MIT [89], to obtain 2D Ta PhC designs optimized for maximum $\varepsilon_H(\lambda)$ at $\lambda < \lambda_c$ and minimum $\varepsilon_H(\lambda)$ at $\lambda > \lambda_c$. The design provided by Q-matching of the fundamental mode was used as the initial starting point of the optimization algorithm. In addition, the following constraints were implemented: $a - 2r \geq 100\,\text{nm}$ to ensure integrity of sidewalls; $d \leq 8.50\,\mu\text{m}$ based on fabrication limits using an SF_6 based DRIE Bosch process [79]. Rigorous coupled wave analysis methods (RCWA) [108] coupled with the Lorentz–Drude model of Ta fitted to experimentally measured R at room T [80] were used to obtain R, from which we can infer ε via Kirchhoff's law [38].

Fig. 4-1(a) & (c) shows $\varepsilon(\lambda, \theta)$ averaged over ϕ and over both polarizations of the unfilled 2D Ta PhC optimized for maximum $\varepsilon_H(\lambda)$ at $\lambda < \lambda_c = 2.00\,\mu\text{m}$ and minimum $\varepsilon_H(\lambda)$ at $\lambda > \lambda_c$. As can be seen, $\varepsilon(\lambda, \theta)$ at $\lambda < \lambda_c$ for the regular unfilled 2D Ta PhC falls dramatically as a function of θ. This severely reduces the magnitude of $\varepsilon_H(\lambda)$ at $\lambda < \lambda_c = 2.00\,\mu\text{m}$. In other words, wavelength selectivity is lost for $\varepsilon_H(\lambda)$. The main reason for this reduction is diffraction losses as detailed in Section 2.2.1. According to Eq. (2.2), radiation with $\lambda = 2\,\mu\text{m}$ will get diffracted when $\theta_i > \theta_d = 46.4°$ for $a = 1.16\,\mu\text{m}$. Above the diffraction threshold, $\varepsilon(\lambda, \theta)$ decreases because there are more channels to couple into, resulting in a smaller Q_{rad}, thus destroying Q-matching. This effect is clearly observed in Fig. 4-1(c) as indicated by the white lines, which are the diffraction thresholds determined using Eq. (2.2). Hence, in order to reduce diffraction losses, it is imperative to lower the diffraction thresholds by reducing a as much as possible.

A simple solution to reduce a is filling the cylindrical cavities with an appropriate dielectric, thereby increasing θ_d by virtue of a reduced r, d, and hence a to obtain the same λ_c due to a reduced

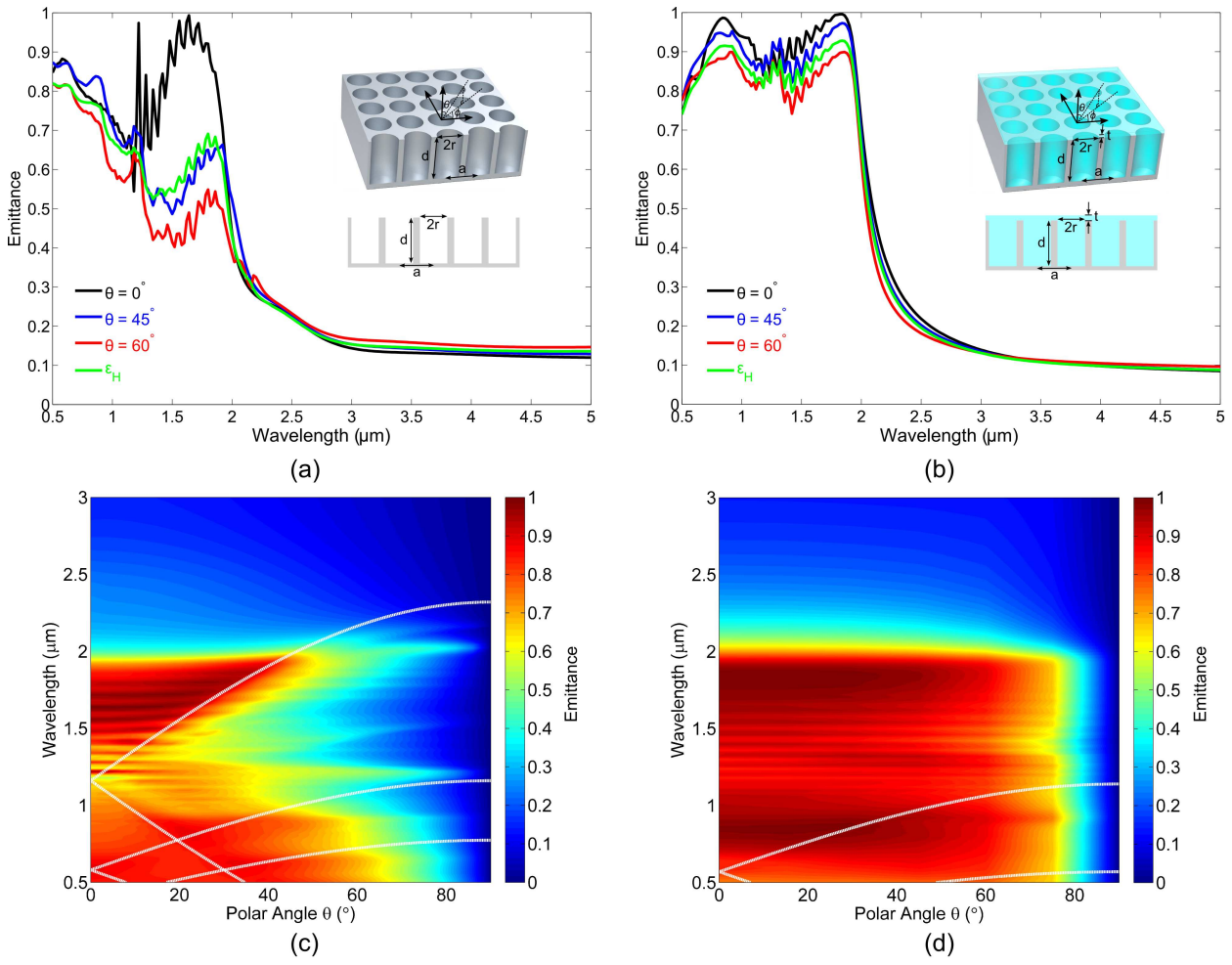

Figure 4-1: $\varepsilon(\lambda, \theta)$ averaged over ϕ and over all polarizations for (a) optimized unfilled 2D Ta PhC for $\lambda_c = 2.00\,\mu m$ ($r = 0.53\,\mu m$, $d = 8.50\,\mu m$, $a = 1.16\,\mu m$) and (b) optimized hafnium oxide HfO_2-filled ARC 2D Ta PhC for $\lambda_c = 2.00\,\mu m$ ($r = 0.23\,\mu m$, $d = 4.31\,\mu m$, $a = 0.57\,\mu m$, and an additional coating using the same dielectric with thickness $t = 78\,nm$ that functions as an ARC). HfO_2 is depicted by the cyan-coloured areas in the inset. The optimized HfO_2-filled ARC 2D Ta PhC has a much more superior $\varepsilon_H(\lambda)$ compared to the unfilled 2D Ta PhC. Note that d is limited to $8.50\,\mu m$ based on fabrication limits using an SF_6 based DRIE Bosch process [79]. (c) Contour plots of $\varepsilon(\lambda, \theta)$ for optimized 2D Ta PhC and (d) optimized HfO_2-filled ARC 2D Ta PhC. White lines indicate the diffraction thresholds as defined by Eq. (2.2).

effective wavelength (by a factor of n) in dielectrics [107]. In this investigation, we further optimize the design using non-linear global optimization methods to achieve the best possible performance, i.e. maximum $\varepsilon_{\mathrm{H}}(\lambda)$ at $\lambda < \lambda_{\mathrm{c}}$ and minimum $\varepsilon_{\mathrm{H}}(\lambda)$ at $\lambda > \lambda_{\mathrm{c}}$. In addition, we consider an additional coating of the same dielectric with thickness t that enhances $\varepsilon_{\mathrm{H}}(\lambda)$ at $\lambda < \lambda_{\mathrm{c}}$ by functioning as an ARC.

Hafnium oxide (HfO_2) is the dielectric material of choice in this investigation because of its transparency in the visible and IR region, its compatible thermal expansion coefficient, and its high melting point. HfO_2 can also be easily deposited via atomic layer deposition (ALD) [80], and sol-gel deposition methods [109]. In addition, the HfO_2 layer promotes stable operation at high temperatures by preventing detrimental chemical reactions that attack the metallic surface, and preventing geometry deformation due to surface diffusion [80, 109]. In subsequent simulations, the refractive index n of HfO_2 is assumed to be 1.9 for $0.50\,\mu\mathrm{m} < \lambda < 5.00\,\mu\mathrm{m}$, which is consistent with results reported in literature [110], as well as with our measurements of HfO_2 thin films deposited via ALD (Cambridge NanoTech Savannah).

Results of non-linear global optimization routines applied to HfO_2-filled ARC 2D Ta PhC for $\lambda_{\mathrm{c}} = 2.00\,\mu\mathrm{m}$ are shown in Fig. 4-1(b) & (d). As can be seen, the optimized HfO_2-filled ARC 2D Ta PhC more closely approaches the ideal cutoff emitter ($\varepsilon_{\mathrm{H}}(\lambda) = 1$ at $\lambda < \lambda_{\mathrm{c}}$ and $\varepsilon_{\mathrm{H}}(\lambda) = 0$ at $\lambda > \lambda_{\mathrm{c}}$); $\varepsilon(\lambda, \theta)$ is essentially unchanged up to $\theta = 40°$, and $\varepsilon(\lambda, \theta) \gtrsim 0.8$ for $\theta < 70°$ at $\lambda < \lambda_{\mathrm{c}}$, a significant improvement compared to the traditional unfilled 2D Ta PhC. In addition, $\varepsilon(\lambda, \theta)$ at $\lambda > \lambda_{\mathrm{c}}$ is lower by ≈ 0.03 primarily due to smaller surface fraction of dielectric to metal. The HfO_2-filled ARC 2D Ta PhC can also be easily optimized for different λ_{c}'s as illustrated in Fig. 4-2. There is also the added flexibility of using other suitable dielectric materials, for instance silicon dioxide (SiO_2) which has $n \approx 1.45$ [111]. As shown in Fig. 4-3, optimized HfO_2-filled and SiO_2-filled ARC 2D Ta PhCs show very similar performance. However, when using dielectrics with smaller n's, larger r, d, a, and t are necessary to achieve optimal performance as shown in Table 4.1. The eventual choice will nevertheless depend more on cost, as well as thermal stability.

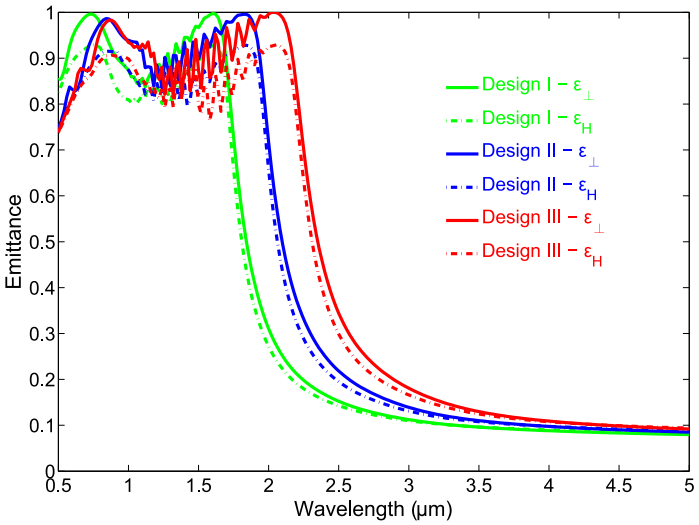

Figure 4-2: Optimized HfO_2-filled ARC 2D Ta PhC designs for $\lambda_c = 1.70\,\mu m$ ($r = 0.19\,\mu m$, $d = 3.62\,\mu m$, $a = 0.49\,\mu m$, $t = 63\,nm$), $\lambda_c = 2.00\,\mu m$ ($r = 0.23\,\mu m$, $d = 4.31\,\mu m$, $a = 0.57\,\mu m$, $t = 78\,nm$), and $\lambda_c = 2.30\,\mu m$ ($r = 0.27\,\mu m$, $d = 5.28\,\mu m$, $a = 0.64\,\mu m$, $t = 80\,nm$). λ_c can easily be shifted by altering r, d, a, and t and further fine tuned using global non-linear optimization routines.

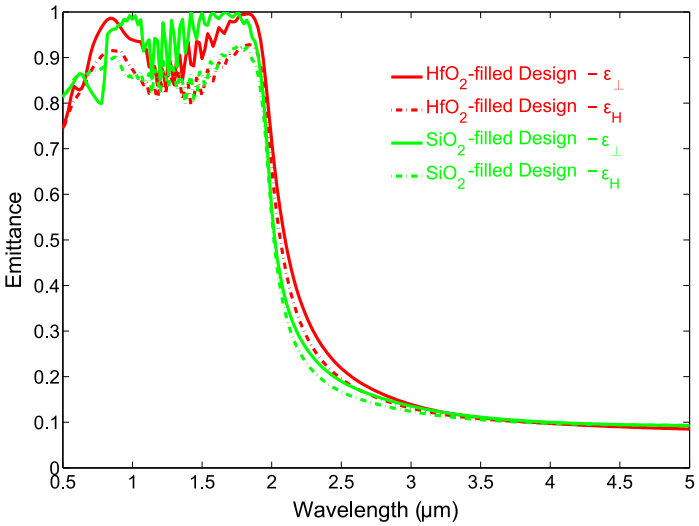

Figure 4-3: Comparison between optimized HfO_2-filled ($n \approx 1.9$) and SiO_2-filled ($n \approx 1.45$) ARC 2D Ta PhCs for $\lambda_c = 2.00\,\mu m$. Similar performance is obtained, albeit at a penalty of larger r, d, a, and t when using dielectrics with smaller n as shown in Table 4.1.

Table 4.1: Relevant dimensions of the dielectric-filled ARC 2D Ta PhCs optimized for $\lambda_c = 2.00\,\mu m$ using different dielectric material choices. The larger the refractive index n, the smaller r, d, a, and t is for the optimized structure.

Dielectric	r (µm)	d (µm)	a (µm)	t (nm)
Air (n = 1)	0.53	8.50	1.16	N/A
SiO_2 (n = 1.45)	0.35	6.28	0.80	125
HfO_2 (n = 1.90)	0.23	4.31	0.57	78

4.3 Analysis and Discussion

4.3.1 Polarization Dependence

At normal incidence, the dielectric-filled 2D MPhC is polarization independent due to the circular symmetry of the cylindrical cavities. However, as θ increases, slight differences can be seen in $\varepsilon(\lambda, \theta)$ between the transverse electric (TE) and transverse magnetic (TM) polarization as shown in Fig. 4-4. Note that $\varepsilon(\lambda, \theta)$ remains virtually constant with respect to $\phi = 0°$–$45°$, thus $\varepsilon(\lambda, \theta)$ is obtained by averaging over ϕ.

For $\theta \lesssim 50°$, $\varepsilon(\lambda, \theta)$ is almost identical for TE and TM polarizations as shown in Fig. 4-4. There are minute differences in the locations of the peaks since different TE and TM cavity resonances are excited in each case. Nevertheless, the resonance λ's are close to one another, such that the overall $\varepsilon(\lambda, \theta)$ profile is nearly identical. The HfO_2-filled ARC 2D Ta PhC is thus virtually polarization insensitive for $\theta \lesssim 50°$.

In contrast, at $\theta \gtrsim 60°$, $\varepsilon(\lambda, \theta)$ is on average larger for TM polarization compared to TE polarization. This is due to the reduction of reflectance at the air–dielectric interface in the vicinity of the Brewster angle given by $\arctan(n)$, which is $\backsimeq 63°$ for air–HfO_2 interface. In fact, $\varepsilon(\lambda, \theta)$ peaks around the Brewster angle for λ's larger than the 1st order diffraction threshold indicated by the white lines. In contrast, $\varepsilon(\lambda, \theta)$ for TE polarization progressively decreases as θ increases, in other words no Brewster angle effects are observed as expected. Regardless, due to the limited range of θ where this occurs and the small differences in $\varepsilon(\lambda, \theta)$ between TE and TM polarizations, ε_H

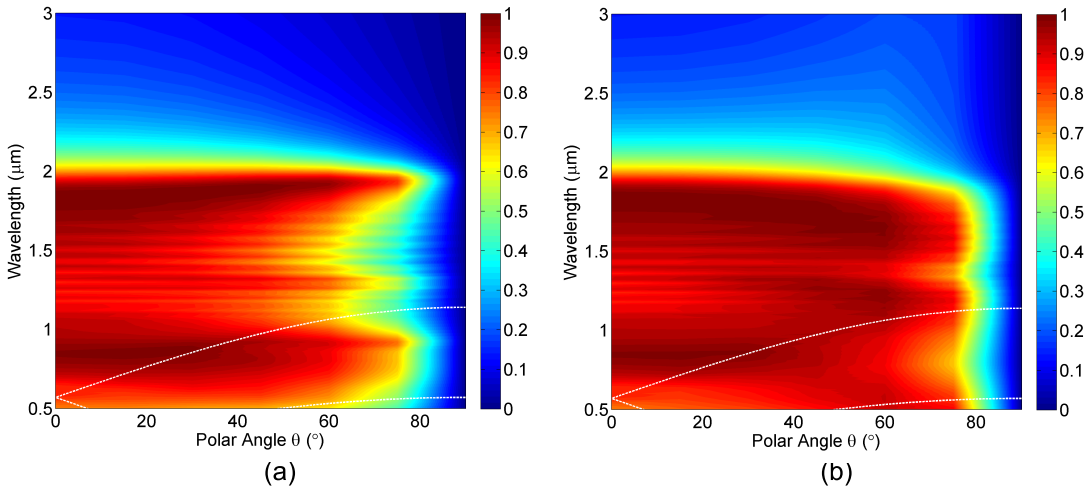

Figure 4-4: Contour plots of $\varepsilon(\lambda, \theta)$ for HfO_2-filled ARC 2D Ta PhC optimized for $\lambda_c = 2.00\,\mu m$ for (a) transverse electric (TE) and (b) transverse magnetic (TM) polarization. Evidently, the optimized HfO_2-filled ARC 2D Ta PhC possess omnidirectional, polarization insensitive, broadband wavelength selective emittance.

remains high (average of 0.86) at $\lambda < \lambda_c$. The optimized dielectric-filled MPhCs are thus essentially polarization insensitive.

4.3.2 Application: Thermophotovoltaic Systems

In this section, we illustrate the optimization of HfO_2-filled ARC 2D Ta PhCs as an emitter in an InGaAsSb TPV energy conversion system. The numerical model outlined in Section 3.2 was used to determine the FOM defined in Eq. (3.15). Again, we are mainly concerned on obtaining the highest η_{TPV} possible, thus $x = 0.9$ was used. Results of the optimization for $T = 1250\,K$ with $F = 0.99$ (achievable with $10\,cm \times 10\,cm$ flat plate geometry with emitter-TPV cell separation of $500\,\mu m$) are shown in Table 4.2. Note that when used at high T, a much smaller d is sufficient for optimum performance, and is thus easier to fabricate.

In TPV systems without a cold-side filter, the optimized HfO_2-filled ARC 2D Ta PhC enables up to 99% and 6% relative improvement in η_{TPV} over the greybody emitter ($\varepsilon = 0.9$) and the optimized unfilled 2D Ta PhC respectively. More importantly, up to 15% relative improvement is seen in J_{elec} with the optimized HfO_2-filled ARC 2D Ta PhC compared to the unfilled 2D Ta PhC

Table 4.2: Comparison of η_{TPV} and J_{elec} between a greybody emitter ($\varepsilon = 0.9$), optimized unfilled 2D Ta PhC ($r = 0.57\,\mu\text{m}$, $d = 4.00\,\mu\text{m}$, $a = 1.23\,\mu\text{m}$), and optimized HfO_2-filled ARC 2D Ta PhC ($r = 0.22\,\mu\text{m}$, $d = 0.75\,\mu\text{m}$, $a = 0.73\,\mu\text{m}$, $t = 146\,\text{nm}$) in InGaAsSb thermophotovoltaic (TPV) systems at $T = 1250\,\text{K}$ with $F = 0.99$ (achievable with $10\,\text{cm} \times 10\,\text{cm}$ flat plate geometry with emitter-TPV cell separation of $500\,\mu\text{m}$) with or without notable experimentally realized reflective spectral control devices.

Emitter	Filter	η_{TPV} (%)	J_{elec} (W/cm^2)
Greybody ($\varepsilon = 0.9$)	N/A	6.38	0.781
Optimized 2D Ta PhC	N/A	12.03	0.621
Optimized HfO_2-filled ARC 2D Ta PhC	N/A	12.71	0.713
Greybody ($\varepsilon = 0.9$)	10 layer Si/SiO_2	12.52	0.700
Optimized 2D Ta PhC	10 layer Si/SiO_2	18.31	0.568
Optimized HfO_2-filled ARC 2D Ta PhC	10 layer Si/SiO_2	19.34	0.646
Greybody ($\varepsilon = 0.9$)	Rugate Tandem Filter	23.44	0.726
Optimized 2D Ta PhC	Rugate Tandem Filter	23.68	0.588
Optimized HfO_2-filled ARC 2D Ta PhC	Rugate Tandem Filter	23.76	0.671

due to 26% relative improvement in ε_{H} at $\lambda < \lambda_{\text{c}}$. The improved J_{elec} is especially vital in many portable power applications where power generated per kilogram of weight (W/kg) is the primary figure of merit.

It is also interesting to compare the performance when coupled with notable experimentally realized reflective spectral control devices, namely the Rugate tandem filter [70] or the 10 layer Si/SiO_2 filter [72] that we discussed in Section 3.3.4. As can be seen, the improvement in J_{elec} is observed even when either filter is included. However, as better filters are used (e.g. Rugate tandem filter), the improvement in η_{TPV} from implementing MPhCs over a greybody becomes insignificant. Nevertheless, it is also important to note that Rugate tandem filters are extremely costly and difficult to fabricate, given the sheer number of layers (> 50 layers) and the specialty materials used (Sb_2Se_3, YF_3, and InPAs). When the much more practical 10 layer Si/SiO_2 filter stack is used instead, the 2D Ta PhC selective emitter enables $> 45\%$ relative improvement over the greybody emitter. Additionally, the performance of the optimized 2D Ta PhC selective emitter based TPV system is improved by $> 50\%$ when the simple 10 layer Si/SiO_2 filter is used. Ultimately, the optimum combination would depend on cost and design goals of a specific application.

4.3.3 Application: Selective Solar Absorption

High-performance selective absorbers are also indispensable for efficient absorption of solar energy in other energy conversion systems such as solar thermal [33, 46, 112], solar thermochemical [19], and solar thermophotovoltaics [15, 46, 63]. For such applications, it is important to ensure maximal absorption of solar irradiance, yet minimal re-emission. Hence, the key metrics for a solar absorber are the solar absorptance α_{s} and the thermal emittance ε_{t} defined as follows:

$$\alpha_{\mathrm{s}} = \frac{\int_0^{\infty} \mathrm{d}\lambda \int_0^{\theta_{\mathrm{c}}} \mathrm{d}\theta \int_0^{2\pi} \mathrm{d}\phi \, [\, \varepsilon(\lambda, \theta, \phi, T)\, S_{\mathrm{s}}(\lambda)\,]}{\int_0^{\infty} \mathrm{d}\lambda \int_0^{\theta_{\mathrm{c}}} \mathrm{d}\theta \int_0^{2\pi} \mathrm{d}\phi \, [S_{\mathrm{s}}(\lambda)\,]} \tag{4.1}$$

$$\varepsilon_{\mathrm{t}} = \frac{\int_0^{\infty} \mathrm{d}\lambda \int_0^{\frac{\pi}{2}} \mathrm{d}\theta \int_0^{2\pi} \mathrm{d}\phi \, [\, i_{\mathrm{BB}}(\lambda, T)\, \varepsilon(\lambda, \theta, \phi, T)\, \cos\theta \sin\theta\,]}{\int_0^{\infty} \mathrm{d}\lambda \int_0^{\frac{\pi}{2}} \mathrm{d}\theta \int_0^{2\pi} \mathrm{d}\phi \, [\, i_{\mathrm{BB}}(\lambda, T)\, \cos\theta \sin\theta\,]} \tag{4.2}$$

where $S_{\mathrm{s}}(\lambda)$ is the terrestrial solar spectral radiance (AM1.5D), and θ_{c} is the cutoff angle related to the solar concentration factor C and the solid angle subtended by the sun $\Omega_{\mathrm{s}} = 68.5 \times 10^{-6}$ sr:

$$\theta_{\mathrm{c}} = \sin^{-1}\left(\sqrt{\frac{C\Omega_{\mathrm{s}}}{\pi}}\right) \tag{4.3}$$

For common solar absorbers used in solar thermal applications at low ($< 450\,\mathrm{K}$) and intermediate temperatures ($< 700\,\mathrm{K}$), it is relatively easy to simultaneously achieve both high α_{s} and low ε_{t}, since blackbody emission in the IR regime is low at these temperatures, and that the thermal and solar spectra do not overlap significantly. In fact, many commercial solutions that can operate under atmospheric conditions exist [33]. However, higher operating temperatures (1000 K to 1500 K) may be necessary for higher efficiencies in certain applications, especially solar thermophotovoltaics [15, 46, 63]. At these temperatures, a sharp cutoff between the high α_{s} and low ε_{t} regions is crucial. In this respect, several promising designs based on 1D multilayer stacks [106], 2D adiabatic index matching PhCs [17, 113], and metamaterials [114] have been reported. However, the dielectric-filled ARC 2D MPhC design holds several other advantages: it is easily optimized for virtually any operating condition; fabrication is simple and scalable; demonstrated thermal stability under vacuum conditions. In addition, we have implemented accurate high temperature

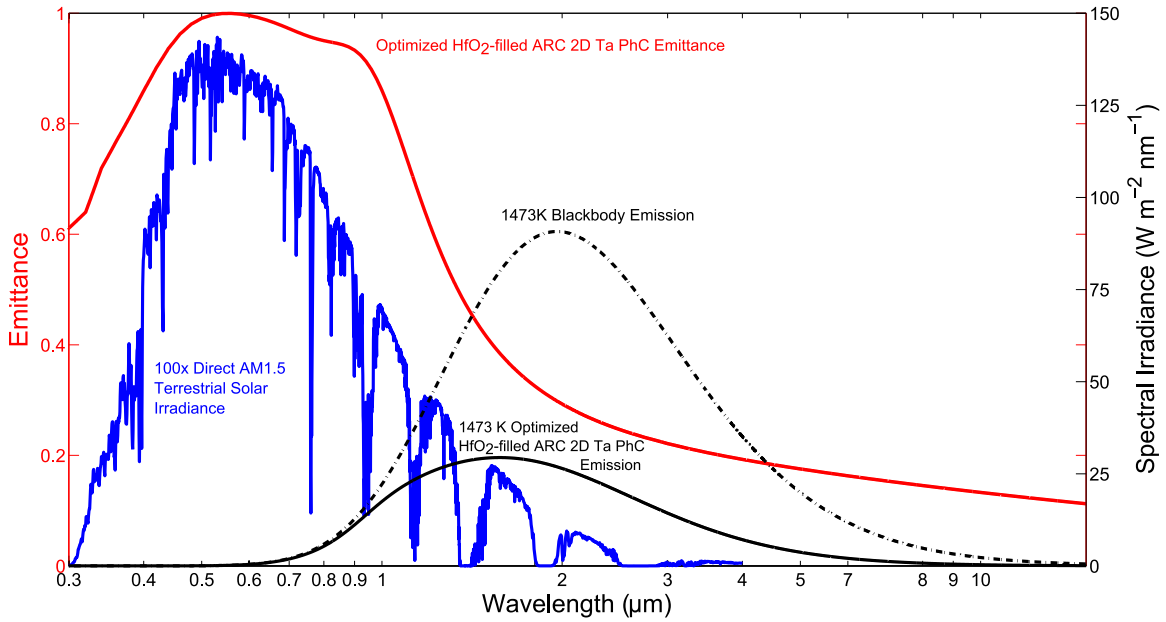

Figure 4-5: HfO_2-filled ARC 2D Ta PhC ($r = 73.6\,\text{nm}$, $d = 1.00\,\mu\text{m}$, $a = 248\,\text{nm}$, $t = 4.8\,\text{nm}$) optimized for optimum selective solar absorption. 84% of incident solar energy is absorbed, while emission is limited to 27% of the blackbody.

material properties in our simulations, which to our knowledge have not been considered in all prior investigations.

The optimum λ_c depends on the operating condition, namely C, and T, which is also related to the rate of heat extraction from the absorber. Here, we are more interested in a design for general operating conditions, and hence we have used the following FOM in the optimization routines:

$$\text{FOM} = \alpha_s \times (1 - \varepsilon_t) \tag{4.4}$$

For $C < 5000$ (typical concentrated solar power systems have $C = 30$–3000), $\theta_c < 20°$. Since both the unfilled and the dielectric-filled 2D MPhC have emission profiles that are essentially unchanged up to $\theta = 30°$, α_s can be approximated with $\varepsilon(\lambda, 0°, 0°, T)$ in Eq. (4.1). Using this, we obtained an optimized unfilled 2D Ta PhC capable of $\alpha_s/\varepsilon_t \approx 0.80/0.27$, and an optimized HfO_2-filled ARC 2D Ta PhC capable of $\alpha_s/\varepsilon_t \approx 0.84/0.27$ (illustrated in Fig. 4-5) for $1000\,\text{K} < T < 1500\,\text{K}$, where a slight improvement is seen in the dielectric-filled structure due to larger bandwidth of high absorptance.

In an appropriately designed system with modest $C = 500$, 68% of incoming solar energy can be transferred to a heat engine situated behind the selective absorber. This outperforms the blackbody absorber by 70%. Thus, the 2D MPhCs enable operation at higher equilibrium temperatures even with low C's.

4.4 Conclusions

In summary, we have demonstrated optimized designs of dielectric-filled ARC 2D MPhCs for broadband wavelength selective emission. Using non-linear global optimization methods, optimized HfO_2-filled ARC 2D MPhC designs exhibiting up to 26% improvement in ε_{H} at $\lambda < \lambda_{\mathrm{c}}$ over the unfilled 2D MPhC have been demonstrated. The optimized designs possess high ε_{H} of 0.86 at $\lambda < \lambda_{\mathrm{c}}$ and low ε_{H} of 0.12 at $\lambda > \lambda_{\mathrm{c}}$ over all polar angles and polarizations at $T < 100\,^{\circ}\mathrm{C}$, whereby λ_{c} can easily be shifted and optimized via non-linear global optimization tools.

At high temperatures ($T \sim 1250\,\mathrm{K}$), ε_{H} at $\lambda > \lambda_{\mathrm{c}}$ increases to 0.26 due to primarily the reduction in DC-conductivity, hence making the metal more lossy at long wavelengths. This limitation is inherent to all metal based selective emitters, and is thus unavoidable. Regardless, the dielectric-filled ARC 2D MPhC design drastically reduces diffraction losses at $\lambda < \lambda_{\mathrm{c}}$ compared to the unfilled 2D MPhC. This translates into $\sim 15\%$ improvement in generated electrical power density for TPV systems, which is vital in many portable power applications. These designs also provide the platform necessary for many applications, ranging from solar absorbers for solar thermal applications, to near- to mid-IR radiation sources for IR spectroscopy.

Chapter 5

Photonic Crystal Enhanced Silicon Cell Based Thermophotovoltaic Systems

As discussed in Chapter 3, PhC enhanced TPV systems hold great promise for efficient solid-state energy generation. However, detailed TPV experimental studies that quantify the improvements seen with PhCs, as well as understanding of parasitic losses, have been lacking. In this chapter, we report the design, optimization, and experimental results of a large area silicon (Si) cell based TPV system. We further show that the results validate the numerical model outlined in Section 3.2. Furthermore, additional insights on experimental parasitic losses are presented, of which would aid towards future development of highly efficient large scale PhC enhanced TPV systems.

5.1 Introduction

In Chapter 3, we have shown that η_{TPV} of 25% can be achieved using experimentally demonstrated optimized 2D Ta PhC selective emitter coupled with an optimized cold-side tandem filter on state-of-the-art InGaAs TPV cells at realistic emitter $T = 1320\,\mathrm{K}$ and $F = 0.99$ ($10\,\mathrm{cm} \times 10\,\mathrm{cm}$ flat

plate geometry with $s = 500\,\mu\text{m}$). This is extremely promising, especially in applications whereby solid-state energy conversion is a major advantage compared to traditional mechanical methods of generation, for instance as a stable energy generator in deep space missions [14, 42, 59, 60]. Compared to TPV, other competing modes of solid-state energy generation, namely thermoelectrics and thermionics, have much lower efficiencies of $< 15\%$ [115, 116]. However, as discussed in Section 3.3.6, detailed TPV experimental studies that accurately determine performance metrics, as well as quantify potential improvements using PhCs, have been lacking.

In this chapter, we report on an experimental large area TPV test setup that enables accurate measurements of η_{TPV} for any emitter–filter–TPV cell combination of interest. Here, we specifically consider Si PV cells as they are cheap and commercially available in large sizes, and the technology is significantly more mature and closer to theoretical limits compared to low bandgap TPV cells. Due to the unique challenges involved in designing efficient Si-TPV systems, very few experimental results have been reported: Swanson reported TPV efficiencies of 10% (does not include cavity losses) with specially designed Si cells and a blackbody cavity emitter at $T = 2350\,\text{K}$ [95]; Bitnar *et al.* reported overall fuel-to-electricity efficiencies of 3.96% and $J_{\text{elec}} = 0.104\,\text{W}\,\text{cm}^{-2}$ using a ytterbia (Yb_2O_3) rare-earth selective emitter at $T > 1700\,\text{K}$ [99]. However, in both of these investigations, direct measurements of η_{TPV} were not performed. Additionally, lower T's ($< 1500\,\text{K}$) are more practical given the difficulties of engineering selective emitters that will remain stable over long time scales. In this investigation, we propose a combination of optimized 2D Ta PhC selective emitters and 1D PhC based cold-side dielectric filters that will enable reasonable performance at lower T's. The experimental setup used to validate the numerical models as well as the measurements obtained will be discussed, followed with our concluding remarks.

5.2 Design and Optimization

5.2.1 Emitter

The primary challenge of designing Si cell based TPV systems for a lower $T = 1500\,\text{K}$ lies in the small fraction of energy that is potentially convertible due to Si possessing a high $E_{\text{g}} = 1.12\,\text{eV}$.

For a greybody with $\varepsilon = 0.9$, only 2.8% of the radiative energy is convertible. Efficient spectral control is thus a necessity.

The recent success in fabricating 2D Ta PhCs allows investigation into designing broadband selective emitters with much lower λ_c ($\sim$ 1-1.5 μm) as compared to using W. This is due to the fact that Ta's transition to high emittance occurs below 1 μm as shown in Fig. 3-3. Thus, optimized designs for 2D Ta PhCs can easily be obtained using the formalism outlined in Section 3.2.1 and 3.2.2. For optimization purposes, we used Si cell data measured by the University of New South Wales (UNSW) solar cell research group, which currently holds the highest solar cell efficiency record achieved for single crystal Si [91,101,117]. Using this, optimized designs of both the unfilled 2D Ta PhC and the HfO_2-filled ARC 2D Ta PhC were obtained; both designs show excellent match with the Si cell EQE as shown in Fig. 5-1. The figure also shows the emittance of flat Ta with an optimized 85 nm coating of HfO_2 (optimized HfO_2 ARC flat Ta), which is an easily fabricated alternative. η_{TPV}, η_{cell}, $\eta_{\text{cav-spec}}$, and J_{elec} for all three selective emitters in a Si-TPV system with T = 1500 K and $F = 0.99$ are shown in Table 5.1.

5.2.2 Cold-side Filter

As shown in Table 5.1, the optimized 2D Ta PhC selective emitter provides the highest $\eta_{\text{TPV}} \simeq$ 4.12%, which is an improvement of 113% over the greybody ($\varepsilon = 0.9$). Regardless, the spectral efficiency is still too low due to the relatively low temperatures involved. To further boost efficiencies,

Table 5.1: Comparison of η_{TPV}, η_{cell}, $\eta_{\text{cav-spec}}$, and J_{elec} between a greybody emitter ($\varepsilon = 0.9$), optimized HfO_2 ARC flat Ta (85nm of HfO_2 on top of flat Ta), optimized unfilled 2D Ta PhC (r = 0.28 µm, d = 2.20 µm, a = 0.61 µm), and optimized HfO_2-filled ARC 2D Ta PhC (r = 0.09 µm, d = 1.00 µm, a = 0.35 µm, t = 83 nm) in Si-TPV systems at T = 1500 K with $F = 0.99$ (achievable with 10 cm × 10 cm flat plate geometry with emitter-TPV cell separation of 500 µm).

Emitter	$\eta_{\text{cav-spec}}$ (%)	η_{cell} (%)	η_{TPV} (%)	J_{elec} (W/cm^2)
Greybody ($\varepsilon = 0.9$)	5.19	37.21	1.93	0.238
Optimized HfO_2 ARC Flat Ta	8.95	38.94	3.48	0.173
Optimized 2D Ta PhC	10.99	37.47	4.12	0.210
Optimized HfO_2-filled ARC 2D Ta PhC	10.42	37.16	3.87	0.237

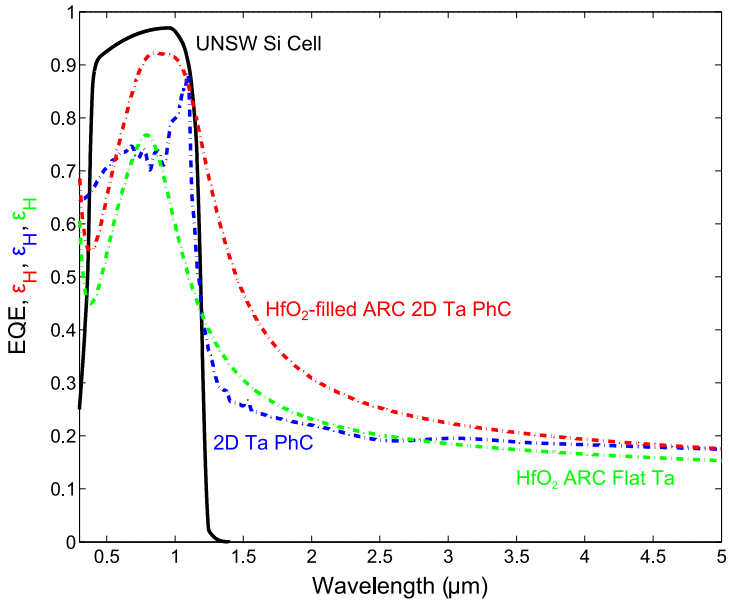

Figure 5-1: Spectral hemispherical emittance of both the optimized unfilled ($r = 0.28\,\mu\text{m}$, $d = 2.20\,\mu\text{m}$, $a = 0.61\,\mu\text{m}$) and HfO_2-filled ARC 2D Ta PhC ($r = 0.09\,\mu\text{m}$, $d = 1.00\,\mu\text{m}$, $a = 0.35\,\mu\text{m}$, $t = 83\,\text{nm}$) show excellent match with the EQE of University of New South Wales's (UNSW) Si solar cells. A simple optimized 85 nm coating of HfO_2 on top of flat Ta (HfO_2 ARC Flat Ta) also performs reasonably well.

a cold-side spectrally selective filter can be added to the front of the Si solar cell in order to achieve reasonable η_{TPV}'s. In this investigation, we consider a simple, experimentally realizable solution based on a variant of the quarter-wave stack 1D PhC: the exponentially chirped distributed Bragg reflector (DBR) [118]. It is essentially a periodic quarter-wave stack with an exponentially varying period, such that the effective stop band is broadened. The period of the l-th stack is given by:

$$a_l = a_0 \exp(lB) \tag{5.1}$$

where a_0 is the period of the first stack, and B is the exponential chirp factor given by:

$$B = \frac{1}{l} \ln\left(\frac{1+b}{1-b}\right) \tag{5.2}$$

where b is defined as the relative range, such that:

$$a_l = a_0 \frac{1+b}{1-b} \tag{5.3}$$

The first stack is chosen such that it corresponds to a standard quarter-wave stack:

$$a_0 = \frac{\lambda_c}{4n_1} + \frac{\lambda_c}{4n_2} \tag{5.4}$$

where λ_c is related to the cutoff wavelength of the filter, and n_1 and n_2 are respectively the refractive index of the first and second dielectric material. As per the standard quarter-wave stack, the larger the refractive index contrast, the better the performance of the filter. From Eqs. (5.1) and (5.4), we can see that only two parameters (λ_c and b) define the exponentially chirped DBR, and thus the optical properties. Again, we used NLOpt to determine the optimum values for maximum FOM defined as follows:

$$\text{FOM} = x\eta_{\text{spec}} + (1-x)\eta_{\text{emit}} \tag{5.5}$$

where η_{spec} and η_{emit} are respectively the spectral efficiency and emission efficiency given by:

$$\eta_{\text{spec}} = \frac{\int_0^{\lambda_c} i_{\text{BB}}(\lambda, T)\, \varepsilon_{\text{H}}(\lambda)\, R_{\text{H}}(\lambda)\, \mathrm{d}\lambda}{\int_0^{\infty} i_{\text{BB}}(\lambda, T)\, \varepsilon_{\text{H}}(\lambda)\, R_{\text{H}}(\lambda)\, \mathrm{d}\lambda} \tag{5.6}$$

$$\eta_{\text{emit}} = \frac{\int_0^{\lambda_c} i_{\text{BB}}(\lambda, T)\, \varepsilon_{\text{H}}(\lambda)\, R_{\text{H}}(\lambda)\, \mathrm{d}\lambda}{\int_0^{\lambda_c} i_{\text{BB}}(\lambda, T)\, \mathrm{d}\lambda} \tag{5.7}$$

where $\varepsilon_{\text{H}}(\lambda)$ is the spectral hemispherical emittance of the selective emitter and $R_{\text{H}}(\lambda)$ is the spectral hemispherical reflectance of the filter. η_{spec} captures the fraction of convertible energy, while η_{emit} is the ratio of convertible power of the emitter–filter combination to that of a blackbody. $\eta_{\text{spec}} = \eta_{\text{emit}} = 1$ represents the limit of performance desired. In practice, the weighting factor x can be tailored to give either more emphasis to efficiency or power density.

In this investigation, we choose tantalum pentoxide (Ta_2O_5) and silicon dioxide (SiO_2) with n of approximately 2.1 and 1.5 respectively; they are both highly transparent in the wavelength range $0.25\,\mu\text{m} < \lambda < 5.0\,\mu\text{m}$, and are industry standard optical coatings [111, 119]. To ensure practical

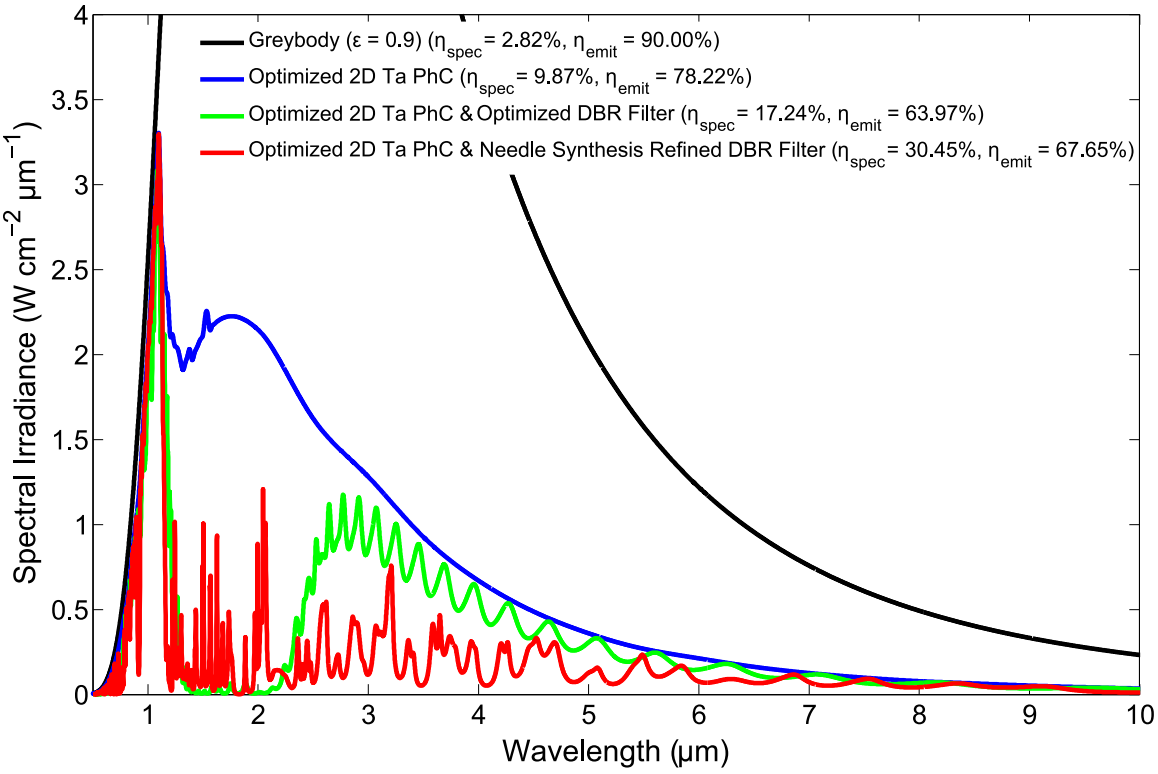

Figure 5-2: Effective spectral irradiance incident on PV cell for various selective emitter and cold-side filter combinations of interest at $T = 1500\,\mathrm{K}$.

realization, we consider only 30 bilayers for the filter design. Using NLOpt with $x = 0.15$, the optimum DBR filter was determined to have $\lambda_c = 1.397\,\mu\mathrm{m}$ and $b = 0.211$. When combined with the optimized 2D Ta PhC, this filter enables an improvement of approximately 511% and 75% in η_{spec} compared to respectively the greybody ($\varepsilon = 0.9$) and optimized 2D Ta PhC based TPV system without the filter, albeit at a slightly reduced η_{emit}. The improvement is clearly seen in Figure 5-2, whereby the effective spectral irradiance incident on the PV cell for $1.1\,\mu\mathrm{m} < \lambda < 2.3\,\mu\mathrm{m}$ is mostly suppressed, i.e. reflected back to the emitter.

The optimized exponentially chirped DBR filter can further be improved via the *needle synthesis* optimization method [120]. This algorithm is, in essence, a perturbative method. In this case, the original optimized exponentially chirped DBR filter is repeatedly modified via the addition or subtraction of a thin layer of material ($\approx 10\,\mathrm{nm}$ to $20\,\mathrm{nm}$) at a location which results in the greatest

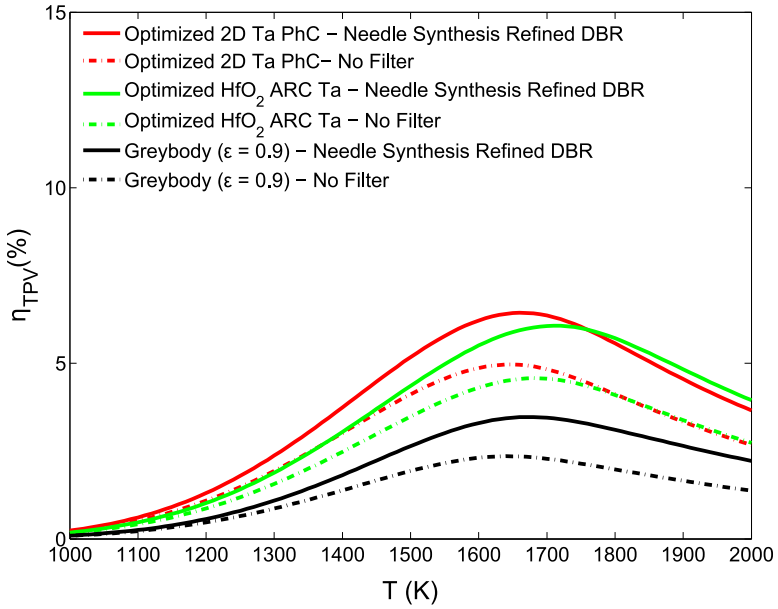

Figure 5-3: η_{TPV} as a function of T for various selective emitter and cold-side filter combinations of interest in TPV systems with $F = 0.99$.

improvement in the FOM. The process is repeated until the FOM ceases to improve. By applying this on the optimized exponentially chirped DBR filter, a further 77% improvement in η_{spec} is seen when coupled with the optimized 2D Ta PhC selective emitter. As can be seen in Fig. 5-2, the *needle synthesis* method improves on the original optimized exponentially chirped DBR filter by further reducing effective spectral irradiance incident on the PV cell for $\lambda > 2.3\,\mu\text{m}$, albeit at a smaller penalty of allowing a small number of photons through for $1.1\,\mu\text{m} < \lambda < 2.3\,\mu\text{m}$.

5.2.3 TPV System

Using the numerical model described in Section 3.2.1, estimates of η_{TPV} using UNSW Si PV cells and various emitter–filter combinations in $F = 0.99$ TPV systems were obtained; the results are illustrated in Fig. 5-3. Similar trends in η_{TPV} reported in Section 3.3 for low bandgap TPV cells are seen; as T increases, η_{TPV} decreases primarily due to series resistance under high current injection, which is $\gtrsim 5$ times of that under standard AM1.5 solar irradiance. Thus, specially designed Si cells for low solar concentrations ($C = 5$–20) would be more suitable for TPV applications.

For the greybody ($\varepsilon = 0.9$), $\eta_{\text{TPV, max}} = 2.35\%$ at $T = 1640\,\text{K}$. By replacing the greybody with

Table 5.2: Comparison of η_{TPV} and J_{elec} between a greybody emitter ($\varepsilon = 0.9$), flat Ta, optimized HfO_2 ARC flat Ta (85nm of HfO_2 on top of flat Ta), and optimized unfilled 2D Ta PhC ($r = 0.28\,\mu\text{m}$, $d = 2.20\,\mu\text{m}$, $a = 0.61\,\mu\text{m}$) at $T = 1500\,\text{K}$ with or without the needle synthesis refined DBR filter in $F = 0.99$ Si-TPV systems.

Emitter	Filter	η_{TPV} (%)	J_{elec} (W/cm^2)
Greybody ($\varepsilon = 0.9$)	N/A	1.93	0.24
Flat Ta	N/A	2.17	0.09
Optimized HfO_2 ARC Ta	N/A	3.48	0.17
Optimized 2D Ta PhC	N/A	4.12	0.21
Greybody ($\varepsilon = 0.9$)	Needle Synthesis Refined DBR	2.64	0.22
Flat Ta	Needle Synthesis Refined DBR	2.63	0.08
Optimized HfO_2 ARC Ta	Needle Synthesis Refined DBR	4.36	0.15
Optimized 2D Ta PhC	Needle Synthesis Refined DBR	5.17	0.19

the optimized HfO_2 ARC Ta or optimized 2D Ta PhC selective emitter, $\eta_{\text{TPV, max}}$ can be increased to 4.58% (at $T = 1680\,\text{K}$) and 4.97% (at $T = 1650\,\text{K}$) respectively. The highest $\eta_{\text{TPV, max}}$ of 6.44% (at $T = 1660\,\text{K}$) is achieved with the optimized 2D Ta PhC and needle synthesis refined DBR filter combination. In this investigation, the target operating T is 1500 K; η_{TPV} and J_{elec} at $T = 1500\,\text{K}$ for various emitter and cold-side filter combinations of interest are shown in Table 5.2.

5.3 Experimental Method and Results

5.3.1 Solar Cell Packaging

In this investigation, we used state-of-the-art Sunpower solar cells, which are to-date the most efficient commercially available Si PV cells boasting a solar-to-electricity efficiency of 25.6% [91]. One of the key reasons for superior efficiencies of Sunpower Si cells is the back-contacted design, i.e. all electrical connections are located at the back of the solar cell, thus eliminating shading losses that plague conventional front-contacted designs. For the particular cell we were using, 6 terminals (3 +ve and 3 -ve) of the size of 7.5 mm × 7.5 mm are provided for electrical connections. All other areas need to be free of electrical connections to ensure no electrical shorts exists. Concurrently, for efficient TPV energy conversion, it is important to ensure that the Sunpower Si cell is in good thermal contact with the heat sink.

In order to achieve both precisely placed electrical connections and excellent thermal path elsewhere, the Sunpower Si cell is mounted on top of a Bergquist HPL Thermal Clad. It is, in essence, similar to a printed circuit board, of which electrical connections are provided by copper (Cu) foils, while the remaining area is covered with a thin layer (38 µm thickness) of high thermal conductivity ($\kappa = 3.0\,\mathrm{W\,m^{-1}\,K^{-1}}$) dielectric material, all on top of a 1 mm thick Cu substrate. To adhere the Sunpower Si cell to the Bergquist HPL Thermal Clad, the following procedure was found to function best:

1. A layer of 3M 8805 thermally conductive ($\kappa = 0.60\,\mathrm{W\,m^{-1}\,K^{-1}}$) electrically insulating pressure sensitive tape (125 µm thick) is placed on top of the Bergquist HPL Thermal Clad at areas requiring electrical insulation.

2. Using a thin stencil (125 µm thick), a small amount of electrically conducting silver-filled grease (AREMCO Heat-Away 641-EV) is applied on electrical contacts of the Bergquist HPL Thermal Clad.

3. Using a precisely fabricated mechanical aligning system, the Sunpower Si cell is slowly lowered until contact is made with the thermal adhesive and electrical grease which have been applied on top of the Bergquist HPL Thermal Clad in previous steps.

4. The entire Sunpower Si cell - Bergquist HPL Thermal Clad device is placed on a hot press. To protect the surface of the Sunpower Si cell, a clean piece of glass is placed in between before initiating the hot press. The hot press is set to $T = 65\,^{\circ}\mathrm{C}$ at a pressure of 5000 kPa; this is maintained for 5 minutes. This step is vital to ensure strong bonding, as well as minimal trapped air between 3M's 8805 thermal tape and the Sunpower Si cell..

A Sunpower Si cell packaged on the Bergquist HPL Thermal Clad is shown in Fig. 5-4. Since the Bergquist HPL Thermal Clad is not perfectly flat, it was bonded onto a thicker (10 mm) aluminum (Al) substrate with Epotek's H74 thermally conductive epoxy ($\kappa = 1.25\,\mathrm{W\,m^{-1}\,K^{-1}}$). A thin layer of thermal grease (AREMCO Heat-Away 641-EV, $\kappa = 5.58\,\mathrm{W\,m^{-1}\,K^{-1}}$) was then applied between

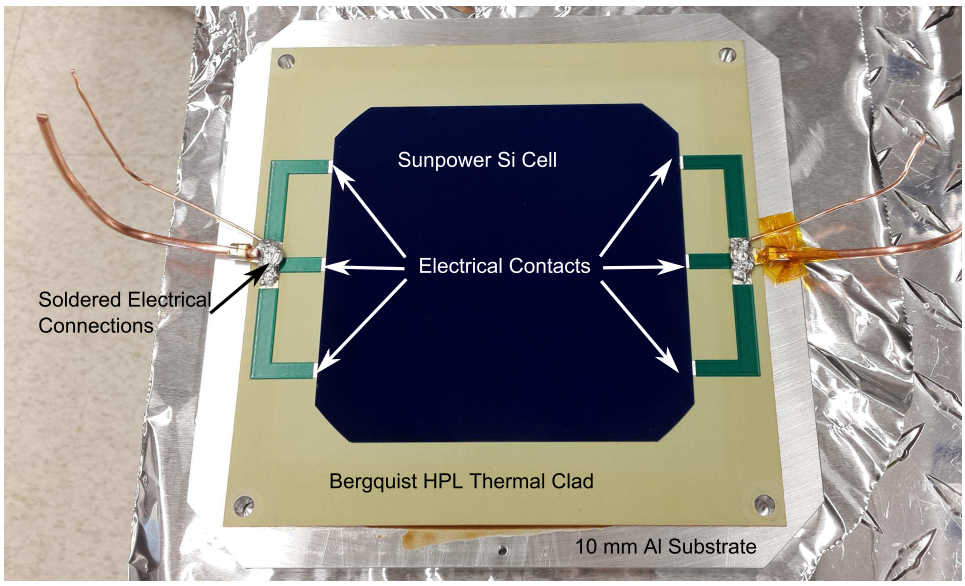

Figure 5-4: Sunpower Si cell packaged on Bergquist HPL Thermal Clad.

the Al substrate and the heat sink. The bolting force coupled with the thicker and thus stiffer Al substrate ensures good thermal contact with the heat sink. Note that standard epoxies do not work well in adhering the Sunpower Si cell to the Bergquist HPL Thermal Clad due to the precision required in ensuring accurate placement and isolation of electrical contacts from thermally conductive electrically insulating areas.

5.3.2 Thermophotovoltaic Cavity Design

The key parameters that we desire to measure are η_{TPV} and P_{elec}. In order to measure η_{TPV} as defined in Eq. (3.11), a precise calorimetric approach to accurately measure the net radiant power emitted ($P_{\mathrm{em}} - P_{\mathrm{re}}$) is necessary. This was achieved in the experimental setup shown in Fig. 5-5, which was specifically designed to accurately account for all energy transfers in the system; input electrical power P_{in} to the heater (100 mm diameter HeatWave Labs 1200 °C UHV Heater) and the electrical power output P_{elec} of the PV cell were measured simply using accurate voltage and current meters (Fluke 289 True RMS Meter, Fluke i310s Current Clamp); measurement of the parasitic conductive heat loss P_{cond} was performed by monitoring the temperature difference of the Al posts using two high-accuracy 100Ω Class A DIN Platinum 3-wire resistance temperature

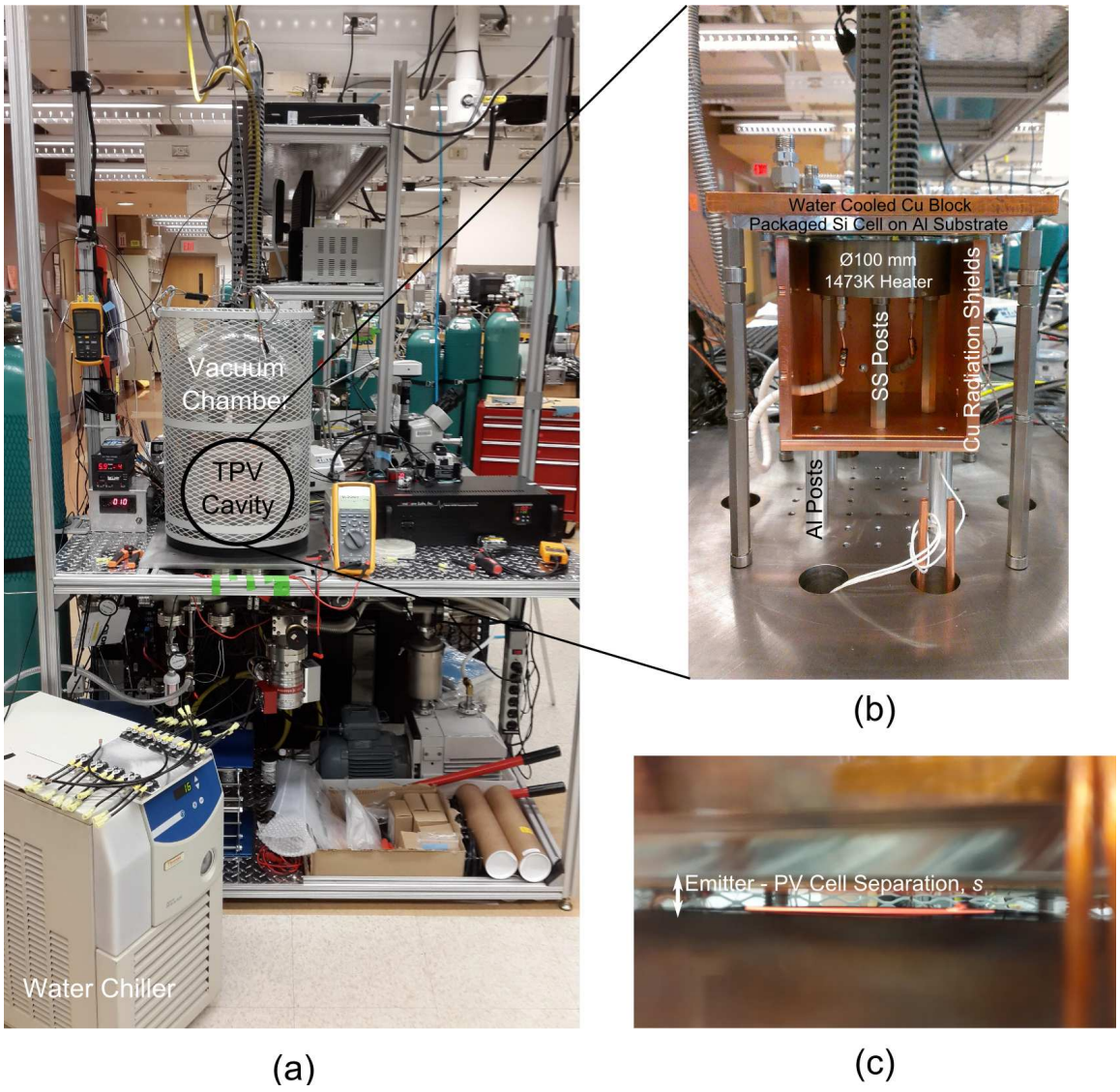

Figure 5-5: (a) Entire TPV efficiency measurement setup. (b) Close-up view of TPV cavity design. SS denotes stainless steel. (c) Close-up view of glowing emitter during operation at 1473 K.

detectors (RTD); parasitic radiative heat loss of the Cu radiation shields were neglected since they are at much lower temperatures of $\approx 500\,\mathrm{K}$, thus contributing $\lesssim 3\%$ of the overall energy balance (in fact, ignoring this results in a more conservative measurement of η_{TPV}, albeit at an acceptably small error). η_{TPV} is then given by:

$$\begin{aligned}\eta_{\mathrm{TPV}} &= \frac{P_{\mathrm{elec}}}{P_{\mathrm{em}} - P_{\mathrm{re}}} \\ &= \frac{P_{\mathrm{elec}}}{P_{\mathrm{in}} - P_{\mathrm{cond}}}\end{aligned} \tag{5.8}$$

5.3.3 Thermophotovoltaic Efficiency Measurements

In this investigation, we are focused on obtaining experimental results using just the optimized HfO_2 ARC flat Ta emitter. This serves as a vital preliminary experimental investigation, and more importantly allows us to verify the numerical models presented in Section 3.2, before deciding to undertake significant efforts toward realizing large area 2D Ta PhCs, and fabrication and implementation of the needle synthesis refined DBR filter, both of which require efforts beyond the scope of this publication.

Stock flat Ta sputtering targets of $r = 50\,\mathrm{mm}$ and $t = 2.5\,\mathrm{mm}$ were sourced from Shanghai Jiangxi Metals Co. The flat Ta wafer was then polished to a mean surface roughness of $\approx 5.94\,\text{Å}$ and surface flatness of $\approx 5.0\,\mu\mathrm{m}$. The polished Ta wafer was then deposited with 85 nm of HfO_2 using ALD (Cambridge Nanotech Savannah 200). t and n of the HfO_2 coating was verified using an ellipsometer (J. A. Woollam Co. M2000). In addition, ε measured indirectly using the FTIR (Nexus 870) reflectance accessory (PIKE Technologies VeeMAX II) with a known standard Al mirror (Thorlabs) was found to match extremely well with numerical predictions.

Accurate measurements of the top surface temperature of the emitter are of extreme importance, without which inhibits comparison of experimental data to numerical models. Here, we spot welded type K thermocouples on top of the emitter. Since the area of the weld covers $\lesssim 0.01\%$ of the total area of the emitter, it is safe to assume that the perturbation is small, and thus this method is a reasonably accurate measurement of the top surface temperature. Indeed, the experimentally

measured P_{elec} shown in Fig. 5-6(b) with emitter-PV cell separation $s = 2.0\,\text{mm}$ shows excellent agreement with simulations. Highest recorded $P_{\text{elec}} = 7.6\,\text{W}$ and $\eta_{\text{TPV}} = 1.18\%$ was obtained at $T = 1380\,\text{K}$; at this point the heater internals are at $T = 1500\,\text{K}$, which is the heater's maximum temperature rating, and thus higher T's are unattainable with this setup.

However, note that measured η_{TPV}'s are $\approx 50\%$ of numerical model predictions denoted by *Ideal Setup* in Fig. 5-6(a). In the *Ideal Setup* numerical simulations, the heater is assumed to only comprise of the selective emitter with $r = 50\,\text{mm}$. However, as can be seen in the inset of Fig. 5-6(a), there are heat shields that contribute to the effective size of the heater such that the measured $r = 59\,\text{mm}$, and more significantly 28% of the effective area is covered by the heat shields. According to HeatWave Labs, the inner and outer heat shields comprise of inconel and stainless steel respectively. In fact, by including the area of the heat shields in simulations assuming reasonable parameters of $\varepsilon = 0.9$ and $T \approx 250\,\text{K}$ cooler than the selective emitter top surface for the heat shields, we obtained simulation results that match extremely well with the experimental results as indicated by *Current Setup* numerical predictions in Fig. 5-6. As seen in Fig. 5-6(b), the heat shields contribute no P_{elec} due to lower T, but results in an increase in net radiative power absorbed by the PV cell by $\approx 80\%$ compared to just the selective emitter alone.

5.4 Conclusions

In summary, we have investigated Si PV cells for TPV applications as they are cheap and commercially available in large sizes, and the technology is significantly more mature and closer to theoretical limits compared to low bandgap TPV cells. Using global non-linear optimization tools, we have demonstrated theoretically a maximum η_{TPV} of 6.4% and $J_{\text{elec}} = 0.4\,\text{W}\,\text{cm}^{-2}$ at $T = 1660\,\text{K}$ when implementing both the optimized 2D Ta PhC selective emitter, and the needle synthesis refined DBR cold-side selective filter; the simulations incorporates Si cell data measured by the UNSW, which currently holds the highest solar cell efficiency record achieved for single crystal Si.

In addition, we have developed an experimental large area TPV test setup that enables accurate measurement of η_{TPV} for any emitter-filter-TPV cell combination of interest. Our experimental

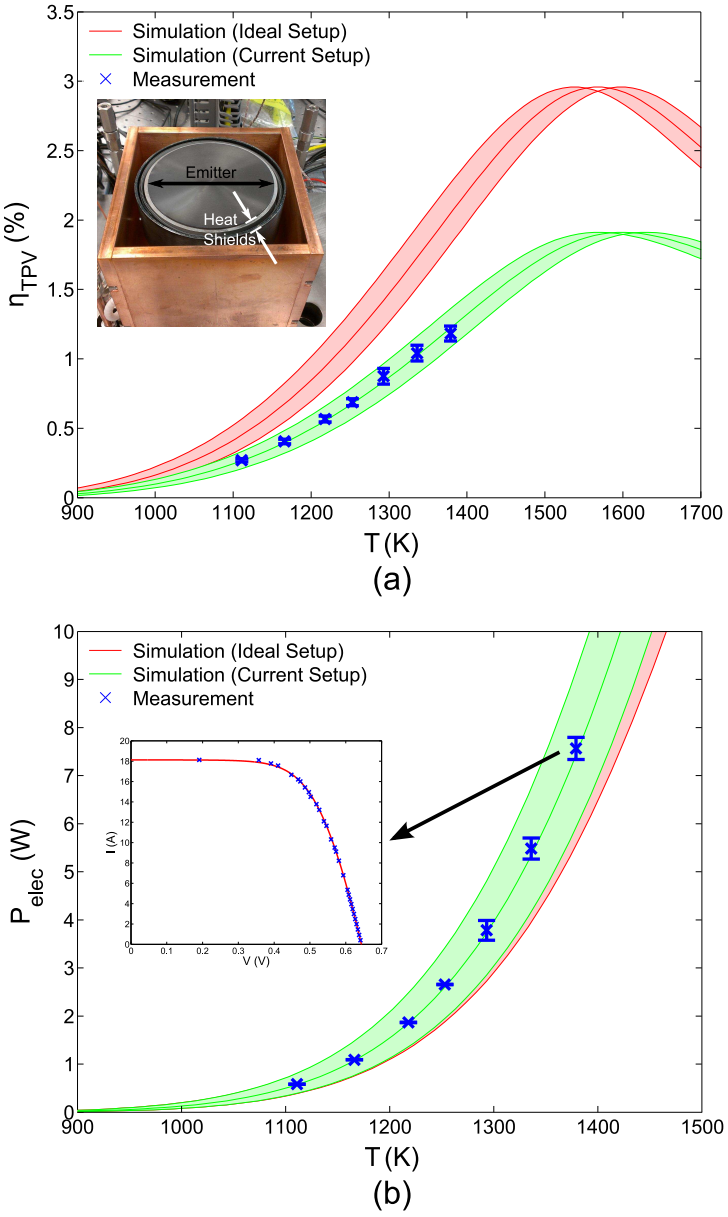

Figure 5-6: Measured (a) η_{TPV} and (b) P_{elec} as a function of T using Sunpower Si cell with optimized 85 nm thick HfO_2 ARC coating on flat Ta with emitter-PV cell separation $s = 2.0\,\mathrm{mm}$. The simulation results are represented as bands to account for an arbitrary temperature uncertainty of $\pm\,30\,\mathrm{K}$. Inset of (a) shows top view of 100 mm diameter HeatWave Labs 1200 °C UHV Heater. The heat shields are estimated to be $\approx 250\,\mathrm{K}$ cooler than the top surface of the emitter; this resulted in significant parasitic radiative heat loss absorbed by the PV cell, which negatively affects η_{TPV} as shown by the green curve (the 'Current Setup'). The 'Ideal Setup' simulations are performed without effects of the heat shields, i.e. only radiation from the emitter is considered. Inset of (b) shows the Sunpower Si cell IV curve measurement at the heater's maximum temperature rating.

setup achieved a maximum $P_{\text{elec}} = 7.6\,\text{W}$ and $\eta_{\text{TPV}} = 1.18\%$ at $T = 1380\,\text{K}$ using standard wafer size back-contacted Sunpower solar cells. The experimental results agree extremely well with numerical predictions, thus validating the models described in Section 3.2.

Chapter 6

Conclusions

In this thesis, we have explored the design, optimization, and experimental realization of PhCs for high temperature applications. Specifically, we have selected an architecture based on 2D PhC slabs fabricated from refractory metals by virtue of its simple design, yet promising performance and potential stability over long operating time scales. The theory, fabrication, and experimental characterization at room and high temperatures of this particular 2D MPhC slab selective emitter/absorber have been explored in detail in Chapter 2. In addition, the 2D MPhC slab has been shown to be extremely robust to fabrication disorders. Nevertheless, extended operation over longer time scales ($>$ 10000 hours) has not been demonstrated experimentally. This is a vital practical requirement and should be addressed in future research.

In Chapter 3, we have quantitatively determined the improvements seen with 2D MPhC selective emitters/absorbers in a particular high temperature application, namely TPV energy conversion. System level numerical models have been developed to estimate the enhancement to present TPV energy conversion systems. By combining an optimized 2D Ta PhC selective emitter with an optimized cold-side tandem filter, a TPV energy conversion system with radiant heat-to-electricity efficiency of 25% and power density of $0.68\,\mathrm{W\,cm^{-2}}$ can be achieved using experimentally demonstrated InGaAs TPV cells at realistic emitter temperature of 1320 K. Interestingly, a performance approaching $\sim$ 80% of this can be achieved with the simpler and more practical 1D PhC Si/SiO_2

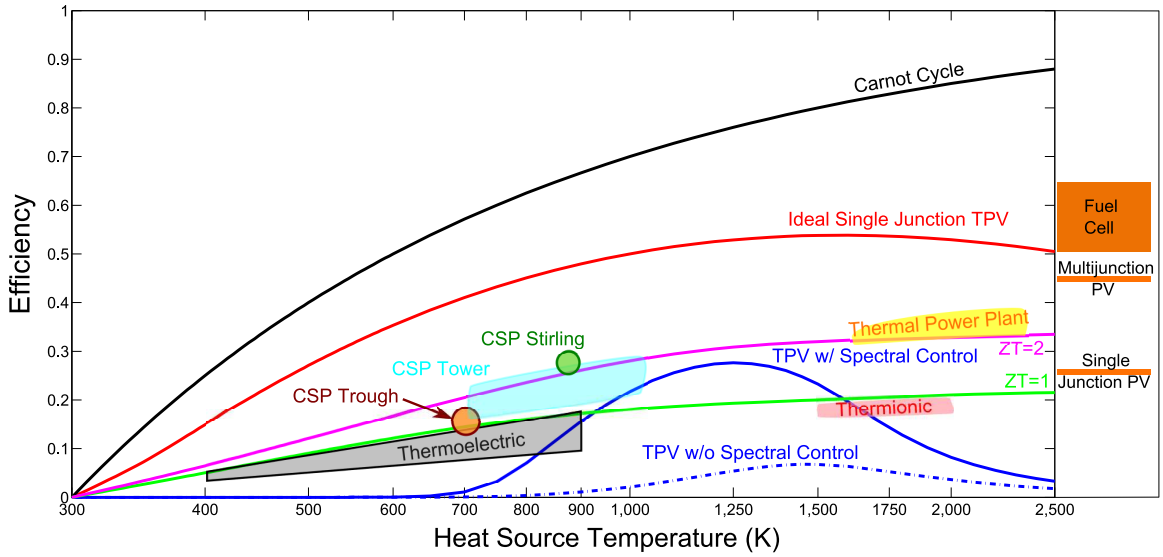

Figure 6-1: Power generation efficiency of different energy conversion technologies as a function of hot side temperature (adapted from Ref. 116). CSP denotes concentrated solar power, while ZT denotes figure of merit of thermoelectric devices. Theoretical limits of thermoelectric energy conversion are shown for ZT = 1 & 2 [116]. The TPV system with spectral control efficiency is calculated for the best possible system achievable today, i.e. the 2D Ta PhC selective emitter and tandem filter on state-of-the-art InGaAs cells, while the TPV system without spectral control uses a blackbody emitter instead without any filter. Ideal single junction TPV limit is calculated assuming ideal cell properties and ideal spectral control as discussed in Section 3.3.6. Shaded regions denote results of experimentally realized systems.

filter. The efficiency could be increased to $\sim 40\%$ absolute (the theoretical 0.62 eV single bandgap TPV and infinite bandgaps TPV thermodynamic limit at emitter temperature of 1320 K and cell temperature of 300 K are 55% and 77% respectively) if TPV cells are to follow a similar research path witnessed by Si PV cells in the past 30 years. In other words, with state-of-the-art TPV cells and the optimized spectrally selective components discussed in this thesis, 45% of the thermodynamic limit can be achieved, while 75% of this limit can be achieved if realistic TPV cell improvements are made. Hence, by noting that current commercial Si PV cells are 85% as efficient as their thermodynamic limit, we conclude that the advancements in spectral control have far outpaced the advancements in TPV cell development. TPV cell development should therefore be given higher priority in order to further advance TPV energy conversion systems. With these highly realizable improvements, TPV energy conversion could quickly displace current energy con-

version systems in the same class of operation (solid-state energy conversion at $1000\,\mathrm{K} \lesssim T \lesssim 1500\,\mathrm{K}$), namely thermoelectrics and thermionics as shown in Fig. 6-1. Moreover, thermoelectrics have reached a point whereby advancing its figure of merit ZT further is extremely challenging [116], while thermionic converters require very high operating temperatures ($T \gtrsim 1750\,\mathrm{K}$) and substantial current densities for efficient operation [121].

In Chapter 4, we have explored the filling of the cavities of standard 2D MPhC slabs with refractory dielectrics, for instance HfO_2 and SiO_2, in order to extend the angular range of high spectral selectivity. We have shown that standard air-filled 2D MPhCs suffer from diffraction losses, and thus begin to lose its spectral selectivity at polar angles greater than 30°. By filling the holes with suitable dielectric materials, the dimensions of the cavities can be designed to be smaller for the same cutoff wavelength, thus increasing the diffraction threshold to larger polar angles. Using this, it is possible to design omnidirectional and polarization insensitive selective emitters that can operate at higher temperatures. However, challenges remain in realizing this experimentally. Given the vast number of applications including TPV energy conversion, infrared spectroscopy, and bolometry, we highly recommend further research towards its experimental realization. In addition, other forms of selective emission/absorption both spatially and spectrally (e.g. highly narrowband emission over both wavelength and angle, broadband emission over narrow angular spread, narrowband omnidirectional emission) can be extremely useful in many applications. Future research directions should focus on realization of these selective emitters/absorbers, upon which would bring significant contribution to the emerging new field of high temperature nanophotonics.

Finally, we have investigated the viability of PhC enhanced Si cell based TPV systems in Chapter 5. The use of conventional Si solar cells in TPV systems is interesting as they are cheap and commercially available in large sizes, and the technology is significantly more mature and closer to theoretical limits compared to low bandgap TPV cells. Using global non-linear optimization tools, we have demonstrated theoretically a maximum radiant heat-to-electricity efficiency of 6.4% and power density of $0.4\,\mathrm{W\,m^{-2}}$ at 1660 K when implementing both the optimized 2D Ta PhC selective emitter, and the needle synthesis refined DBR cold-side selective filter. In addition, we have developed an experimental large area TPV test setup that enables accurate measurement of TPV

conversion efficiency for any emitter-filter-TPV cell combination of interest. Our experimental setup has achieved a maximum electrical output power of 7.6 W and radiant heat-to-electricity efficiency of 1.18% at 1380 K using standard wafer size back-contacted Sunpower Si solar cells. The experimental results agree extremely well with numerical predictions. Nevertheless, the results indicate that TPV systems require superior thermal management, without which substantial penalties in efficiencies will occur. Different system architectures should be explored in the near future to determine the most efficient design. These efforts, in conjunction with the much needed TPV cell research and development as discussed earlier, could potentially pave the way towards widespread adoption of what may be a promising highly efficient, portable, and reliable energy conversion system.

Bibliography

[1] E. Yablonovitch, "Inhibited Spontaneous Emission in Solid-State Physics and Electronics," Phys. Rev. Lett. **58**, 2059–2062 (1987).

[2] S. John, "Strong Localization of Photons in Certain Disordered Dielectric Superlattices," Phys. Rev. Lett. **58**, 2486–2489 (1987).

[3] E. Yablonovitch, "Photonic band-gap structures," J. Opt. Soc. Am. B **10**, 283–295 (1993).

[4] J. D. Joannopoulos, S. G. Johnson, J. N. Winn, and R. D. Meade, *Photonic Crystals: Molding the Flow of Light* (Princeton University Press, 2008).

[5] J. D. Joannopoulos, P. R. Villeneuve, and S. Fan, "Photonic crystals: putting a new twist on light," Nature **386**, 143–149 (1997).

[6] W. Suh, M. F. Yanik, O. Solgaard, and S. Fan, "Displacement-sensitive photonic crystal structures based on guided resonance in photonic crystal slabs," Appl. Phys. Lett. **82**, 1999–2001 (2003).

[7] B. Ellis, M. A. Mayer, G. Shambat, T. Sarmiento, J. Harris, E. E. Haller, and J. Vučković, "Ultralow-threshold electrically pumped quantum-dot photonic-crystal nanocavity laser," Nat. Photonics **5**, 297–300 (2011).

[8] A. A. Erchak, D. J. Ripin, S. Fan, P. Rakich, J. D. Joannopoulos, E. P. Ippen, G. S. Petrich, and L. A. Kolodziejski, "Enhanced coupling to vertical radiation using a two-dimensional photonic crystal in a semiconductor light-emitting diode," Appl. Phys. Lett. **78**, 563–565 (2001).

[9] E. R. Brown and O. B. McMahon, "Large electromagnetic stop bands in metallodielectric photonic crystals," Appl. Phys. Lett. **67**, 2138–2140 (1995).

[10] M. M. Sigalas, C. T. Chan, K. M. Ho, and C. M. Soukoulis, "Metallic photonic band-gap materials," Phys. Rev. B **52**, 11744–11751 (1995).

[11] S. Fan, P. R. Villeneuve, and J. D. Joannopoulos, "Large omnidirectional band gaps in metallodielectric photonic crystals," Phys. Rev. B **54**, 11245–11251 (1996).

[12] J. G. Fleming, S.-Y. Lin, I. El-Kady, R. Biswas, and K. M. Ho, "All-metallic three-dimensional photonic crystals with a large infrared bandgap," Nature **417**, 52–55 (2002).

[13] M. Zenker, A. Heinzel, G. Stollwerck, J. Ferber, and J. Luther, "Efficiency and power density potential of combustion-driven thermophotovoltaic systems using GaSb photovoltaic cells," IEEE Trans. Electron. Dev. **48**, 367–376 (2001).

[14] C. J. Crowley, N. A. Elkouh, S. Murray, and D. L. Chubb, "Thermophotovoltaic converter performance for radioisotope power systems," in Space Technology and Applications International Forum (AIP, 2005), pp. 601–614.

[15] N. P. Harder and P. Wurfel, "Theoretical limits of thermophotovoltaic solar energy conversion," Semicond. Sci. Technol. **18**, S151–S157 (2003).

[16] V. M. Andreev, A. S. Vlasov, V. P. Khvostikov, O. A. Khvostikova, P. Y. Gazaryan, S. V. Sorokina, and N. A. Sadchikov, "Solar thermophotovoltaic converters based on tungsten emitters," J. Sol. Energy Eng. **129**, 298–303 (2007).

[17] E. Rephaeli and S. Fan, "Absorber and emitter for solar thermophotovoltaic systems to achieve efficiency exceeding the Shockley-Queisser limit," Opt. Express **17**, 15145–15159 (2009).

[18] P. Bermel, M. Ghebrebrhan, W. Chan, Y. X. Yeng, M. Araghchini, R. Hamam, C. H. Marton, K. F. Jensen, M. Soljačić, J. D. Joannopoulos, S. G. Johnson, and I. Celanovic, "Design and global optimization of high-efficiency thermophotovoltaic systems," Opt. Express **18**, A314–A334 (2010).

[19] A. Steinfeld, "Solar thermochemical production of hydrogen - a review," Sol. Energy **78**, 603–615 (2005).

[20] N. Moelders, M. U. Pralle, M. P. McNeal, I. Puscasu, L. Last, W. Ho, A. C. Greenwald, J. T. Daly, and E. A. Johnson, "Designing Thermally Uniform MEMs Hot Micro-bolometers," in Mat. Res. Soc. Symp. Proc. (MRS, 2002), vol. 729, pp. U5.2.1–U5.2.7.

[21] A. Tittl, P. Mai, R. Taubert, D. Dregely, N. Liu, and H. Giessen, "Palladium-based plasmonic perfect absorber in the visible wavelength range and its application to hydrogen sensing," Nano Lett. **11**, 4366–4369 (2011).

[22] J.-J. Greffet, R. Carminati, K. Joulain, J.-P. Mulet, S. Mainguy, and Y. Chen, "Coherent emission of light by thermal sources." Nature **416**, 61–64 (2002).

[23] M. U. Pralle, N. Moelders, M. P. McNeal, I. Puscasu, A. C. Greenwald, J. T. Daly, E. A. Johnson, T. George, D. S. Choi, I. El-Kady, and R. Biswas, "Photonic crystal enhanced narrow-band infrared emitters," Appl. Phys. Lett. **81**, 4685–4687 (2002).

[24] I. Celanovic, D. Perreault, and J. Kassakian, "Resonant-cavity enhanced thermal emission," Phys. Rev. B **72**, 075127 (2005).

[25] A. Heinzel, V. Boerner, A. Gombert, B. Bläsi, V. Wittwer, and J. Luther, "Radiation filters and emitters for the NIR based on periodically structured metal surfaces," J. Mod. Opt. **47**, 2399–2419 (2000).

[26] S.-Y. Lin, J. Moreno, and J. G. Fleming, "Three-dimensional photonic-crystal emitter for thermal photovoltaic power generation," Appl. Phys. Lett. **83**, 380–382 (2003).

[27] H. Sai and H. Yugami, "Thermophotovoltaic generation with selective radiators based on tungsten surface gratings," Appl. Phys. Lett. **85**, 3399–3401 (2004).

[28] I. Celanovic, N. Jovanovic, and J. Kassakian, "Two-dimensional tungsten photonic crystals as selective thermal emitters," Appl. Phys. Lett. **92**, 193101 (2008).

[29] T. A. Walsh, J. A. Bur, Y.-S. Kim, T.-M. Lu, and S.-Y. Lin, "High-temperature metal coating for modification of photonic band edge position," J. Opt. Soc. Am. B **26**, 1450–1455 (2009).

[30] C. H. Seager, M. B. Sinclair, and J. G. Fleming, "Accurate measurements of thermal radiation from a tungsten photonic lattice," Appl. Phys. Lett. **86**, 244105 (2005).

[31] Y. X. Yeng, M. Ghebrebrhan, P. Bermel, W. R. Chan, J. Joannopoulos, M. Soljačić, and I. Celanovic, "Enabling high temperature nanophotonics for energy applications," Proc. Natl. Acad. Sci. USA **109**, 2280–2285 (2011).

[32] A. Narayanaswamy and G. Chen, "Thermal emission control with one-dimensional metallodielectric photonic crystals," Phys. Rev. B **70**, 125101 (2004).

[33] C. E. Kennedy, "Review of Mid- to High-Temperature Solar Selective Absorber Materials," Tech. Rep., National Renewable Energy Lab, NREL/TP-520-31267 (2002).

[34] M. Ghebrebrhan, P. Bermel, Y. X. Yeng, J. D. Joannopoulos, M. Soljačić, and I. Celanovic, "Tailoring thermal emission via Q-matching of photonic crystal resonances," Phys. Rev. A **83**, 033810 (2011).

[35] A. Taflove and S. C. Hagness, *Computational Electrodynamics: The Finite-Difference Time-Domain Method* (Artech House, 2000).

[36] A. F. Oskooi, D. Roundy, M. Ibanescu, P. Bermel, J. D. Joannopoulos, and S. G. Johnson, "Meep: A flexible free-software package for electromagnetic simulations by the FDTD method," Comput. Phys. Comm. **181**, 687–702 (2010).

[37] Y. S. Touloukian and D. P. DeWitt, "Thermal Radiative Properties: Metallic Elements and Alloys," in *Thermophysical Properties of Matter Volume 7* (IFI/PLENUM, 1970).

[38] J.-J. Greffet and M. Nieto-Vesperinas, "Field theory for generalized bidirectional reflectivity: derivation of Helmholtz's reciprocity principle and Kirchhoff's law," J. Opt. Soc. Am. A **15**, 2735–2744 (1998).

[39] H. A. Haus, *Waves and Fields in Optoelectronics* (Prentice-Hall, 1984).

[40] O. V. Sulima and A. W. Bett, "Fabrication and simulation of GaSb thermophotovoltaic cells," Sol. Energy Mater. Sol. Cells **66**, 533–540 (2001).

[41] R. R. Siergiej, B. Wernsman, S. A. Derry, R. G. Mahorter, R. J. Wehrer, S. D. Link, M. N. Palmisiano, R. L. Messham, S. Murray, C. S. Murray, F. Newman, J. Hills, and D. Taylor, "20% efficient InGaAs/InPAs TPV cells," in 5th Conference on Thermophotovoltaic Generation of Electricity (AIP, 2003), pp. 414–423.

[42] C. S. Murray, C. J. Crowley, S. Murray, N. A. Elkouh, R. W. Hill, and D. E. Chubb, "Thermophotovoltaic converter design for radioisotope power systems," in 6th Conference on Thermophotovoltaic Generation of Electricity (AIP, 2004), pp. 123–132.

[43] C. A. Wang, H. K. Choi, S. L. Ransom, G. W. Charache, L. R. Danielson, and D. M. Depoy, "High-quantum-efficiency 0.5 eV GaInAsSb/GaSb thermophotovoltaic devices," Appl. Phys. Lett. **75**, 1305–1307 (1999).

[44] M. W. Dashiell, J. F. Beausang, H. Ehsani, G. J. Nichols, D. M. Depoy, L. R. Danielson, P. Talamo, K. D. Rahner, E. J. Brown, S. R. Burger, P. M. Fourspring, W. F. Topper Jr., P. F. Baldasaro, C. A. Wang, R. K. Huang, M. K. Connors, G. W. Turner, Z. A. Shellenbarger, G. Taylor, J. Li, R. Martinelli, D. Donetski, S. Anikeev, G. L. Belenky, and S. Luryi, "Quaternary InGaAsSb thermophotovoltaic diodes," IEEE Trans. Electron. Dev. **53**, 2879–2891 (2006).

[45] D. L. C. Chan, M. Soljačić, and J. D. Joannopoulos, "Thermal emission and design in 2D-periodic metallic photonic crystal slabs," Opt. Express **14**, 8785–8796 (2006).

[46] M. Blanco, J. G. Martin, and D. C. Alarcon-Padilla, "Theoretical efficiencies of angular-selective non-concentrating solar thermal systems," Sol. Energy **76**, 683–691 (2004).

[47] R. Hamam, I. Celanovic, and M. Soljačić, "Angular photonic band gap," Phys. Rev. A **83**, 035806 (2011).

[48] P. Bermel, M. Ghebrebrhan, M. Harradon, Y. X. Yeng, I. Celanovic, J. D. Joannopoulos, and M. Soljačić, "Tailoring photonic metamaterial resonances for thermal radiation," Nanoscale Res. Lett. **6**, 549 (2011).

[49] J. R. Sambles, G. W. Bradbery, and F. Yang, "Optical excitation of surface plasmons: an introduction," Contemp. Phys. **32**, 173–183 (1991).

[50] N. Jovanovic, *Microstructured Tungsten Thermophotovoltaic Selective Emitters* (Ph. D. Thesis, Department of Electrical Engineering and Computer Science, Massachusetts Institute of Technology, 2008).

[51] M. Araghchini, Y. X. Yeng, N. Jovanovic, P. Bermel, L. A. Kolodziejski, M. Soljačić, I. Celanovic, and J. D. Joannopoulos, "Fabrication of two-dimensional tungsten photonic crystals for high-temperature applications," J. Vac. Sci. Technol. B **29**, 061402 (2011).

[52] S. Brown, *Thermal Emission Measurement and Calibration* (S. B. Thesis, Department of Physics, Massachusetts Institute of Technology, 2009).

[53] E. Lindermeir, P. Haschberger, V. Tank, and H. Dietl, "Calibration of a Fourier transform spectrometer using three blackbody sources," Appl. Opt. **31**, 4527–4533 (1992).

[54] R. H. Knibbs, "The measurement of thermal expansion coefficient of tungsten at elevated temperatures," J. Phys. E: Sci. Instrum. **2**, 515–517 (1969).

[55] H. H. Kolm, "Solar-battery Power Source," Tech. Rep., MIT Lincoln Laboratory, Quarterly Progress Report Group 35 (1956).

[56] B. D. Wedlockt, "Thermo-Photo-Voltaic energy conversion," Proc. of IEEE **51**, 694–698 (1963).

[57] T. J. Coutts, "A review of progress in thermophotovoltaic generation of electricity," Renew. Sust. Energ. Rev. **3**, 77–184 (1999).

[58] W. E. Horne, M. D. Morgan, V. S. Sundaram, and T. Butcher, "500 Watt Diesel Fueled TPV Portable Power Supply," AIP Conf. Proc. **653**, 91–100 (2003).

[59] B. Wernsman, R. G. Mahorter, R. R. Siergiej, S. D. Link, R. J. Wehrer, S. J. Belanger, P. M. Fourspring, S. Murray, F. Newman, D. Taylor, and T. Rahmlow, "Advanced thermophotovoltaic devices for space nuclear power systems," in Space Technology and Applications International Forum (AIP, 2005), pp. 1441–1448.

[60] R. W. Kaszeta, Y. X. Yeng, M. Ghebrebrhan, J. D. Joannopoulos, M. Soljačić, and I. Celanovic, "Advanced radiative emitters for radioisotope thermophotovoltaic power systems," in 5th World Conference on Photovoltaic Energy Conversion / 9th Thermophotovoltaic World Conference (2010).

[61] H. Yugami, H. Sai, K. Nakamura, N. Nakagawa, and H. Ohtsubo, "Solar thermophotovoltaic using $Al_2O_3/Er_3Al_5O_{12}$ eutectic composite selective emitter," in 28th IEEE Photovoltaic Specialists Conference (2000), vol. 1, pp. 1214–1217.

[62] A. Lenert, D. M. Bierman, Y. Nam, W. R. Chan, I. Čelanović, M. Soljačić, and E. N. Wang, "A nanophotonic solar thermophotovoltaic device," Nat. Nanotechnol. **9**, 126–130 (2014).

[63] Y. Nam, Y. X. Yeng, A. Lenert, P. Bermel, I. Celanovic, M. Soljačić, and E. N. Wang, "Solar thermophotovoltaic energy conversion systems with two-dimensional tantalum photonic crystal absorbers and emitters," Sol. Energy Mater. Sol. Cells **122**, 287–296 (2014).

[64] R. A. Lowe, D. L. Chubb, S. C. Farmer, and B. S. Good, "Rare-earth garnet selective emitter," Appl. Phys. Lett. **64**, 3551–3553 (1994).

[65] L. Ferguson and F. Dogan, "A highly efficient NiO-Doped MgO matched emitter for thermophotovoltaic energy conversion," Mat. Sci. Eng. B **83**, 35–41 (2001).

[66] B. Bitnar, W. Durisch, J.-C. Mayor, H. Sigg, and H. Tschudi, "Characterisation of rare earth selective emitters for thermophotovoltaic applications," Sol. Energy Mater. Sol. Cells **73**, 221–234 (2002).

[67] D. L. C. Chan, M. Soljačić, and J. D. Joannopoulos, "Thermal emission and design in one-dimensional periodic metallic photonic crystal slabs," Phys. Rev. E **74**, 016609 (2006).

[68] R. Biswas, D. Zhou, I. Puscasu, E. Johnson, A. Taylor, and W. Zhao, "Sharp thermal emission and absorption from conformally coated metallic photonic crystal with triangular lattice," Appl. Phys. Lett. **93**, 063307 (2008).

[69] D. L. C. Chan, M. Soljačić, and J. D. Joannopoulos, "Direct calculation of thermal emission for three-dimensionally periodic photonic crystal slabs," Phys. Rev. E **74**, 036615 (2006).

[70] T. D. Rahmlow, J. E. Lazo-wasem, E. J. Gratrix, P. M. Fourspring, and D. M. Depoy, "New performance levels for TPV front surface filters," in 6th Conference on Thermophotovoltaic Generation of Electricity (2004), pp. 180–188.

[71] R. T. Kristensen, J. F. Beausang, and D. M. Depoy, "Frequency selective surfaces as near-infrared electromagnetic filters for thermophotovoltaic spectral control," J. Appl. Phys. **95**, 4845–4851 (2004).

[72] F. O'Sullivan, I. Celanovic, N. Jovanovic, J. Kassakian, S. Akiyama, and K. Wada, "Optical characteristics of one-dimensional Si/SiO_2 photonic crystals for thermophotovoltaic applications," J. Appl. Phys. **97**, 033529 (2005).

[73] T. D. Rahmlow, D. M. Depoy, P. M. Fourspring, H. Ehsani, J. E. Lazo-Wasem, and E. J. Gratrix, "Development of front surface, spectral control filters with greater temperature stability for thermophotovoltaic energy conversion," in 7th Conference on Thermophotovoltaic Generation of Electricity (AIP, 2007), vol. 890, pp. 59–67.

[74] G. W. Charache, D. M. DePoy, P. F. Baldasaro, and B. C. Campbell, "Thermophotovoltaic devices utilizing a back surface reflector for spectral control," AIP Conf. Proc. **358**, 339–350 (1996).

[75] R. K. Huang, C. A. Wang, M. K. Connors, G. W. Turner, and M. W. Dashiell, "Hybrid back surface reflector GaInAsSb thermophotovoltaic devices," AIP Conf. Proc. **738**, 329–336 (2004).

[76] L. B. Karlina, M. M. Kulagina, N. K. Timoshina, A. S. Vlasov, and V. M. Andreev, "$In_{0.53}Ga_{0.47}As/InP$ conventional and inverted thermophotovoltaic cells with back surface reflector," AIP Conf. Proc. **890**, 182–189 (2007).

[77] P. F. Baldasaro, J. E. Raynolds, G. W. Charache, D. M. Depoy, C. T. Ballinger, T. Donovan, and J. M. Borrego, "Thermodynamic analysis of thermophotovoltaic efficiency and power density tradeoffs," J. Appl. Phys. **89**, 3319–3327 (2001).

[78] T. A. Walsh and S.-Y. Lin, "Power density and efficiency of thermophotovoltaic energy conversion using a photonic-crystal emitter and a 2-D metal-grid filter," IEEE Trans. Electron. Dev. **55**, 1101–1108 (2008).

[79] V. Rinnerbauer, S. Ndao, Y. X. Yeng, J. J. Senkevich, K. F. Jensen, J. D. Joannopoulos, M. Soljačić, I. Celanovic, and R. D. Geil, "Large-area fabrication of high aspect ratio tantalum photonic crystals for high-temperature selective emitters," J. Vac. Sci. Technol. B **31**, 011802 (2013).

[80] V. Rinnerbauer, Y. X. Yeng, W. R. Chan, J. J. Senkevich, J. D. Joannopoulos, M. Soljačić, and I. Celanovic, "High-temperature stability and selective thermal emission of polycrystalline tantalum photonic crystals," Opt. Express **21**, 11482–11491 (2013).

[81] B. Wernsman, R. R. Siergiej, S. D. Link, R. G. Mahorter, M. N. Palmisiano, R. J. Wehrer, R. W. Schultz, G. P. Schmuck, R. L. Messham, S. Murray, C. S. Murray, F. Newman, D. Taylor, D. M. Depoy, and T. Rahmlow, "Greater than 20% radiant heat conversion efficiency of a thermophotovoltaic radiator/module system using reflective spectral control," IEEE Trans. Electron. Dev. **51**, 512–515 (2004).

[82] W. Chan, R. Huang, C. A. Wang, J. Kassakian, J. D. Joannopoulos, and I. Celanovic, "Modeling low-bandgap thermophotovoltaic diodes for high-efficiency portable power generators," Sol. Energy Mater. Sol. Cells **94**, 509–514 (2010).

[83] Y. X. Yeng, W. R. Chan, V. Rinnerbauer, J. D. Joannopoulos, M. Soljačić, and I. Celanovic, "Performance analysis of experimentally viable photonic crystal enhanced thermophotovoltaic systems," Opt. Express **21**, A1035–A1051 (2013).

[84] E. R. G. Eckert and E. M. Sparrow, "Radiative heat exchange between surfaces with specular reflection," Int. J. Heat Mass Transfer **3**, 42–54 (1961).

[85] J. Nelson, *The Physics of Solar Cells* (Imperial College Press, 2003).

[86] S. Kucherenko and Y. Sytsko, "Application of deterministic low-discrepancy sequences in global optimization," Comput. Optim. Appl. **30**, 297–318 (2005).

[87] M. J. D. Powell, *Advances in Optimization and Numerical Analysis* (Kluwer Academic, 1994).

[88] W. L. Price, "Global optimization by controlled random search," J. Optim. Theory Appl. **40**, 333–348 (1983).

[89] S. G. Johnson, "The NLopt nonlinear-optimization package," http://ab-initio.mit.edu/nlopt.

[90] J. Bravo-Abad, F. J. García-Vidal, and L. Martín-Moreno, "Resonant transmission of light through finite chains of subwavelength holes in a metallic film," Phys. Rev. Lett. **93**, 227401 (2004).

[91] NREL, "Best research-cell efficiencies chart," http://www.nrel.gov/ncpv/images/efficiency_chart.jpg.

[92] C. H. Henry, "Limiting efficiencies of ideal single and multiple energy gap terrestrial solar cells," J. Appl. Phys. **51**, 4494–4500 (1980).

[93] W. Shockley and H. J. Queisser, "Detailed balance limit of efficiency of p-n junction solar cells," J. Appl. Phys. **32**, 510–519 (1961).

[94] L. M. Fraas and L. Minkin, "TPV history from 1990 to present & future trends," AIP Conf. Proc. **890**, 17–23 (2007).

[95] R. M. Swanson, "Silicon photovoltaic cells in thermophotovoltaic energy conversion," in International Electron Devices Meeting (1978), pp. 70–73.

[96] P. L. Adair, Z. Chen, and M. F. Rose, "TPV Power generation prototype using composite selective emitters," in 3rd NREL Conference on Thermophotovoltaic Generation of Electricity (ASCE, 1997), vol. 277, pp. 277–290.

[97] W. Yang, S. Chou, C. Shu, H. Xue, and Z. Li, "Design, Fabrication, and Testing of a Prototype Microthermophotovoltaic System," J. Microelectromech. Syst. **13**, 851–856 (2004).

[98] D. Kirikae, Y. Suzuki, and N. Kasagi, "A silicon microcavity selective emitter with smooth surfaces for thermophotovoltaic power generation," J. Micromech. Microeng. **20**, 104006 (2010).

[99] B. Bitnar, W. Durisch, and R. Holzner, "Thermophotovoltaics on the move to applications," Appl. Energy **105**, 430–438 (2013).

[100] W. R. Chan, P. Bermel, R. C. N. Pilawa-Podgurski, C. H. Marton, K. F. Jensen, J. J. Senkevich, J. D. Joannopoulos, M. Soljačić, and I. Celanovic, "Toward high-energy-density, high-efficiency, and moderate-temperature chip-scale thermophotovoltaics." Proc. Natl. Acad. Sci. USA **110**, 5309–5314 (2013).

[101] J. Zhao, A. Wang, P. P. Altermatt, S. R. Wenham, and M. A. Green, "24% Efficient perl silicon solar cell: Recent improvements in high efficiency silicon cell research," Sol. Energy Mater. Sol. Cells **42**, 87–99 (1996).

[102] N. Liu, M. Mesch, T. Weiss, M. Hentschel, and H. Giessen, "Infrared perfect absorber and its application as plasmonic sensor," Nano Lett. **10**, 2342–2348 (2010).

[103] S. E. Han and D. J. Norris, "Beaming thermal emission from hot metallic bull's eyes," Opt. Express **18**, 4829–4837 (2010).

[104] T. V. Teperik, F. J. García de Abajo, A. G. Borisov, M. Abdelsalam, P. N. Bartlett, Y. Sugawara, and J. J. Baumberg, "Omnidirectional absorption in nanostructured metal surfaces," Nat. Photonics **2**, 299–301 (2008).

[105] B. Zhao and Z. M. Zhang, "Study of magnetic polaritons in deep gratings for thermal emission control," J. Quant. Spectrosc. Radiat. Transfer **135**, 81–89 (2014).

[106] N. P. Sergeant, O. Pincon, M. Agrawal, and P. Peumans, "Design of wide-angle solar-selective absorbers using aperiodic metal-dielectric stacks." Opt. Express **17**, 22800–22812 (2009).

[107] J. B. Chou, Y. X. Yeng, A. Lenert, V. Rinnerbauer, I. Celanovic, M. Soljačić, E. N. Wang, and S.-G. Kim, "Design of wide-angle selective absorbers/emitters with dielectric filled metallic photonic crystals for energy applications," Opt. Express **22**, A144–A154 (2013).

[108] V. Liu and S. Fan, "A free electromagnetic solver for layered periodic structures," Comput. Phys. Comm. **183**, 2233–2244 (2012).

[109] H.-J. Lee, K. Smyth, S. Bathurst, J. Chou, M. Ghebrebrhan, J. Joannopoulos, N. Saka, and S.-G. Kim, "Hafnia-plugged microcavities for thermal stability of selective emitters," Appl. Phys. Lett. **102**, 241904 (2013).

[110] F. L. Martínez, M. Toledano-Luque, J. J. Gandía, J. Cárabe, W. Bohne, J. Röhrich, E. Strub, and I. Mártil, "Optical properties and structure of HfO_2 thin films grown by high pressure reactive sputtering," J. Phys. D: Appl. Phys. **40**, 5256–5265 (2007).

[111] H. R. Philipp, "The infrared optical properties of SiO_2 and SiO_2 layers on silicon," J. Appl. Phys. **50**, 1053–1057 (1979).

[112] S. Kalogirou, "Solar thermal collectors and applications," Prog. Ener. Comb. Sci. **30**, 231–295 (2004).

[113] J. Wang, Z. Chen, and D. Li, "Simulation of two-dimensional Mo photonic crystal surface for high-temperature solar-selective absorber," Phys. Status Solidi A **207**, 1988–1992 (2010).

[114] C. Wu, B. Neuner III, J. John, A. Milder, B. Zollars, S. Savoy, and G. Shvets, "Metamaterial-based integrated plasmonic absorber/emitter for solar thermo-photovoltaic systems," J. Opt. **14**, 024005 (2012).

[115] J. W. Schwede, I. Bargatin, D. C. Riley, B. E. Hardin, S. J. Rosenthal, Y. Sun, F. Schmitt, P. Pianetta, R. T. Howe, Z.-X. Shen, and N. A. Melosh, "Photon-enhanced thermionic emission for solar concentrator systems," Nat. Mater. **9**, 762–767 (2010).

[116] M. Zebarjadi, K. Esfarjani, M. S. Dresselhaus, Z. F. Ren, and G. Chen, "Perspectives on thermoelectrics: from fundamentals to device applications," Energy Environ. Sci. **5**, 5147–5162 (2012).

[117] J. Zhao, A. Wang, and M. A. Green, "24.5% Efficiency silicon PERT cells on MCZ substrates and 24.7% efficiency PERL cells on FZ substrates," Prog. Photovoltaics Res. Appl. **7**, 471–474 (1999).

[118] P. Wilkinson, "Photonic Bloch oscillations and Wannier-Stark ladders in exponentially chirped Bragg gratings," Phys. Rev. E **65**, 056616 (2002).

[119] G. A. Al-Jumaily and S. M. Edlou, "Optical properties of tantalum pentoxide coatings deposited using ion beam processes," Thin Solid Films **209**, 223–229 (1992).

[120] A. V. Tikhonravov, M. K. Trubetskov, and G. W. Debell, "Application of the needle optimization technique to the design of optical coatings." Appl. Opt. **35**, 5493–508 (1996).

[121] S. F. Adams, "Solar Thermionic Space Power Technology Testing: A Historical Perspective," AIP Conf. Proc. **813**, 590–597 (2006).